

Deformation Processes Adjacent to Active Faults – Examples
from Eastern California

Eitan Shelef

A thesis submitted to the faculty of the University of North Carolina at Chapel Hill in partial fulfillment of the requirements for the degree Master of Science in the Department of Geological Sciences.

Chapel Hill
2007

Approved by:

Dr. Michael Oskin

Dr. Allen Glazner

Dr. Jonathan Lees

Abstract

EITAN SHELEF: Deformation Processes Adjacent to Active Faults – Examples from Eastern California
(Under the direction of Dr. Michael Oskin)

Major seismogenic faults occur within bands of inelastic off-fault deformation (OFD), where both distributed displacement and modification of rock properties occur. Active distributed displacement may affect slip-rate estimates, understanding of seismic energy radiation and geodynamic models. This study addresses the role of OFD in the displacement history and mechanical behavior of major seismogenic faults. Here I present a multi-site study of planar and linear geologic features next to active strike-slip faults in the central Mojave Desert. Conservative estimates suggest that distributed displacement accommodates 19 ± 3 % of the total displacement over zones of 1 to 4 km width. Most of this displacement occurs within 100-200 m of faults and decreases exponentially with distance from the main fault. Distributed displacement is accommodated by a combination of block rotation and simple shear across secondary faults. Analysis of block dimensions show that blocks tend to decrease in size toward faults. Conservative estimates indicate that the cumulative length of secondary faults is at least a factor of ten greater than the length of the main fault. Finally, I argue that distributed displacement is an active feature and suggests that zones of diminished rigidity near faults may be at least in part driven by formation and lengthening of secondary faults and their associated OFD zones.

To Yosef

Acknowledgments

To the casual observer, a thesis dissertation may appear to be solitary work. However, to complete a project of this magnitude requires a network of support, and I am indebted to many people. First, I would like to thank Dr. Mike Oskin, for his endless patient and continuous support, as well as for his enlightening ideas, valuable advices, and tremendous contribution to this work. I would also like to thank Dr. Oskin for many enjoyable scientific discussions and for giving me the freedom that made this project the great experience it was for me. I would like to thank Dr. Jonathan Lees for valuable advices regarding data analysis and computer programming, and for being always available and willing to help. To Dr. Allen Glazner, for constructive reviews of this thesis and the preceding research proposal, as well as for helpful advice regarding the geology of the Mojave desert.

I would also like to thank Dr. Elizabeth Cochran, for providing the seismic refraction equipment, and for aiding with its deployment and with the analysis of the refraction data. To Dr. Yuri Fialko, for providing me with InSAR-based displacement data, and advise regarding its analysis. To Dr. Joe Kirschvink for letting me use the paleomagnetism lab at Caltech, for his advice regarding the analysis of the paleomagnetic data, and for his generous hospitality. To Dr. Jim Cassidy, for leading us in the perilous terrain of the 29 Palms marine base, and for his generous hospitality. To James Barry, for guiding us in the Hector mine. To Dr. Missey Eppes and Dr. Andy Bobyarchick for their help with providing and utilizing the

ground penetrating radar. To Robert and Marilyn Oskin, for their generous hospitality, great company, and generous portions of excellent food. To Richard Lease for his help with the processing of paleomagnetic samples and for his company in the field. To my field assistants: Mike Strane, Mariana Vale, Neta Bar, Dolev Shelef, and Tomer Ben-David, for their help and enjoyable company during long field periods. It is a pleasure for me to thank Oskin's research group: Kim Le, Scott Bennett, Jacob Selander, Mike Strane, Sabrina Belknap and Emily Gurney, for their supportive, helpful, and friendly company during the last two years. I am most especially grateful to the Martin Fund, SCEC and NSF, for supporting this project and making it possible.

Finally, I would like to thank my Parents, Yosef and Nurit Shelef, for installing their fascination with nature in me, for teaching me how to ask questions, and for much more than can be written here. I would like to thank my wife, friend, and companion - Neta Bar, for the big adventure she led me to, and for being the way she is through it. Last, I want to thank the Mojave Desert, for the wide horizons, the starry nights, the firewood, and for the great questions and answers hidden in its rocks.

Table of contents

Abstract.....	ii
Acknowledgments.....	IV
Table of contents.....	VI
List of figures.....	IX
List of abbreviations	XI
1. Introduction.....	1
2. Methods.....	18
2.1. Mapping.....	18
2.2. Measurements of mylonitic lineation.....	19
2.3. Paleomagnetism.....	19
2.4. Seismic refraction survey.....	20
2.5. InSAR	22
3. Observations	23
3.1. Deflection of continuous planar markers within OFD zones.....	23
3.2. Rotation of local linear markers within OFD zones	26
3.2.1 Mylonitic lineation.....	26
3.2.2 Paleomagnetic data	30

3.3. Distribution of and offsets along secondary faults within OFD zones	36
3.4. Seismic refraction survey.....	36
4. Data analysis.....	43
4.1. Analysis of mylonitic lineation directions adjacent to the Harper Lake fault	43
4.1.1. Variability of mylonitic lineation directions as function of distance from the fault	43
4.1.2. Calculation of maximum block dimensions within the OFD zone.....	45
4.1.3. Secondary fault density within the OFD zone	54
4.1.4. Rotational shear displacement accommodated within the OFD zone	61
4.2. Analysis of seismic refraction data to trace changing rock properties within OFD zones	65
4.3. InSAR data analysis to trace the effect of lithology on rigidity.	76
5. Discussion.....	79
5.1. Assumptions.....	79
5.2. Magnitude of Distributed Displacement.....	80
5.3. OFD zone width.....	82
5.4. Distribution of shear displacement within the OFD zone.....	82
5.5. Activity of OFD.....	83
5.6. Structural mechanism of strain accommodation within OFD zones	84
5.7. Damage and displacement interactions within OFD zones	87
6. Conclusions.....	90
Appendix 1: Table of mylonite lineation direction.....	92

Appendix 2: Calculation of parameters for seismic refraction model.	107
Appendix 3: $^{40}\text{Ar}/^{39}\text{Ar}$ dating of the Sunshine and Lavic basalts	112
Appendix 4: Cenozoic evolution of the Ludlow fault, Cady Mountains and Blacktop Hills, California.....	117
References.....	131

List of figures

Figure 1. Mechanisms of off-fault displacement	2
Figure 2. Location map	5
Figure 3. Illustration of a refraction line	21
Figure 4. Deflected geologic features next to the Calico fault	24
Figure 5. Lengths of dike segments vs. distance from the Calico fault	25
Figure 6. Map of mylonitic lineation measurements along the Harper Lake fault	27
Figure 7. Mylonite rotation vs. distance from the Harper Lake fault	28
Figure 8. Trend vs. plunge of mylonitic lineation measurements	29
Figure 9. Mylonite rotation vs. distance from secondary fault A	31
Figure 10. Mylonite rotation vs. distance from secondary fault B	32
Figure 11. Rotation values for paleomagnetic sites	34
Figure 12. Example plots of paleomagnetic analysis	35
Figure 13. Map of the Pisgah fault in the Sunshine Peak basalt field	37
Figure 14. $^{40}\text{Ar}/^{39}\text{Ar}$ dating of the Sunshine and Lavic basalts	38
Figure 15. Map of offset contacts next to secondary fault B	39
Figure 16. Index map of seismic refraction lines	40
Figure 17. First arrival time vs. distance for seismic refraction lines	41
Figure 18. Mylonitic lineation variance vs. distance from the Harper Lake fault	44
Figure 19. Patterns of mylonite rotation along segments of the Harper Lake fault	46
Figure 20. Analysis of block radii	48
Figure 21. Analysis of block radii - sorted	49
Figure 22. Block radii vs. distance from the Harper Lake fault	50

Figure 23. Comparison of real data vs. randomly generated data	52
Figure 24. Block radii vs. distance from the fault, excluding secondary fault	53
Figure 25. Block radii vs. distance from the southern section of the fault	55
Figure 26. Geometric illustration of blocks number calculation	57
Figure 27. Geometric illustration of secondary-faults density calculation	60
Figure 28. Mylonite rotation vs. distance from the northern section of the fault	62
Figure 29. conceptual models for cumulative shear displacement	64
Figure 30. Illustration of tilted velocity structure	68
Figure 31. Illustration of circular ray-path.....	70
Figure 32. Geometric illustration for seismic refraction model.....	71
Figure 33. Model fits for all refraction lines.....	73
Figure 34. Best fit parameter results for all refraction lines	74
Figure 35. Modeled velocity structure	75
Figure 36. Illustration of InSAR data analysis.....	77
Figure 37. Conceptual model for the mechanisms of distributed displacement	85

List of abbreviations

OFD	Off fault deformation
ECSZ	Eastern California shear zone
InSAR	Interferometric synthetic aperture rada

1. Introduction

Major seismogenic faults are embedded within narrow zones of inelastic off-fault deformation (OFD), where both distributed displacement and modification of rock properties occur (Fialko et al., 2002; Katz et al., 2003; Li et al., 1998; Faulkner et al., 2006). In the brittle crust, OFD includes faulting, rigid body rotation and fracturing (Katz et al., 2003; Nelson and Jones, 1987; Sonder et al., 1994; Fig.1). Distributed shear displacement within OFD-zones along strike-slip faults can account for up to 60% of the total shear displacement (Kimorah et al., 2004; Nelson and Jones, 1987; Miller and Yount, 2002). This distributed displacement is difficult to observe and quantify and thus is often ignored in tectonic reconstructions. If OFD is active, it will change slip-rate estimates and thus could affect comparisons with geodetic loading rates, seismic hazard analysis, and geodynamic models (Salyards et al., 1992; Thatcher and Lisowski, 1987; Hilley et al., 2005). Fracturing also represents a potentially significant sink of seismic energy (Shipton et al., 2006; Wilson et al., 2005; Chester et al., 2005).

By modifying bulk rock properties, OFD could also play an important role in the mechanics of faulting. OFD, including rock pulverization, leads to a reduction of shear rigidity within the fault zone that affects stress orientation and elastic strain distribution next to faults (Faulkner et al., 2006). In detail, this process involves the accrual of damage through creation and growth of cracks in a rock mass (Lemaitre and Desmorat, 2005). This damage

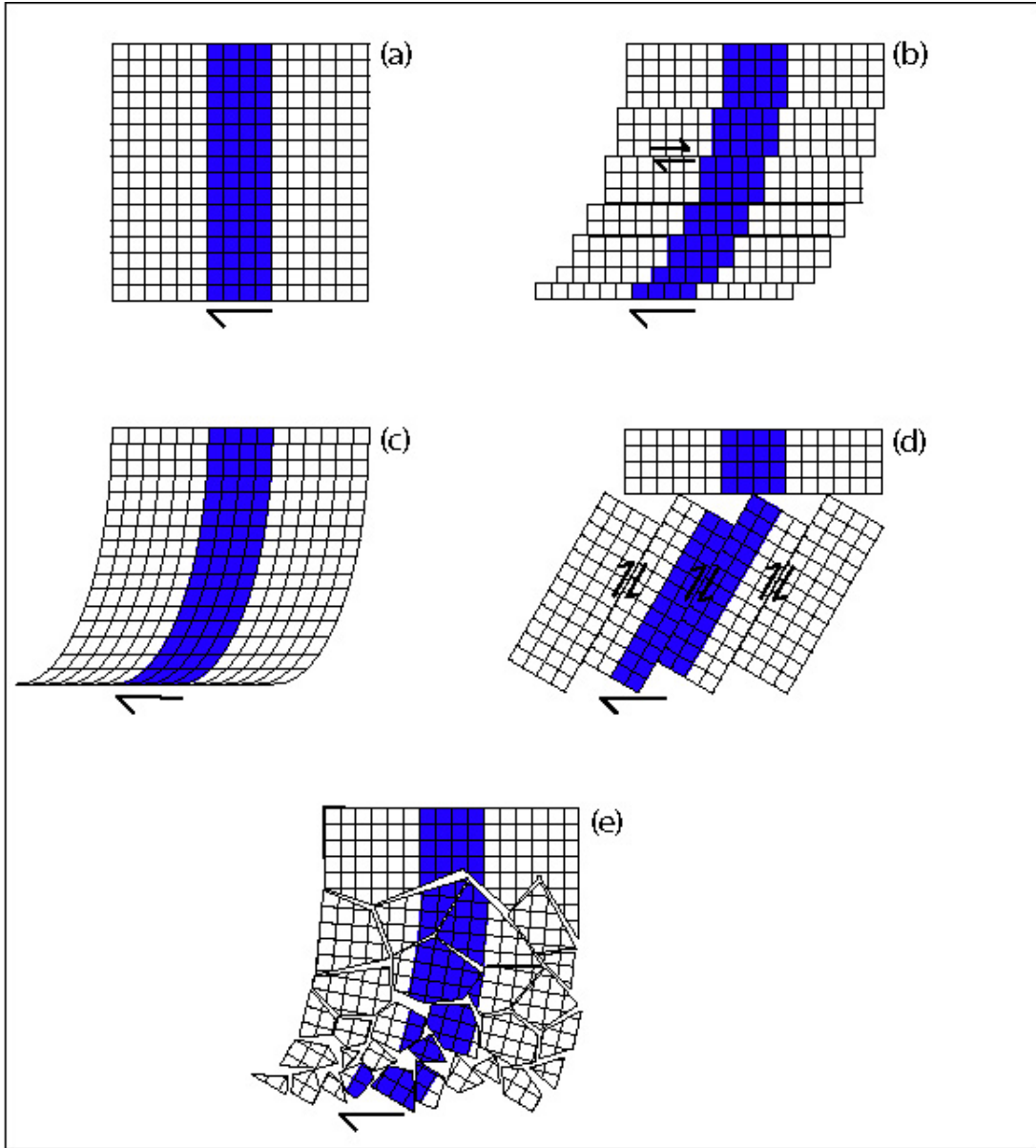


Figure 1. Mechanisms of off-fault displacement

After Nelson and Jones (1987): (a) undeformed domain, (b) shear on faults sub parallel to the main fault, (c) pervasive continuous shear, (d) block rotation accompanied by internal antithetic shear, (e) small block rotation.

reduces the effective area that supports stress load (Rabotnov, 1988, as cited by Lyachovsky et al, 2005), and thus leads to formation of a compliant zone of reduced rigidity. Compliant fault zones have been observed seismically and geodetically (Fialko et al., 2002, 2004; Li et al., 1998; Li and Vidale, 2001) and are attributed to damage acquired during coseismic dynamic rupture propagation (Li et al., 1998, 2002, 2003; Yamashita, 2000). Though this damage is permanent deformation, shear rigidity can recover from damage through a process known as healing whereby cracks within a rock mass gradually relax and close. Healing has also been observed on active faults within a span of several years following an earthquake rupture (Li et al., 1998, 2002, 2003; Li and Vidale, 2001). Because of healing effects, OFD is not a direct proxy for the reduction of shear rigidity in fault zones. However, to the extent that damage is proportional to distributed shear displacement, such displacement provides useful insight into the time-integrated pattern of fracture production and the expected distribution of rigidity surrounding active faults.

This study addresses the role of OFD in the displacement history and mechanical behavior of major seismogenic faults. Because it is easiest to quantify, this study focuses on the component of OFD expressed as distributed shear displacement. To accomplish this I seek to characterize several basic attributes of distributed displacement from geologic observations. These include quantifying: (1) What fraction of the total shear displacement occurs as distributed displacement? (2) How wide is the zone of distributed displacement? (3) What is the distribution of displacement within this zone? (4) Is distributed displacement active? (5) What structural mechanisms accommodate displacement? I also seek to understand how zones of OFD are related to compliant zones surrounding active faults. This study addresses these questions through study of active strike-slip faults traversing the

Mojave Desert of southern California. The Mojave section of the eastern California shear zone (ECSZ, Fig. 2), has been an area of active strike-slip faulting since the early Miocene (Glazner et al., 2002). The potential discrepancy between fast geodetic rates (Dixon et al., 1995; Gan et al., 2000) to slow fault slip-rates across the ECSZ (Rockwell et al., 2000; Oskin et al., in review) may be at least in part due to unaccounted distributed displacement.

Abundant exposure of planar and linear features next to active faults in the Mojave Desert provides ample opportunity to study the magnitude, mechanism and activity of distributed shear. Well-documented $M_w > 7$ earthquakes that occurred in the Mojave Desert during the 1990's allow observation of coseismic patterns of OFD. These patterns can be compared to distributed displacement integrated over multiple seismic cycles.

Distributed shear displacement is usually quantified from deflected planar and linear features next to faults (Albers et al., 1967; Richard et al., 1991; Katz et al., 2003; Sonder et al., 1994; Thatcher and Lisowski, 1987). The resolution of these processes depends on scale of observation and may appear continuous. The convex shape of continuously deflected geologic features next to faults is often called “fault drag” (Dennis, 1972, Reches and Eidelman, 1995), “drag folds” (Davis, 1984), or “flanking features” (Passchier, 2001). Reches and Eidelman (1995) describe “normal drag,” where the convexity is similar to the sense of shear on the fault, and “reverse drag,” where the sense of shear from deflected features is opposite that of the fault. “Reverse drag” occurs where folding compensates for fault-slip gradients. In narrow OFD zones reverse drag may occur where a steep, local, slip gradient exists. However, reverse drag is in general not relevant at the scale of the narrow OFD zones studied here.

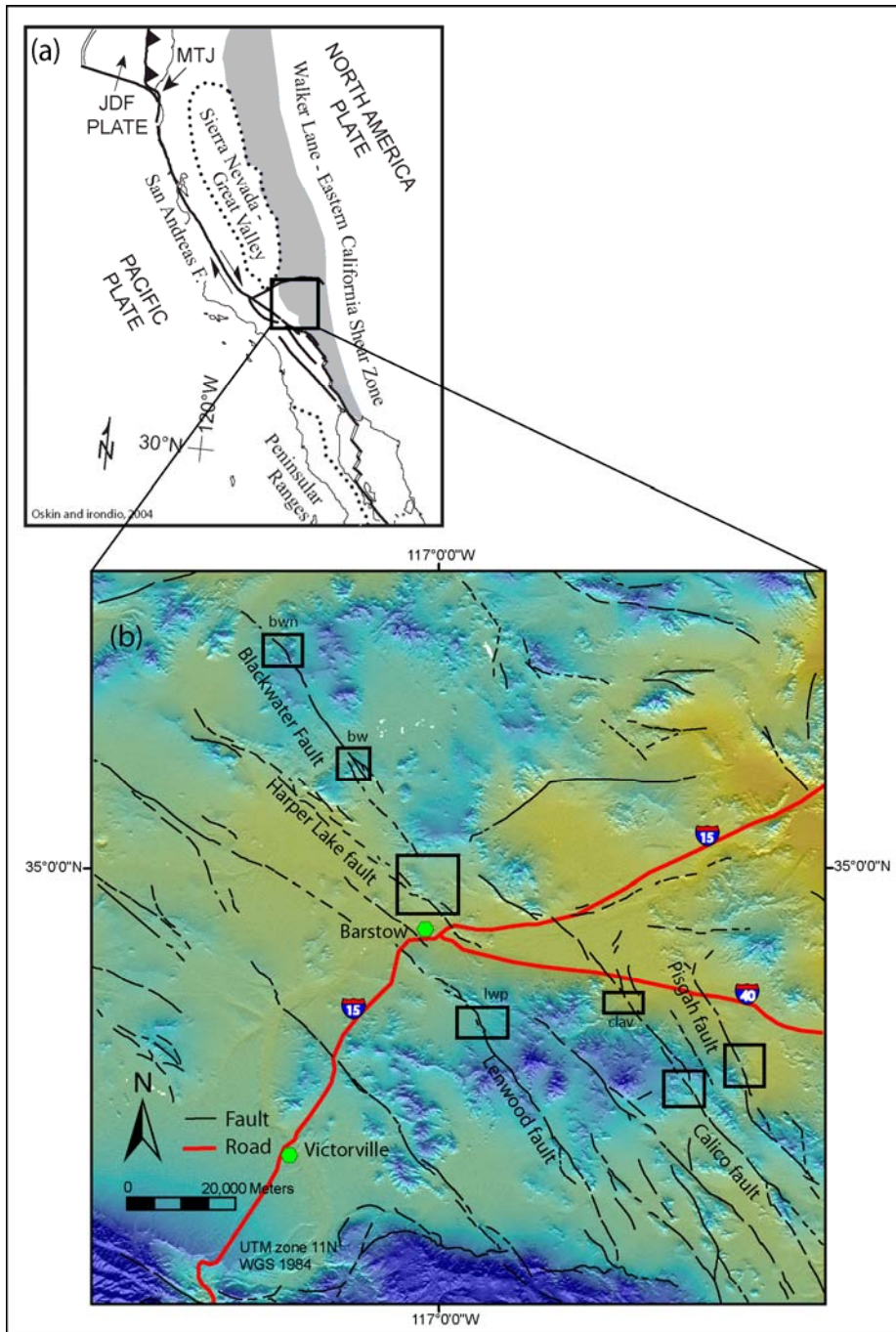


Figure 2. Location map

(a) Index map of the Eastern California Shear Zone (ECSZ). The ECSZ is a zone of distributed dextral faulting along the Pacific North America plate boundary (Dokka and Travis, 1990). (b) The Mojave Desert section of the ECSZ, black frames show study areas. lwp, bw, bwn, and clay, are names of paleomagnetic study sites.

One of the challenges in understanding the role of OFD in active faulting is that the distribution and amount of OFD are likely to evolve over the various stages of fault nucleation and growth. Pre-faulting deformation is assumed to be quasi-uniformly distributed and to reflect preexisting stress and strain fields (Katz et al., 2003; Lyachovsky et al., 1997). Fault-growth related OFD probably occurs next to a propagating fault tip due to elevated stress load (Vermilye and Scholz, 1998). Slip-related OFD takes place next to mature, active master faults and is attributed to wear due to fault roughness (Scholz, 1990) and to inelastic deformation during coseismic dynamic rupture (Li et al., 1998, 2002; Yamashita, 2000).

2. Methods

I focus my observations on macroscopic planar and linear features next to faults that record net shear displacement by faulting and rotation. To quantify distributed displacement I measured and mapped continuous unique planar markers such as faults and dikes, as well as non-unique linear markers such as mylonitic lineation and paleomagnetic vectors. I isolate the dependency of distributed displacement on lithology, fault displacement, and timing of marker emplacement by pairing study sites that differ by only one of these variables. Comparison between distributed displacement and fault compliant zones is determined from seismic velocity measurements and InSAR (Fialko et al., 2002).

2.1. Mapping

To gain an overview of the distribution and mechanism of OFD I mapped secondary faults, dikes, and contacts next to the Harper Lake, Calico, and Pisgah faults. Preliminary mapping was done using high-resolution aerial photos. Complementary detailed field mapping in a scale of 1:5000 was acquired next to the Calico and Harper Lake faults. Field mapping next to the Pisgah fault was limited in time and extent due to live ammunition military training on the Twenty-nine Palms marine base. Thus, mapping of the Pisgah fault next to the Sunshine Peak lava field is partly based on preexisting mapping by Wilbur (1980) and on a report by Hart (1988). Along the Calico and Harper Lake faults, I used differential GPS to survey dikes and faults in places where location precision was essential.

2.2. Measurements of mylonitic lineation

In order to get a detailed spatial view of rigid block rotation next to a fault I measured mylonitic lineation directions (n=648) in the early Miocene central Mojave metamorphic core complex (Fletcher et al., 1995) where it has been cut by the active dextral Harper Lake fault. Measurement sites are located within a 6.5 km by 1.5 km region of the Mitchel Range, bounded on the southwest by the Harper Lake fault. Sites were selected with good in-situ exposure indicated by outcrop field appearance and by homogenous lineation over an area of ~10-40 m². Brunton compass was used to measure lineation trend and plunge and a handheld GPS to measure site locations. Location errors are less than 15m. Differential GPS with an error of ~1m was used where changes in mylonitic lineation were measured over short distances. Because I did not measure S-C fabrics or other shear sense indicators it is not possible to deduce mylonite rotation >90° from the data set. To resolve this problem I use the farthest measurement point as a reference point and present the measurements as mylonite rotation relative to this point. Conservative mylonite rotation values are presented by limiting the azimuthal component of rotation to <90°.

2.3. Paleomagnetism

Paleomagnetic measurements of markers with uniform pre-faulting remanence direction were used to attempt to quantify differential vertical-axis rotation next to active faults. I sampled previously dated volcanic units in five areas to relate the timing of rotation and faulting. Each area is composed of 3 to 10 sampling sites located at increasing distances from a fault. Most sites consist of 6-10 individual samples collected over an area of 10 to 50 m². All core samples were oriented in situ using solar compass. Demagnetization measurements

were carried with a superconducting cryogenic magnetometer sensitive to 2×10^{-9} emu. Most samples underwent alternating field demagnetization up to 70 mT, with 5 mT steps up to 10 mT, and 10 mT steps between 10 to 70 mT. Specimens from cores of samples that did not yield stable primary magnetization went through demagnetization path composed of alternating field demagnetization of 2.5 mT steps between 2.5 mT to 10 mT, followed by thermal steps of 50° C from 150° to 650° C. Line and plane fits were calculated following Kirschvink (1980), site mean directions were calculated (Fisher, 1953), and tilt correction was applied using Paleomag software 3.1 (Jones, 2002). Rotation and flattening were determined following the methods of Beck (1980) and Demarest (1983) by using the furthest site from the fault as a reference site.

2.4. Seismic refraction survey

In order to compare the distribution of displacement within the OFD zone to the spatial change of rock properties next to faults, a 1030 m-long refraction survey was conducted across the Calico fault in the same region where I had mapped deflected markers. With the aid of Elizabeth Cochran (U.C. Riverside), I deployed five sequential refraction lines approximately perpendicular to the fault. Each line, 110 to 230 m long with 10 m geophone spacing, was triggered using a hammer and plate source from four different shot points. Two shot points were located at each line end-point termed close shot points, and two shot points located 50 m away from each end-point termed far shot points. For each line, the two western shot points are termed forward shot points while the two eastern shot points are termed reverse shot points (Fig. 3). 10 hits at each shot point were stacked to reduce errors in the seismic signal. Seismic signals were filtered using a notch filter at 60 Hz to screen noise

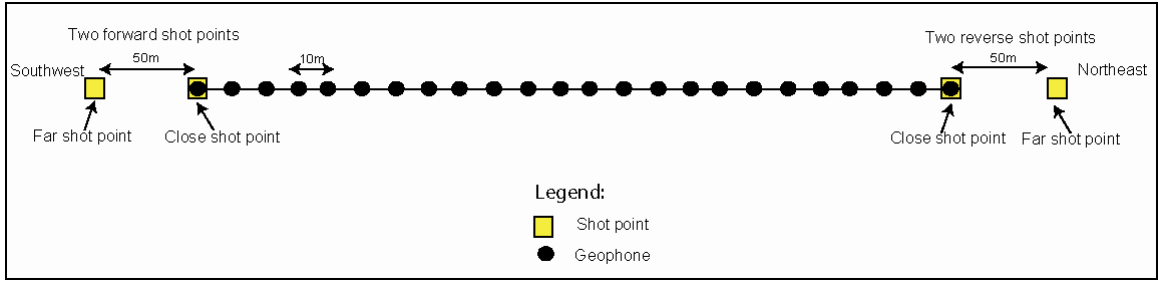


Figure 3. Illustration of a refraction line

Illustration of a single refraction line. Black dots are geophones, yellow squares are shot point locations. Note the forward-reverse, close-far terminology for the shot points.

induced by an adjacent power line. Most of the first arrivals were chosen manually from the data set.

2.5. InSAR

In order to test for the effect of lithology on rigidity reduction near faults of the central Mojave Desert I examine the lithology of compliant zones that were imaged with InSAR by Fialko et al., (2002). Through collaboration with Dr. Fialko of UCSD, I acquired the high-pass filtered interferogram that Fialko et al., (2002) derived from data acquired within few months before and after the 1999 M_w 7.1 Hector Mine earthquake. Fialko et al., (2002) showed that compliant zones of reduced rigidity are revealed in this data by elastic deformation resulting from static stress change following this major earthquake. I utilize this data to compare both the amounts of deformation and deformation gradients in exposed crystalline rocks versus sedimentary basins. This comparison was made with lithologic maps digitized from existing 1:62500 geologic maps (Dibblee, 1964a, 1964b, 1966, 1967a, 1967b, 1967c, 1967d, 1967e, 1970; Dibblee and Basset 1966a, 1966b).

3. Observations

3.1. Deflection of continuous planar markers within OFD zones

Continuous, formerly planar markers oriented at high angle to a fault provide the most complete picture of distributed displacement. Such markers record total magnitude of shear displacement, patterns of faulting and rigid body rotation, width of the OFD zone, and distribution of shear displacement within this zone. Figure 4 show maps of dikes and faults that are deflected as they approach the cross-cutting Calico fault. The convex shape of a set of Mesozoic aplite dikes indicates distributed shear displacement of 640 to 1100 m and suggests that distributed displacement increases nonlinearly toward the fault. Two kilometers to the north, Oskin et al., (2007) found a similar deflection of the west-striking Miocene Silver Bell fault, as it approaches the Calico fault (Fig. 4). They also show that the deflection of the fault increases nonlinearly such that 70% of distributed displacement occurs within 100 m of the Calico fault.

Detailed mapping of a set of mafic dikes located between these deflected markers next to the Calico fault further illustrates how shear displacement is accomplished within OFD zones. The dikes are contained within homogeneous quartz monzonite. Segmentation of the dikes illuminates the spacing of small faults that would otherwise be difficult to observe. Field measurements show that the length of dike segments (Fig. 5) decreases towards the

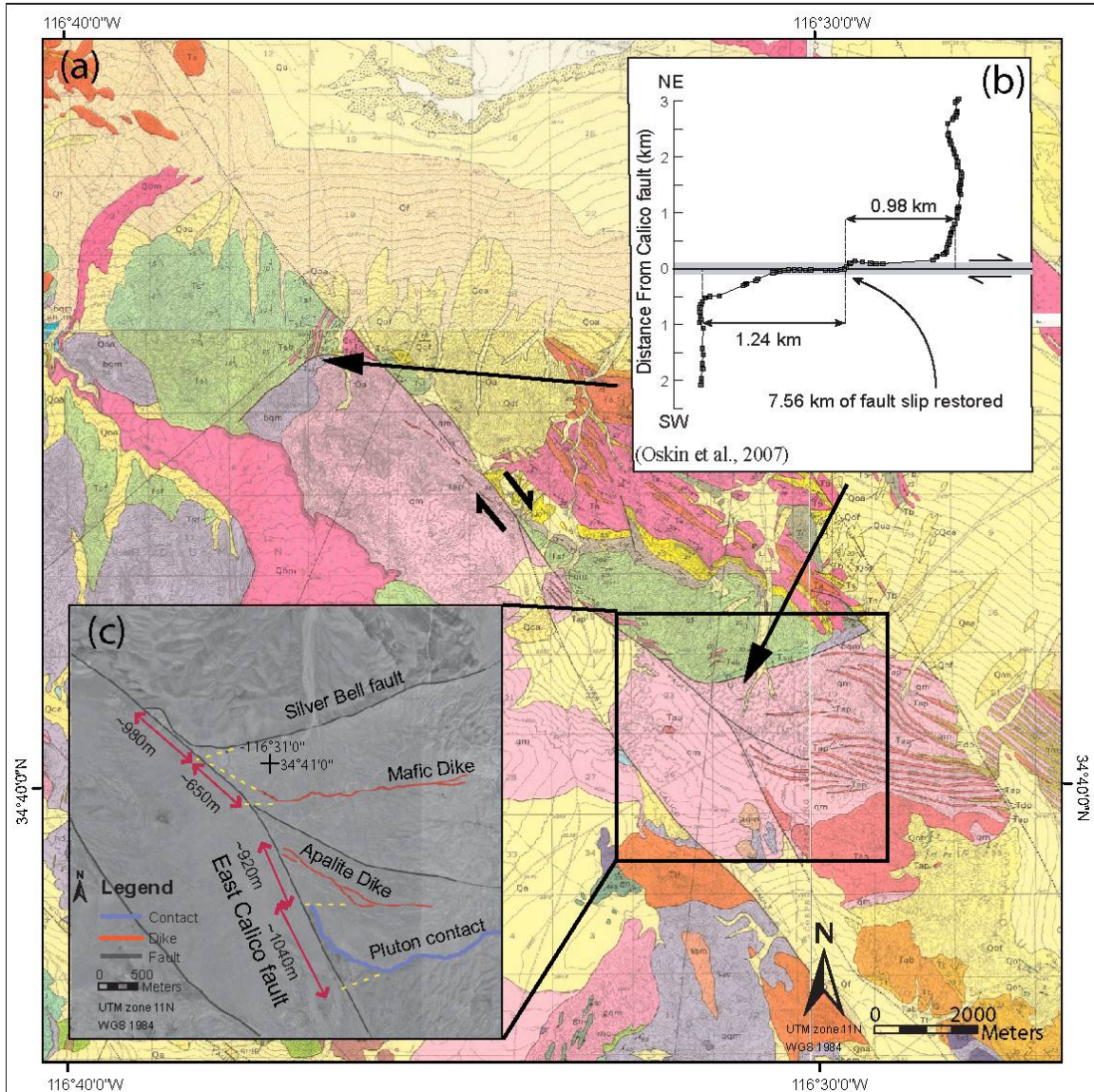
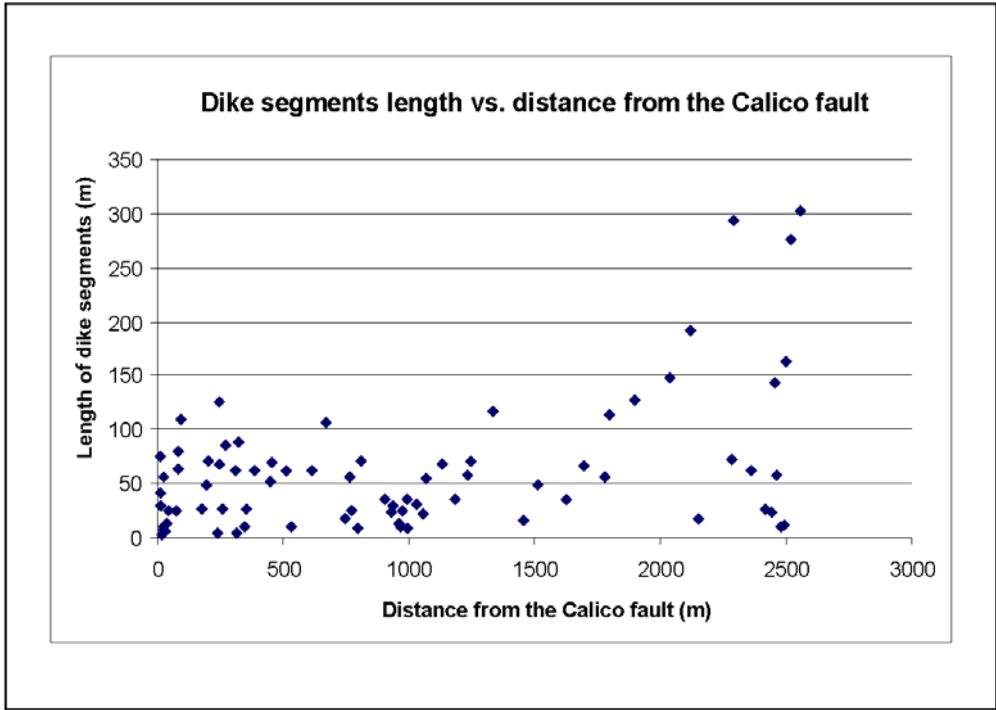


Figure 4. Deflected geologic features next to the Calico fault

(a) Geologic map (Dibblee, 1964a, 1964b) showing markers that are deflected approaching the Calico fault. (b) The deflected form of the Silver Bell normal fault (after Glazner et al., 2000 and Oskin et al., 2007). Arrows indicate the map location of the deflected fault. (c) Air photo of deflected dikes, fault, and contact next to the Calico fault.



fault. Mean dike segment length is 120 m >2000 m from the fault and only 47 m <2000 m from the fault (Fig. 5). In some cases, dike segments are separated by conjugate sinistral and dextral faults. Other segment boundaries may be due segmentation during dike intrusion (Baer and Reches, 1991) and thus unrelated to OFD.

3.2. Rotation of local linear markers within OFD zones

Unlike continuous markers, local linear markers, such as mylonitic lineation and paleomagnetic remanent direction, measure only a component of OFD via rotation. These measurements give insight into the mechanism of block rotation, the width of OFD zones, and the distribution and magnitude of displacement via rotation.

3.2.1 Mylonitic lineation

Measurements next to the Harper Lake fault (Fig. 6) show that on average, the trend of mylonitic lineations is rotated clockwise approaching the fault (Fig. 7). The amount and character of this rotation varies along fault strike. Observations (n=648, table A1) show increasing mean and variance of the azimuthal component of rotation values towards the fault (Fig. 7). Some upright folding along an axis parallel to the Harper Lake fault has been mapped (Fletcher et al., 1995). Tilting about a horizontal axis parallel to the fault is predicted to reduce the trend of mylonation from its far-field, unfolded trend. This prediction inconsistent with a plot of trend vs. plunge (Fig. 8), which suggests that orientation is not significantly affected by the tilting and thus that the clockwise rotation of mylonite trends predominantly records vertical axis rotation.

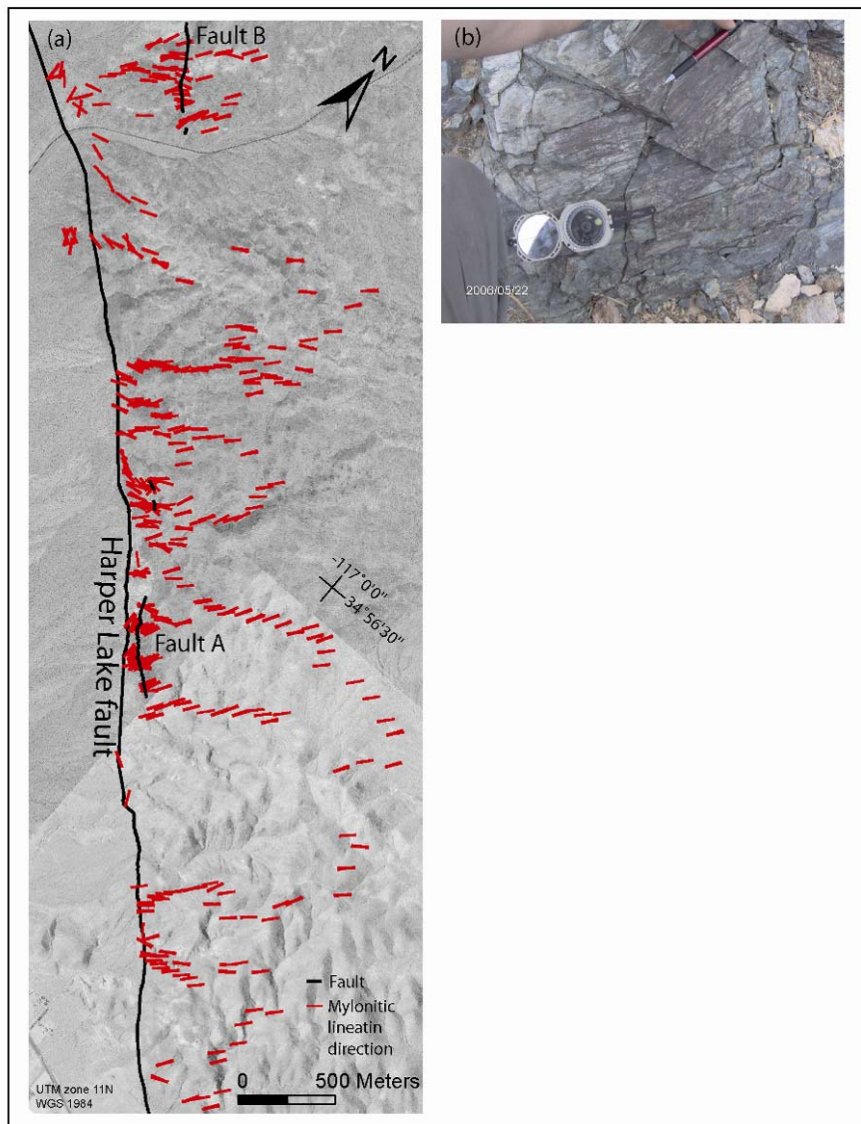


Figure 6. Map of mylonitic lineation measurements along the Harper Lake fault
 (a) Map of mylonitic lineation measurements along the Harper Lake fault. Short, solid red lines are measurements of mylonitic lineation directed according to their trend. Faults A, B are mapped segments of the secondary faults shown in figures 9 and 10. The few mylonitic lineations west of the Harper Lake fault are due to an isolated metamorphic outcrop at this side of the fault. (b) Field exposure of mylonitic lineation. The picture shows change in mylonitic lineation direction across a joint, probably due to brittle deformation that postdates mylonitization.

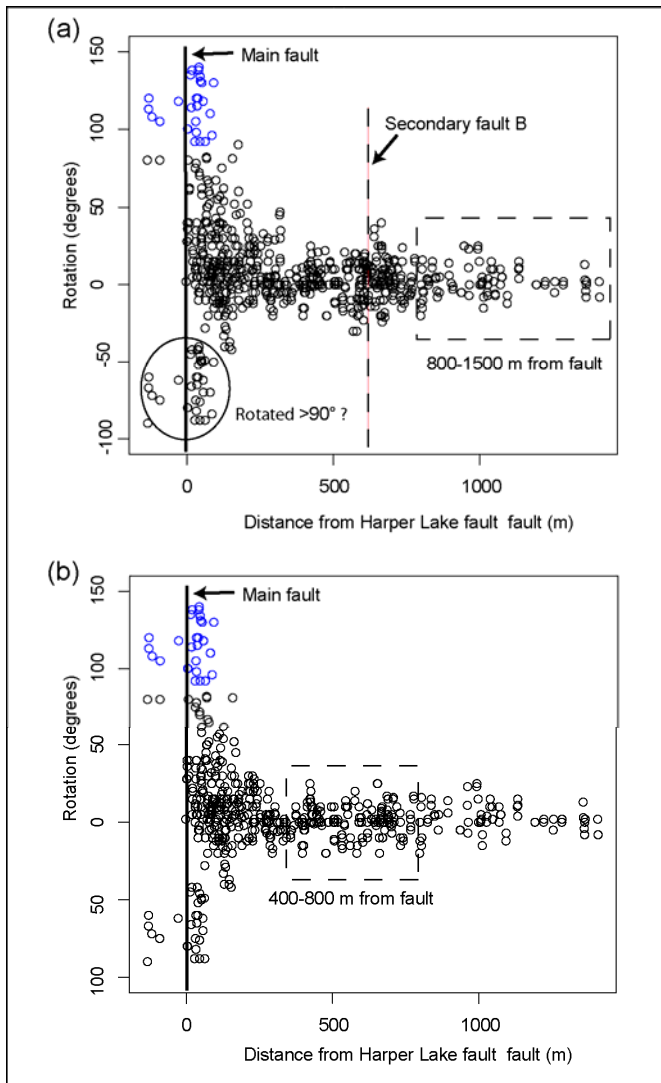


Figure 7. Mylonite rotation vs. distance from the Harper Lake fault

(a) Azimuthal component of mylonite rotation vs. distance from the Harper Lake fault. Rotation values are stacked along all 6.5 km of fault strike and limited to $\leq 90^\circ$. Rotation was calculated relative to the farthest point from the fault. Negative rotation values indicate counterclockwise rotation or rotation $> 90^\circ$. This group of points is replotted in blue as $> 90^\circ$ rotation. Note the area of approximately homogenous rotation values between 800-1500 m from the fault. The rotation values in this area have a standard deviation of 9° .

(b) The same as 7a, but after excluding the points at the northern part of the fault, next to secondary fault B (Fig. 6). The area of approximately homogenous rotation values between 400-800 m has a standard deviation of 10° . The similarity of the standard deviation values suggest that 9° - 10° is a typical standard deviation of rotation values in areas of homogenous rotation which are interpreted as one block.

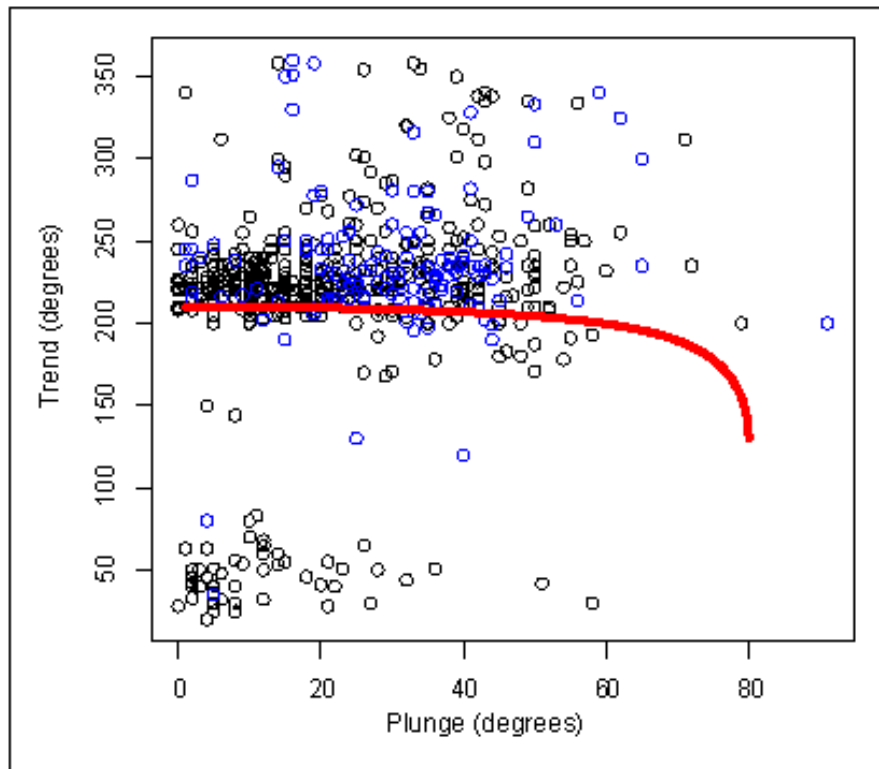


Figure 8. Trend vs. plunge of mylonitic lineation measurements

Trend vs. plunge of all measurements of mylonitic lineation direction (n=648) next to the Harper Lake fault. Blue points show a subset of the data for the northern 2 km of the study area. Red line represent the modeled trend vs. plunge, calculated for mylonitic lineations originally horizontal and trending 220° (the mean trend and plunge far from the fault) that are tilted about a horizontal axis parallel to the fault (trending 320°). The inconsistency between the data, dominated by trends $\geq 220^\circ$ and the model that predicts trends $< 220^\circ$, suggests a low dependency of the trend on the plunge.

Mylonitic lineation data also show that rotation occurs adjacent to secondary faults. Measurements along two transect lines (n=33) across a ~1.5 km-long secondary dextral fault (fault A, Fig. 6) show continuous rotation. This smoothly varying rotation also suggests that immediately adjacent to the fault mylonite rotation about vertical axis may exceed 90° (Fig. 9). Rotation starts 20-30 m from the fault and is approximately symmetric across it. Dispersed measurements of mylonitic lineation next to another secondary fault (fault B, Fig. 6) show ~15° difference in the azimuthal component of rotation across the fault (Fig. 10).

3.2.2 Paleomagnetic data

155 cores out of 165 cores drilled in four different areas gave stable magnetic vectors. results are presented in Table 1 and Figures 11 and 12. All but two of 23 sites investigated gave rotation values that cannot be distinguished significantly from zero (Fig. 11). A declination of $186^\circ \pm 5^\circ$ was measured for Site bfd06, sampled from basaltic flow 4 of the Black Mountain basalt (Oskin and Iriondo, 2004) adjacent to the Blackwater fault. All other sites in this area, sampled from basaltic flow 3, gave declinations of 180° to 174° that overlap within error. The slight declination anomaly of basaltic flow 4 may be a result of secular variation of the magnetic field and thus it is not certain whether it reflects actual rotation. Valentine et al., (1993) show paleomagnetic declinations in the Black Mountain basalt that are similar to those of site bfd06 and relate these to secular variation. Modest rotation of $10^\circ \pm 8^\circ$ was observed for site Lwp 3-4, sampled from Peach Spring tuff. This rotation is within error of most of the other sites next to the Lenwood fault as well as with the reference point (I=33°, D=36.4°, $\alpha_{95}=3.4^\circ$) determined by wells et al., (1989) at the Colorado Plateau.

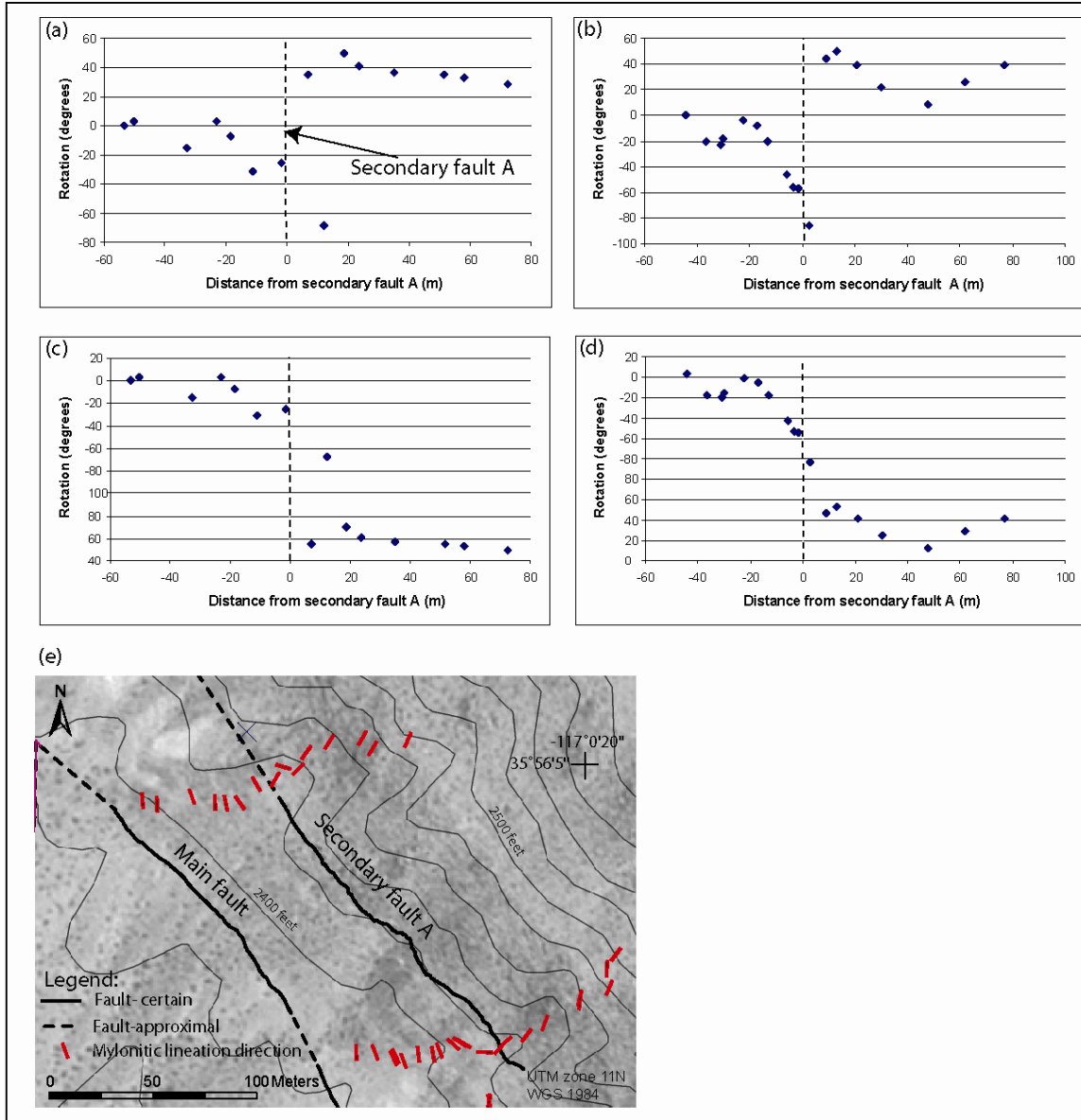


Figure 9. Mylonite rotation vs. distance from secondary fault A

Measurements of the azimuthal component of mylonite rotation vs. distance from secondary fault A next to the Harper Lake fault. Secondary fault and mylonitic lineation measurements were located with differential GPS. (a, b) Rotation values along two fault-normal transects. Rotation values are calculated relative to the westernmost point (leftmost point on the graphs) and are limited to $\leq 90^{\circ}$. (c, d) Rotation values along the same transects. Here, measurements east of the secondary fault are shifted (note the change in y axis) to illustrate the continuous pattern of rotation. (e) Map view of the two transects, transect (a, c) is the northern one.

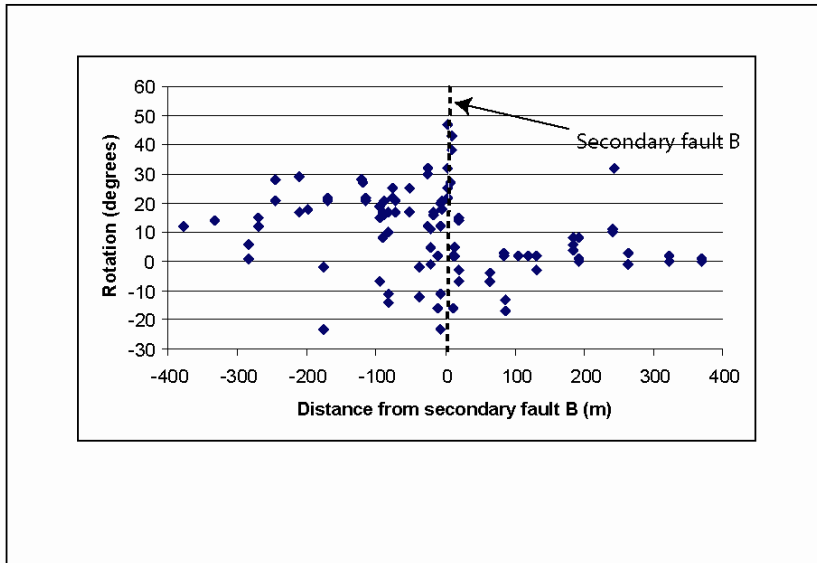


Figure 10. Mylonite rotation vs. distance from secondary fault B

Dispersed measurements of azimuthal component of mylonite rotation vs. distance from secondary fault B, located within the northern portion of the Harper Lake fault study area. Note the $\sim 15^\circ$ change of the rotation values across the fault. Negative rotation values may indicate counterclockwise rotation.

Site	Distance from fault(m)	Lithologic Unit	Age (Ma)	Declination (°)	Inclination (°)	α95	k	n/n ₀	Rotation (°)	Rotation Error (°)	Flattening (°)	Flattening error (°)	Latitude (°)	Longitude (°)	Tilt Correction	
															Strike	Dip
clav1	3080	Pipkin Basalt	0.77 ± 0.04 ¹	18.8	53.6	6.7	163.7	7/7	Reference Site			34.7586	-116.65441	none		
clav2	280			8.7	50.4	23.2	16.6	6/6	-10.1	28.1	-3.2	17.0	34.7775			-116.63398
clav3	140			6.3	43.7	8.7	92.1	8/9	-12.5	12.8	-9.9	8.5	34.7782			-116.63287
bw1	100	Black Mountain Basalt (unit 3)	3.77 ± 0.11 ²	173.6	-48.8	2.8	403.7	8/8	-3.5	5.3	3.7	3.3	35.1983	-117.19334	none	
bw2	220			180.2	-50.5	2.2	703.1	8/8	3.1	4.9	2.0	3.0	35.1968	-117.19356		
bw3	1280			179.0	-54.9	5.1	119.7	8/8	1.9	8.1	-2.4	4.7	35.1996	-117.20983		
bw4	391			179.5	-50.8	4.8	160.2	7/8	2.4	7.2	1.7	4.5	35.2049	-117.20252		
bw5	220			178.9	-49.6	4.4	156.0	8/8	1.8	6.7	2.9	4.2	35.2064	-117.20164		
bw6	3500			177.1	-52.5	3.2	301.1	9/9	Reference Site			35.2046	-117.14781			
bw7	500			173.9	-45.5	7.1	166.2	4/8	-3.2	8.7	7.0	5.9	35.1756	-117.16266		
bfd06	740	(unit 4)	3.74 ± 0.05 ²	186.4	-44.3	4.9	154.6	6/8	9.3	6.7	8.2	4.6	35.1925	-117.17934	314	25
bwn1	30	Black Hills Dacite	7.23 ± 1.07 ³	189.8	-33.9	14.3	23.7	5/8	-2.9	20.2	4.5	16.1	35.3504	-117.30122	247	6
bwn2	300			207.6	-37.4	11.2	81.8	3/3	14.9	18.5	1.0	14.5	35.3555	-117.29589		
bwn3	720			192.7	-38.4	15.5	13.8	7/7	Reference Site			35.3528	-117.29943			
lwp1	10	Peach Springs Tuff	18.5 ± 0.2 ⁴	28.5	51.1	10.4	47.8	6/6	-12.1	13.7	1.3	14.3	34.7581	-116.92631	70	10
lwp2	190			47.1	38.7	12.1	19.2	9/9	6.5	12.8	-11.1	15.1	34.7588	-116.92431		
lwp3-4	420			51.0	34.7	7.3	59.3	8/8	10.4	8.0	-15.1	13.1	34.7580	-116.92135		
lwp5	510			37.3	49.1	7.3	85.7	6/6	-3.3	9.6	-0.7	13.1	34.7568	-116.91971		
lwp6	710			37.9	47.8	6.0	85.2	8/8	-2.7	8.1	-2.0	12.7	34.7568	-116.91717		
lwp7	900			29.2	54.1	8.2	67.7	6/6	-11.4	11.7	4.3	13.4	34.7577	-116.91533		
lwp8	1070			37.6	47.9	8.0	57.5	7/7	-3.0	10.2	-1.9	13.3	34.7575	-116.91325		
lwp9	1210			41.8	43.0	9.1	44.7	7/7	1.2	10.6	-6.8	13.8	34.7583	-116.91197		
lwp10	1430			40.6	49.8	5.9	90.3	8/8	Reference Site			34.7585	-116.90984			

Note: Line and plane fits for each sample were calculated following Kirschvink (1980). Site mean directions were calculated following Fisher (1953) and tilt correction applied, if any. Rotation and flattening were determined following the methods of Beck (1980) and Demerutis (1983) by using the furthest site from the fault as a reference site. Unit 3 of the Black Mountain basalt was correlated to areas not mapped by Oskin and Iriondo (2004).

¹Oskin et al. (2007)

²Unit 3 of Black Mountain Basalt is confined between units dated 3.77±0.11 Ma unit 2 and 3.74±0.05 Ma unit 4. Because the older age overlaps the younger including uncertainty, 1 this age is cited for unit 3.

³Oskin and Iriondo (2004)

⁴Nielson et al. (1990)

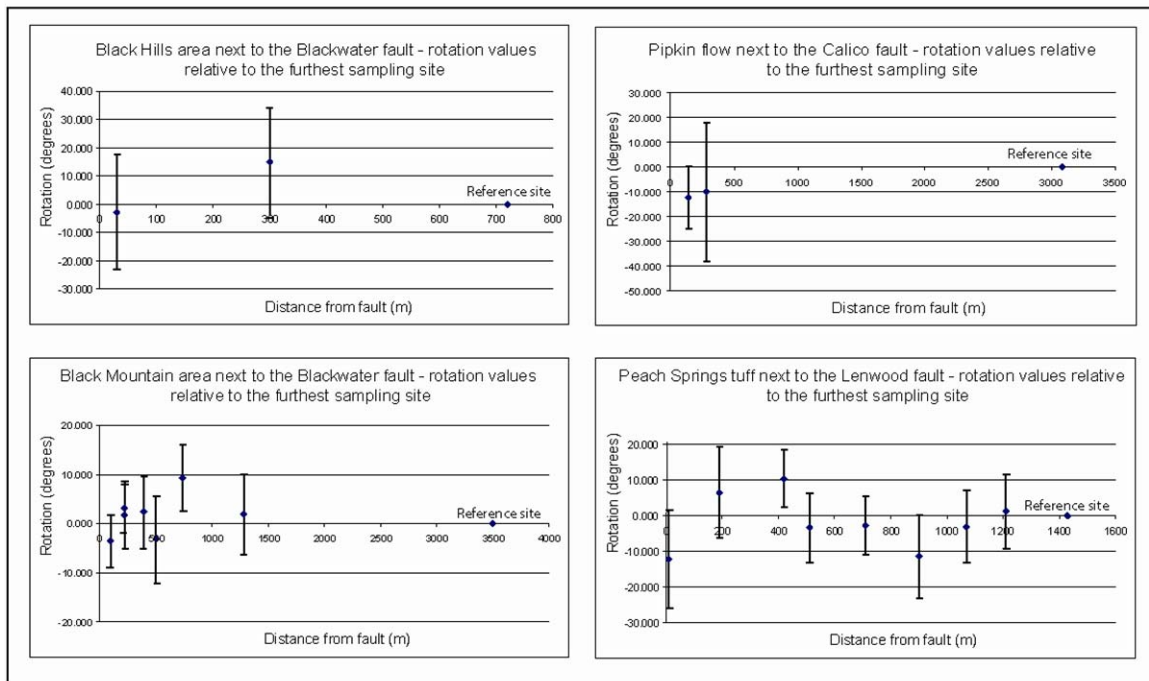


Figure 9. Rotation values for paleomagnetic sites

Rotation values for paleomagnetic sites next to the Calico, Blackwater and Lenwood faults. See Figure 2 and Table 2 for site locations. Rotation values are calculated relative to the furthest measurement site from the fault. Negative rotation values indicate counterclockwise rotation. Rotation errors are calculated according to Demarest (1983).

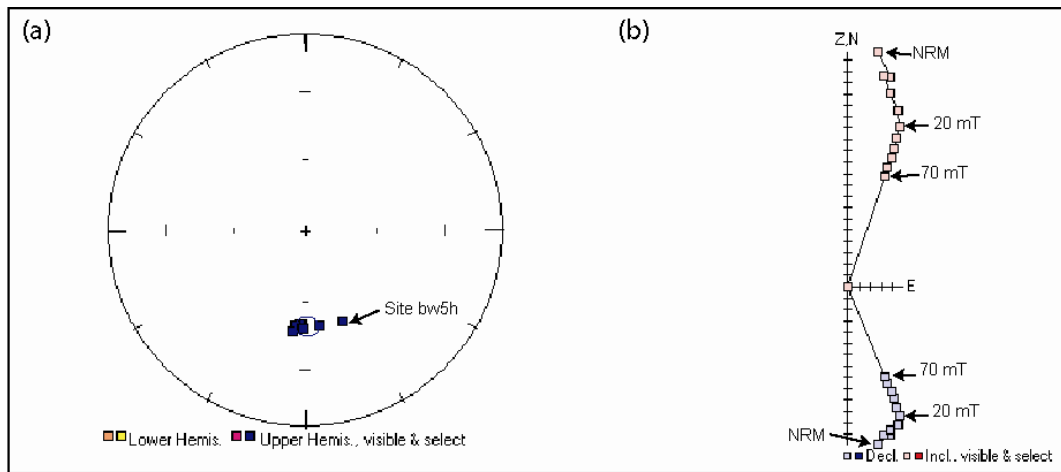


Figure 10. Example plots of paleomagnetic analysis

(a) Example of equal area plot for site bw5 next to the Blackwater fault. Black cycle represent α_{95} confidence limit around site mean ($I=-44.6^\circ$, $D=178.9^\circ$, $\alpha_{95}=4.4^\circ$). (b) Example of Zijderveld diagram presenting alternating field (AF) demagnetization of sample bw5h ($I=-49^\circ$, $D=157.7^\circ$, MAD (maximum angular deviation) = 1.4°). Note stabilization of the magnetization direction at AF field above 20 mT. Divisions are 10^{-3} emu/cm³.

3.3. Distribution of and offsets along secondary faults within OFD zones

Measurements of fault distribution provide insights into the width, level of activity, mechanism, and distribution of displacement in OFD zones. Mapping of the Pisgah fault zone where it cuts two flows of the Sunshine Peak basalt field shows abundant secondary faulting that extends up to ~400 m from the main fault trace (Fig. 13). Secondary faults cutting both flows form scarps up to several meters high and oriented ~30° relative to the main Pisgah fault, consistent with Riedel shears. In general, these faults are exposed in uplifted, folded areas (Fig. 13). Some of the secondary faults can be followed through the volcanic units into the underlying basement and sedimentary rocks. In order to evaluate the activity of OFD, samples of both flows were dated via $^{40}\text{Ar}/^{39}\text{Ar}$ at the University of Wisconsin (Fig. 14, Appendix 3). Tuff deposits overlain by the 752 ± 110 ka Lavic Lake lava flow are offset by 785 ± 125 along a well-defined fault trace. Channels incised in the 169 ± 29 ka Sunshine peak basalts are offset only 130 ± 70 m.

Next to the Harper Lake fault, secondary fault B, located parallel to and 600 to 800 meters east of the main fault, offsets multiple lithologic contacts by 179 ± 6 m (fault B in Fig. 6, Fig. 15). This fault also offset an alluvial fan by 13 ± 2 m at $117^{\circ}1'37.31''\text{W}$ $34^{\circ}57'24.9''\text{N}$ (Fig. 15).

3.4. Seismic refraction survey

Figures 16 and 17 show location and first arrival times, respectively, for five seismic refraction lines sequentially deployed next to the Calico fault. Four of these lines were deployed within a tributary of Silver Canyon wash and a fifth line was deployed within

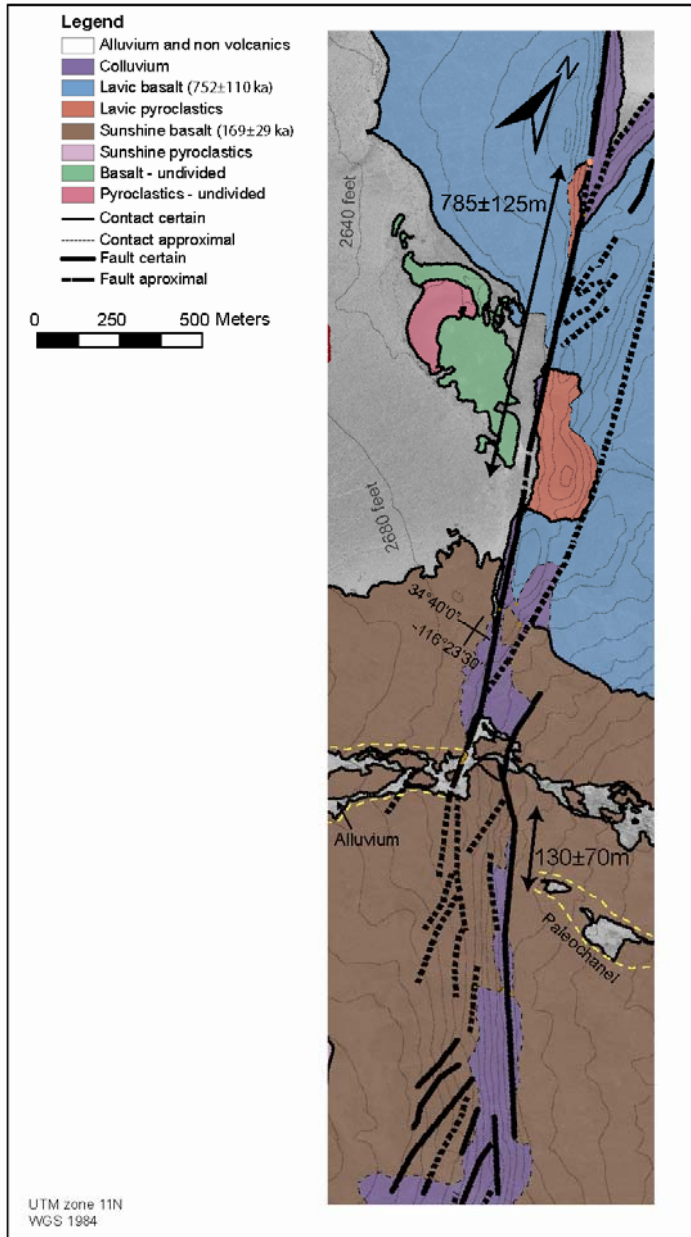


Figure 11. Map of the Pisgah fault in the Sunshine Peak basalt field

Interpreted air-photo map of the Pisgah fault where it cuts the Sunshine Peak basalt field. Pyroclastic rocks overlain by the Lavic Lake basalt flow are offset by 785 ± 125 m along a well-defined fault trace. Channels established across the 169 ± 29 ka Sunshine peak basalt flow are offset only 130 ± 70 m. Note the concentrations of secondary faults southwest and northeast of the fault. Both of these localities coincide with folding of the basalt flows.

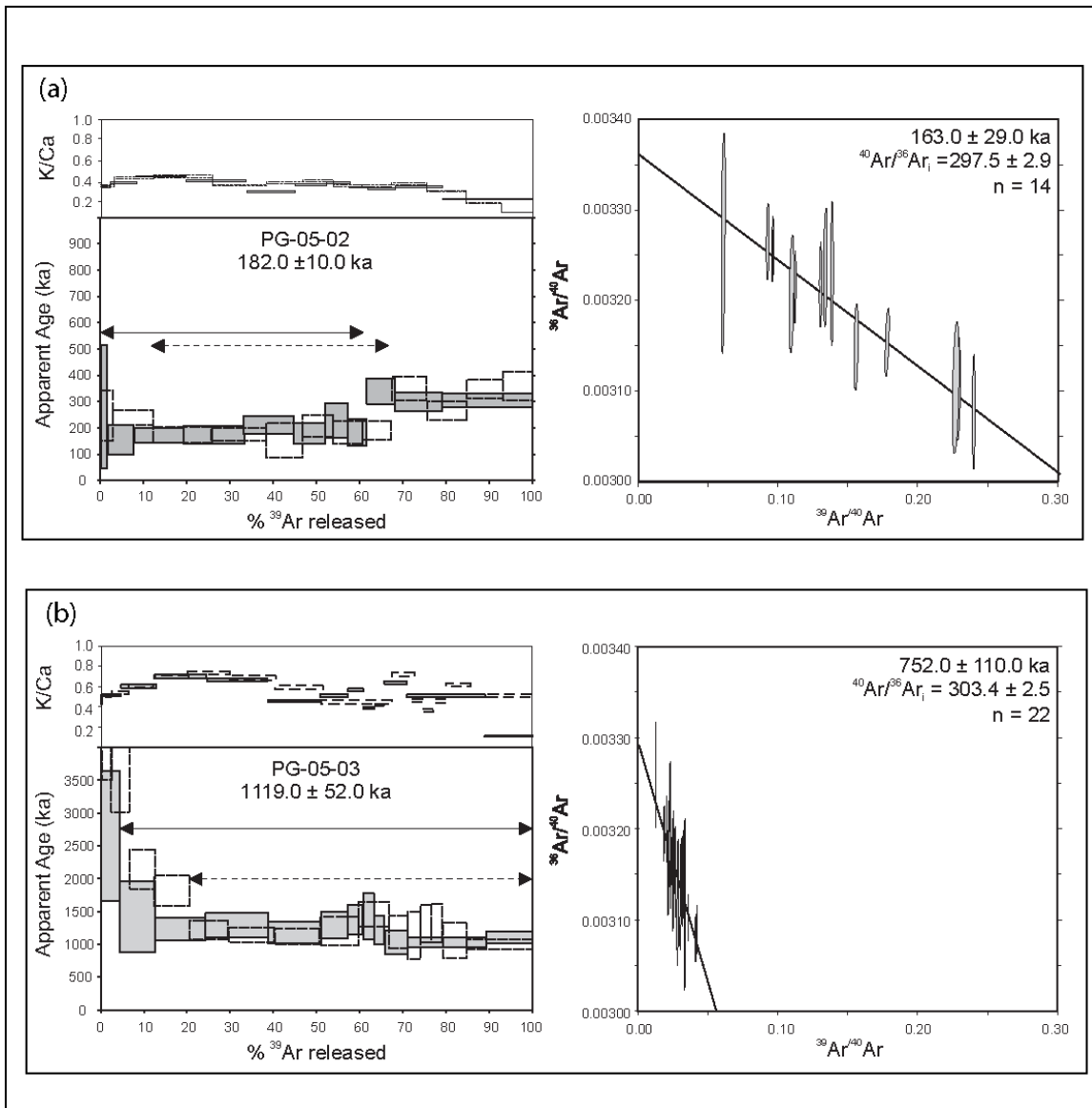


Figure 12. $^{40}\text{Ar}/^{39}\text{Ar}$ dating of the Sunshine and Lavic basalts

Apparent age spectra and K/Ca release patterns (left) and inverse isochron diagrams (right) for replicate analyses of samples PG-05-02 (14a) and -03 (14b) of the Sunshine and Lavic basalts respectively. Portions of the spectra that yielded age plateaus are shown by the arrows. Only these plateau data are combined to calculate the isochron ages shown at the right (data from individual experiments normalized to a common J value for illustrative purposes only). The regression for sample PG-05-03 yields a y-intercept value with a $^{40}\text{Ar}/^{36}\text{Ar}$ ratio of 303.4 ± 2.5 , implying that this lava contains a significant quantity of excess argon. The isochron ages therefore give the best estimates of time since these lavas erupted.

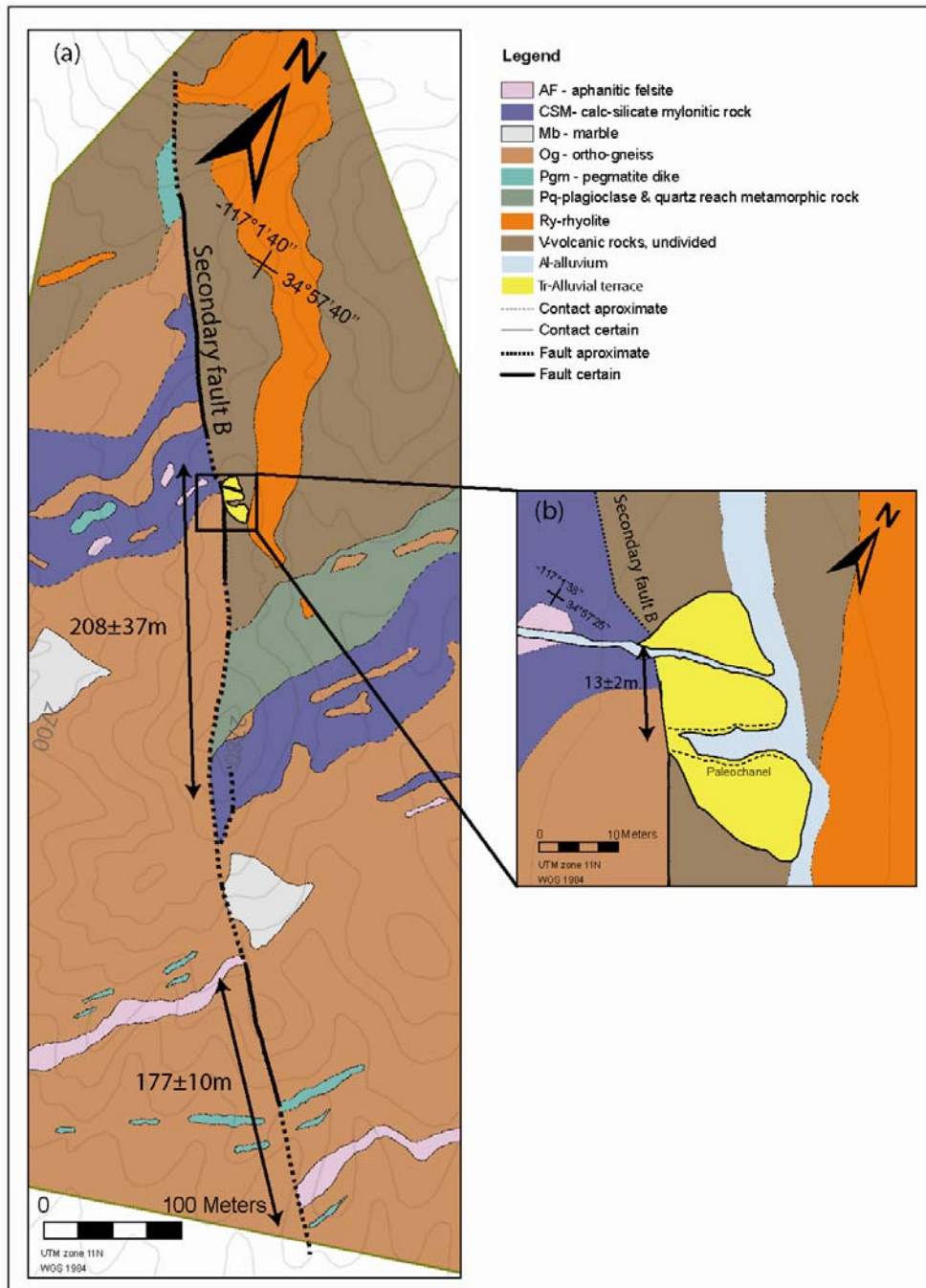


Figure 13. Map of offset contacts next to secondary fault B

(a) Geologic map of lithologies offset by secondary fault B, located near the Harper Lake fault. Arrows mark offset of pegmatite dike (Pgm) and of calc-silicate mylonitic rock. Note that the marble (Mb) and rhyolite (Ry) units are also offset. (b) Map of stream channel incised into an alluvial fan and offset $13 \pm 2m$ by secondary fault B.

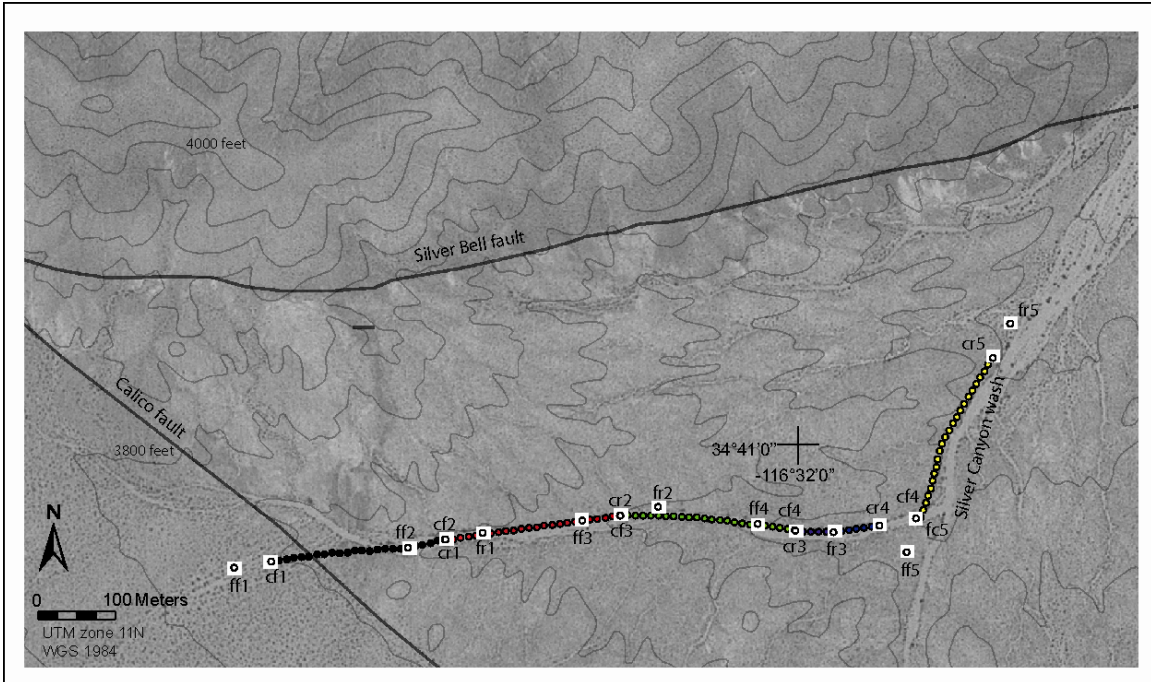


Figure 14. Index map of seismic refraction lines

Index map of refraction lines. Circles represent geophones and are colored by line. Circles within squares are shot points. Shot point naming scheme is: first letter for close-c or far-f, second letter for forward-f or reverse-r, the following number is the line number.

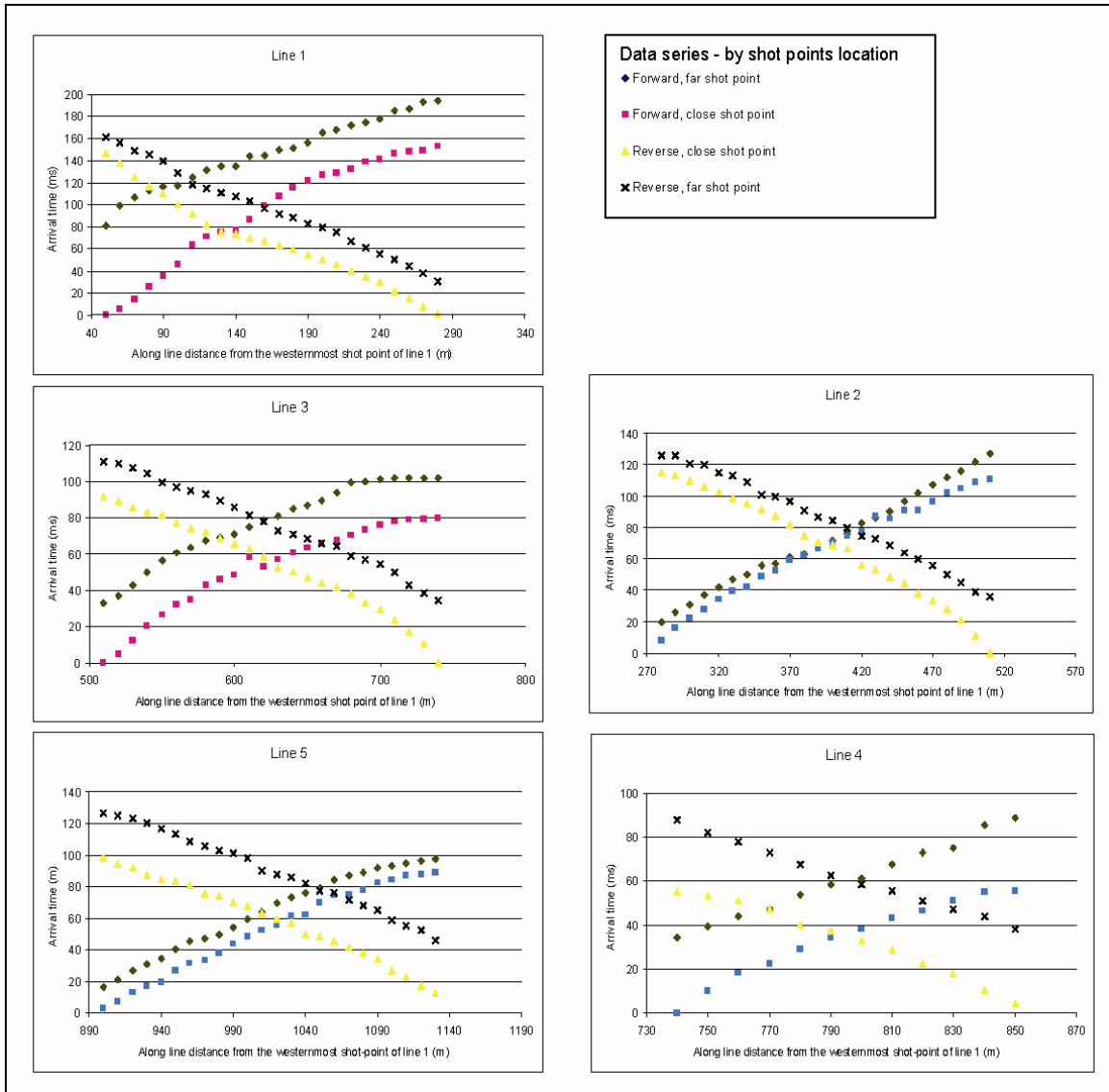


Figure 15. First arrival time vs. distance for seismic refraction lines

First arrival time vs. distance for five seismic refraction lines located NE of the Calico fault. Each data series correspond to a specific shot point and named using the forward-reverse, close-far, terminology described in 3. Arrival times are plotted with respect to the distance from the westernmost geophone for all seismic refraction lines.

Silver Canyon wash itself. Bedrock was exposed intermittently in the floor of the tributary, thus I interpret that depth of alluvium within the tributary is insignificant to the refraction survey. All lines except for line 1 display various degrees of negative curvature (e.g. concave-down) for all four shot points. Negative curvature is consistent with a continuous increase of seismic velocity with depth. Line 1, located immediately east of the Calico fault, displays negative curvature for the 2 shot-points located close to the fault and positive curvature for the 2 shot-points located away from the fault.

For simple velocity structure where velocity increases with depth, the arrival time from the far shot points to the closest geophone will be similar for either end. The data show differences in arrival time of up to 51 ms (Fig. 17). Delay in triggering the recording system may cause some difference in arrival time. For example, the close shot-points of lines 2, 4, and 5 yielded relatively late arrival times of 3 to 12 ms for the first geophone (Fig. 17), located within one meter of the shot point. These delays are almost certainly due to mechanical delay in triggering the recording system. Such mechanical delay could explain arrival time differences of <16 ms between the far shot point and the closest geophone observed for lines 2, 3, and 4 (Fig. 17). However, for lines 1 and 5 this difference is 51 and 31 ms respectively, a delay that far exceeds the mechanical delay. I attribute the extra delay for line 5 to placement of one of the far shot-points on exposed granite and the other on thick alluvium cover in Silver Canyon wash. Line 1 display a longer arrival time for the far shot-point located next to the Calico fault. This delay may be due to thicker alluvial cover west of the Calico fault. Alternatively, the delay may be attributed to a low-velocity zone near the fault.

4. Data analysis

4.1. Analysis of mylonitic lineation directions adjacent to the Harper Lake fault

I use the mylonitic lineations data set adjacent to the Harper Lake fault to quantify the style and amount of distributed shear deformation accomplished through rotation. First, I focus on the variance of mylonite directions and show that this variance increases towards the fault. Then I use this variability to constrain the maximum sizes of hypothetical fault-bounded blocks that make up the zone of distributed displacement. Using these block dimensions, I estimate the density of secondary faults within the OFD zone. I then integrate over the blocks to quantify the amount and distribution of distributed deformation.

4.1.1. Variability of mylonitic lineation directions as function of distance from the fault

To quantify patterns of block rotation next to faults I used simple statistical tools to analyze the variability of the mylonite rotation next to the Harper Lake fault. Measurement points were grouped into 100 m-wide bins from 0 to 700 m from the fault, and an 800 m wide bin between 700 to 1500 m from the fault where the spatial density of measurement points is lower. I then applied the Fisher precision parameter (k) and α_{95} (Fisher, 1953) to quantify the 3-D variability of mylonite rotation in each bin. Analysis of all the mylonitic measurements (Fig. 18) shows a nonlinear increase in variance towards the fault described by

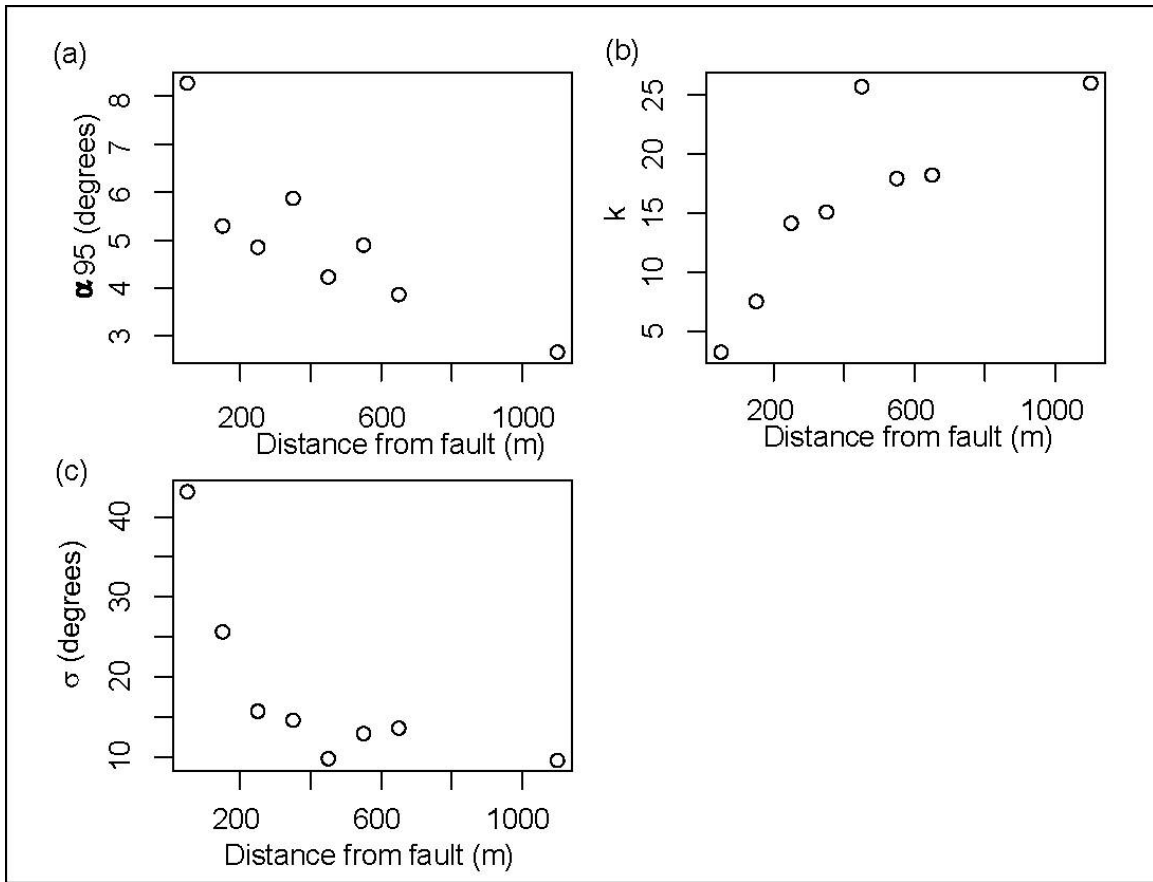


Figure 16. Mylonitic lineation variance vs. distance from the Harper Lake fault

(a, b) Graphs of Fisher statistical measures of variance versus distance from the Harper Lake fault - (a) - α_{95} , (b) fisher precision parameter, k . These parameters are based on a vector sum of mylonite rotation measurements stacked within a 6.5 km-long fault-parallel bin. Bins are 100 meters wide within 700 m from the fault, and 800 meters wide beyond this range where data-points are sparse. Higher α_{95} values and lower k values indicate greater scatter of mylonite rotation. (c) Standard deviation of the azimuthal component of mylonite rotation for the whole mylonitic lineation direction data set. The rotation values are divided into bins by distance from the Harper Lake fault as in (a, b).

increasing α_{95} values and decreasing k values. Focusing on the azimuthal component of rotation alone, I also find that variability increases towards the fault (Fig. 18). Applying this analysis for different segments along fault strike shows different patterns of variability for each segment (Fig. 19).

4.1.2. Calculation of maximum block dimensions within the OFD zone

I use the azimuthal component of mylonite rotation values to estimate the sizes of rigid blocks that comprise the OFD zone. I first assume that there is a zone of low rotation variability (Fig. 7) starting at ~ 800 m away from the fault. This zone is considered one rigid block with a representative Gaussian distribution of mylonite rotation. Then, the variance of the azimuthal component of rotation for this zone ($2\sigma=18^\circ$) is used as an estimate of the permissible variance within smaller rigid blocks within the OFD zone. I calculate 2-D block dimensions in several steps using a computer program to analyze all possible combinations of points that make up blocks. First, I choose a measurement point and compare its azimuthal component of rotation value to its closest neighbors ordered by distance. When I find a point that has a rotation angle that differs by $>2\sigma$, I interpret its distance as the distance between points located on different blocks. I then back up to the previous point compared, which is the furthest of a continuous set of distance-ordered points with rotation values that differ by $\leq 2\sigma$ from the measurement point. I interpret this distance (L) as a possible measure of the furthest distance between points located on the same block. Repetition of this process for all measurement points in the data set provides each point with an associated L value.

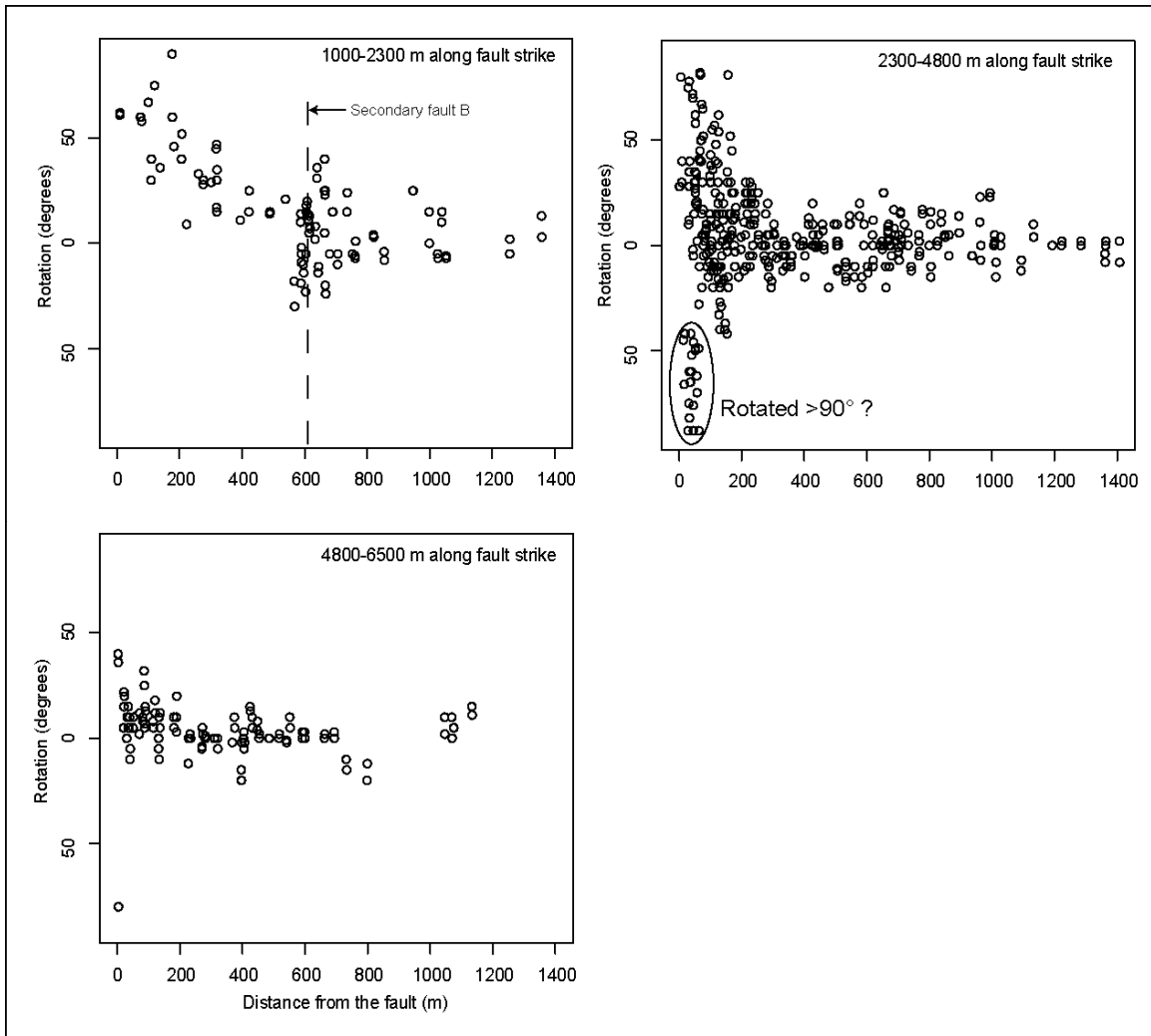


Figure 17. Patterns of mylonite rotation along segments of the Harper Lake fault
 Different patterns of the azimuthal component of mylonite rotation along portions of the Harper Lake fault. Upper right corner of each graph shows location of the subset of data shown as distance along the Harper Lake fault measured from NW end of study area. The middle section shows a group of points, immediately adjacent to the fault, that are apparently rotated counterclockwise. These points are likely to be actually rotated $>90^\circ$.

Figure 20 shows circles of radius L centered at each one of the measurement points. If block dimensions are much larger than the spacing between measurement points, and if each rigid block is distinguished from the surrounding rigid blocks by rotation angles $>2\sigma$, then L values from a particular block should be largest for measurement points nearest the center of the block. Hence, the largest L value per block (L_{\max}), is a gross approximation of the half-length of the shortest axis of a block.

To estimate L_{\max} , I have to exclude all L values measured from data points located close to block margins (Fig. 21). This is done by excluding all L values that are included entirely within larger blocks. These L values are illustrated in Figure 20 by small circles included within larger ones. Partly overlapping circles are not excluded because they represent different possible block configurations. Figure 21 also shows that the spatial pattern of block dimensions changes along fault strike. The northern portion of the fault has more small blocks next to the fault than the southern portion. I exclude L_{\max} values determined for blocks that include less than 10 measurement points in order to reduce the effect of erroneous measurements such as those taken from rocks that are not in-place. This also excludes very small blocks from the analysis. Because small blocks are expected to infill spaces between the larger blocks, characterizing the distribution of largest blocks gives an overall measure of the degree of fragmentation of the OFD zone.

The half-length of the shortest axis of blocks (L_{\max}), combined with the distance (X) between the fault and the middle of the shortest axis (the center of the circles in Figure 21) provides an estimate of largest block dimensions as function of distance from the fault. A plot of L_{\max} vs. X (Fig. 22), stacked along 6.5 km of fault strike, shows

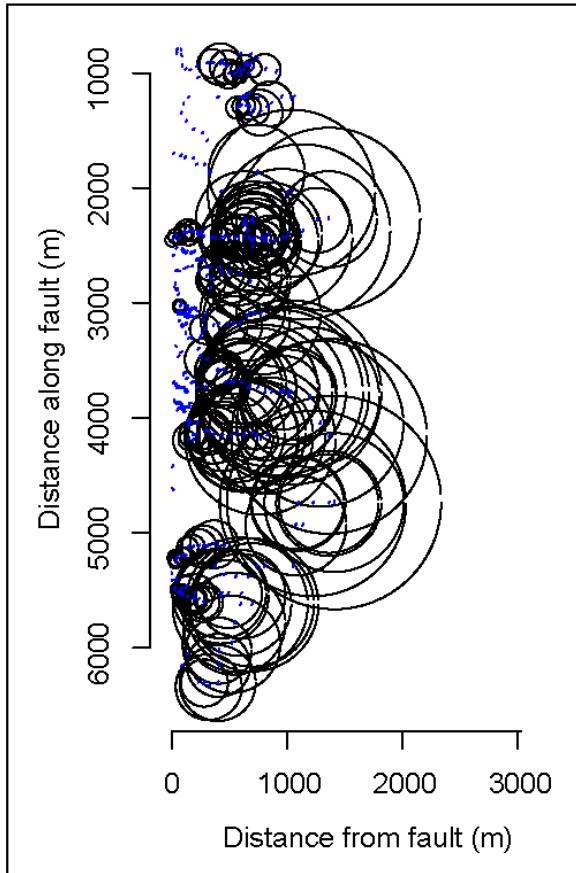


Figure 20. Analysis of block radii

Circle of radius L centered at mylonitic lineation measurement point where at least nine adjacent points had azimuthal component of rotation values within 2σ . L value is interpreted as the distance between points located on the same block. Distance along fault is measured southward from the northern edge of the Harper Lake fault in the study area.

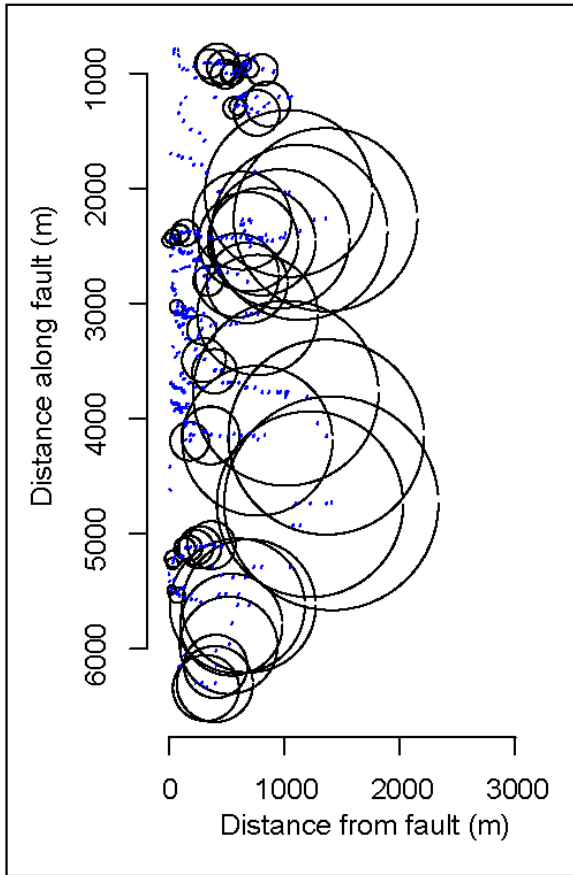


Figure 18. Analysis of block radii - sorted

Circles of radius L_{\max} , centered at a measurement point that is interpreted to be near the middle of the shortest axis of a block. L_{\max} is found by excluding all possible blocks (e.g. circles) that are enclosed within other possible blocks. As in Figure 20, I exclude all L values that include less than 10 measurement points. Distance along fault is measured southward from the northern edge of the Harper Lake fault in the study area.

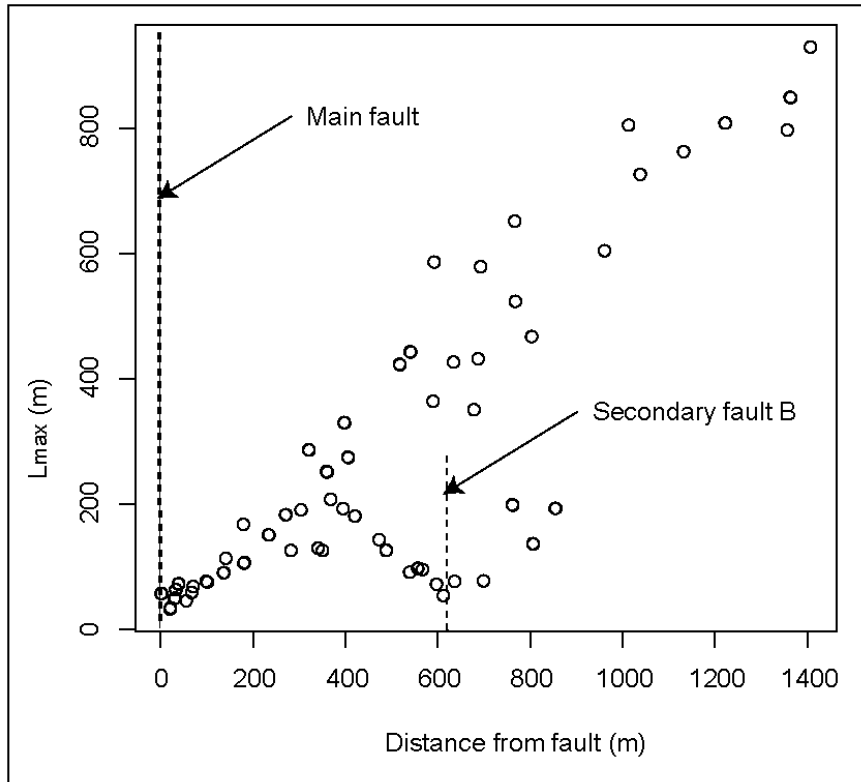


Figure 19. Block radii vs. distance from the Harper Lake fault

A plot of L_{\max} versus distance from the fault (X) shows that block dimensions decrease towards the fault. The outlying set of data points with low L_{\max} values at 400-800 m is interpreted to be due to the effect of secondary fault B.

continuous decrease of block dimensions towards the fault. The outlying set of data points with low L_{\max} values at 400-800 m from the fault may be due to secondary fault B (Fig. 6). To estimate the affect of the spatial distribution of mylonite measurement on the clear trend seen in Figure 22, we replaced the actual rotation data set with randomly generated Gaussian data set ($\sigma = 9^\circ$), and applied the same analysis procedure on the random data set. Results (Fig. 23) indicate that although there is some affect of the spatial distribution of the measurements, the analysis provides reliable outcome.

In order to estimate a relationship between distance and maximum block size, the outlier dataset associated with the secondary fault is excluded (Fig. 24). All points within 800 m from the fault provide regression of $L_{\max}=16.3+0.67X$, $R^2=0.87$, slope error = 0.03. All points within 400 m from the fault provide regression of $L_{\max}=30+0.56X$, $R^2=0.84$, slope standard error = 0.04 (Fig. 24). Theoretically - L values larger than X should not occur since the main fault should define a block boundary, however the analysis identified possible blocks within 100 m of the fault that violate this constraint. The regression line obtained by excluding these points is $L_{\max}=-4+0.71X$, $R^2=0.85$, slope standard error=0.05, and $L_{\max}=15+0.61X$, $R^2=0.81$, slope standard error = 0.06, for data within 800 m and 400 m from the fault, respectively (Fig. 24). Note that intercept for block size at the fault is insignificant from zero.

The distribution of block sizes can be used to estimate the width of the OFD zone. For example: at a large distance from the OFD zone, there should be essentially one large block with a homogenous rotation value. Thus, $L_{\max f}$, the block radius associated with the outermost measurement point, should be approximately equal to X_f (the distance of the furthest measurement point from the fault) minus the width of the OFD zone (W).

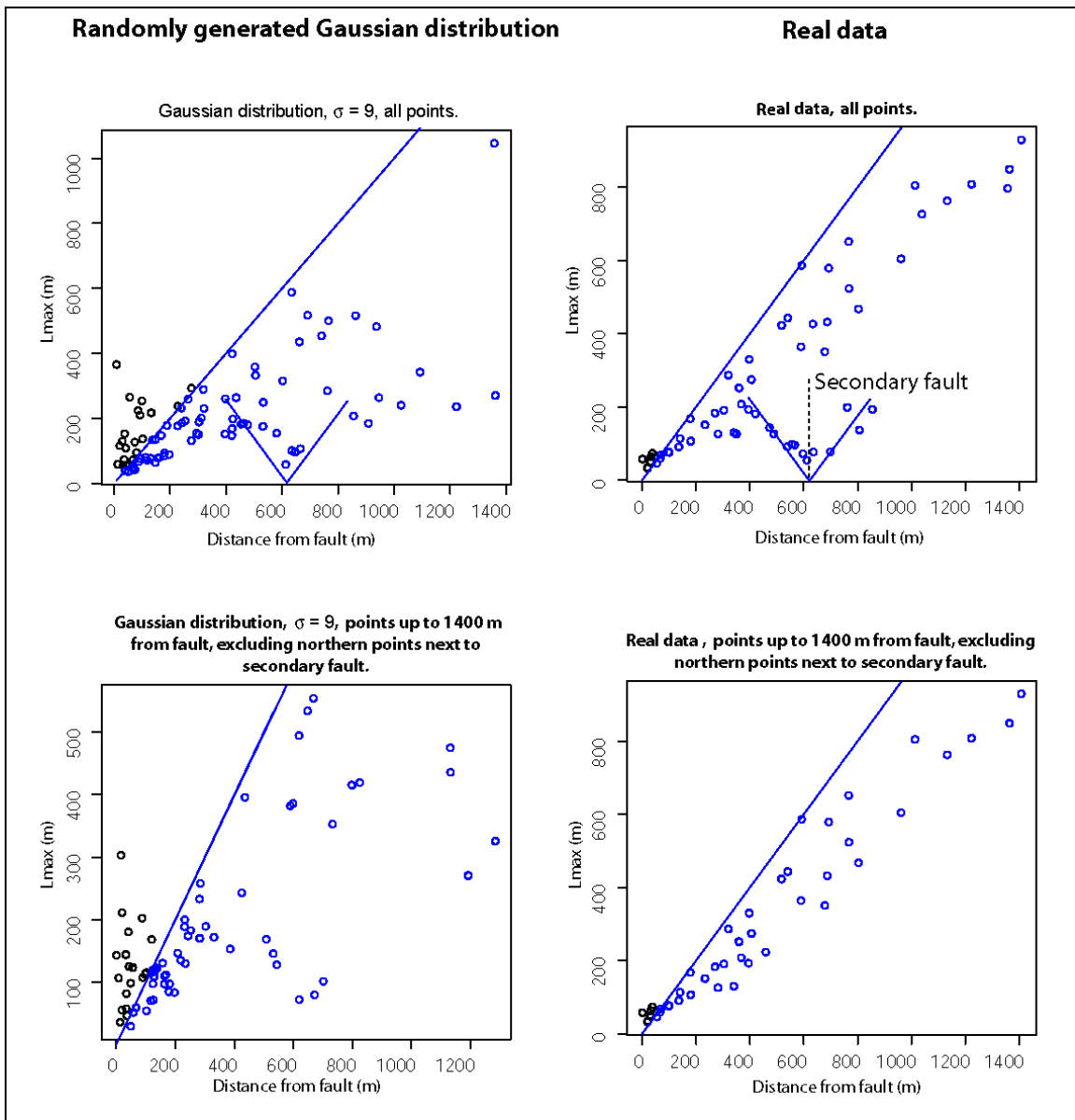


Figure 20. Comparison of real data vs. randomly generated data

Comparison of block size analysis (based on the process described in section 4.1.2) using real data vs. randomly generated Gaussian distribution. In the processing I used value of $2\sigma=18$, as a way to distinct between blocks. Blue lines are lines of slope = 1, plotted respective to the main fault so it transects the x-axis at 0. Black points are points above this line. The trend seen in the randomly generated data, indicate that there is some affect to the spatial distribution of the measurements. However, the more distinctive trend of the real data, as well as the small number of L_{max} values above the line of slope 1 (an unrealistic block size), indicate that the method we followed may be considered reliable.

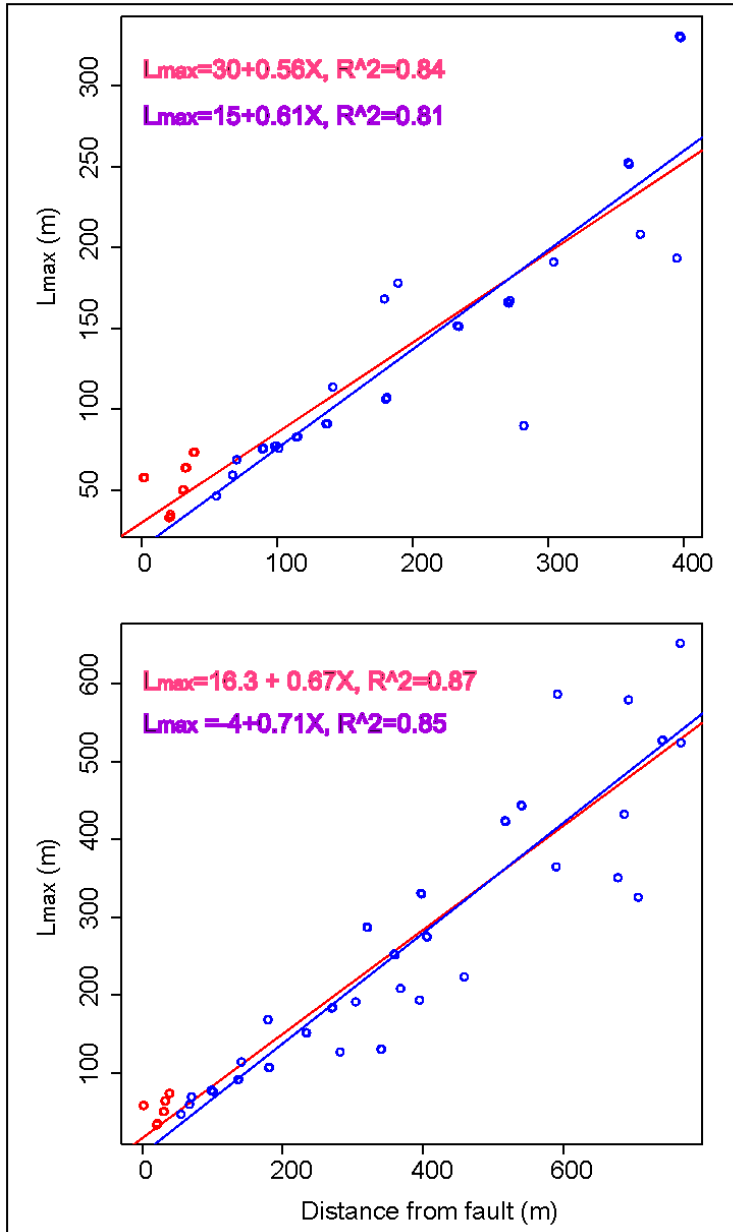


Figure 21. Block radii vs. distance from the fault, excluding secondary fault
 Plot of L_{max} versus distance from the fault (X) for 800m-wide and 400m-wide OFD zones. L_{max} values for points next to secondary fault A are excluded from this plot. Red circles represent L_{max} values where $L_{max} > X$. These are interpreted to be unrealistic because they imply a block that overlaps the main fault. Red and blue regression lines correspond to fits to the data with and without the measurements where $L_{max} > X$, respectively.

Because I exclude smaller blocks (smaller values of L) contained entirely within larger blocks, the area outside of the OFD zone can also be identified by a gap between the outermost point and the center points of the rest of the blocks. Such a scenario is shown in Figure 25 where L_{\max} values are plotted versus X for the southern portion of the study area. Here, the furthest point is located ~ 1400 m away from the fault and has a size of ~ 1000 m. At this position, I estimate the width of the OFD zone,

$$W \approx X_f - L_{\max} = 1400m - 1000m = 400m.$$

4.1.3. Secondary fault density within the OFD zone

The ratio between the length of secondary faults and the main fault, if secondary faults are active during seismic events, is important in order to understand the role of OFD as a sink of seismic energy. I estimate this ratio (i.e. the secondary fault density) by calculating the cumulative circumference of blocks bounded between the main fault and the outer margins of the OFD zone. To do this I assume that the blocks are circular and have a radius of L_{\max} . Because L_{\max} is an estimate of the half-length of the short axis of blocks, this approach will overestimate the density of secondary faults if blocks are elongate. However, I also neglect smaller blocks that are certain to lie between larger ones, as well as subhorizontal faults that may bound some blocks. Thus, overall the estimate of secondary fault density is conservative. The distribution of block sizes estimated in the previous section is used to calculate the minimum number of blocks within the OFD zone. Then, I use the cumulative circumference of these blocks, per unit length along the fault as a measure of secondary fault density.

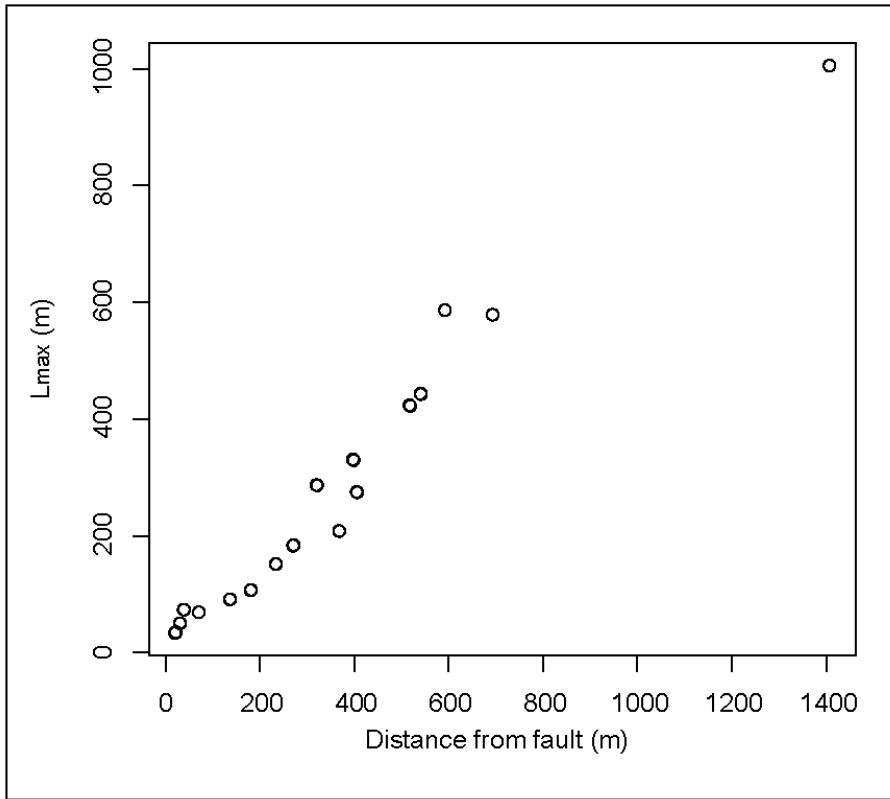


Figure 22. Block radii vs. distance from the southern section of the fault

L_{max} versus distance from the fault (X) for the southerly set of measurement points (located at 4500 to 6500 m along fault strike). Note the gap between the farthest most point and the rest of the data.

In order to calculate the cumulative circumference of blocks within the OFD zone I find the number of blocks, n , over a distance, X , where block radius, L_{\max} , increases as a function of X (Fig. 24). The minimal number of blocks (n) within the OFD zone occurs when blocks are arranged side by side as shown in Figure 26a. The right triangles, defined by the center and radii of these blocks are used to derive a geometric relationship for n . Figure 26b shows that $L_{\max}=mX$ defines the height of the triangles.

The triangles HX_1E , FX_2G are isosceles right triangles due to the circular shape of the enclosing blocks. Thus, triangles HX_1E , FX_2G are also similar triangles and therefore the following ratios are equal for a pair of adjacent blocks (Fig. 26b):

$$(1) \frac{L_{\max 2}}{L_{\max 1}} = \frac{\overline{X_2 G}}{\overline{X_1 G}} = \frac{mX_2}{mX_1} = \frac{X_2}{X_1} = \frac{\overline{GF}}{\overline{EF}}.$$

The triangle EGF is also right triangle. The tangent of angle GEF is thus also equal to this set of ratios,

$$(2) \frac{L_{\max 2}}{L_{\max 1}} = \frac{X_2}{X_1} = \frac{\overline{GF}}{\overline{EF}} = \tan(\angle GEF) = \tan\left(\frac{\pi}{4} + \theta\right),$$

where $\theta = \tan^{-1}(m)$. Using the trigonometric identity for the tangent of a sum of two angles,

$$(3) \tan(u + v) = \frac{\tan u + \tan v}{\tan u - \tan v},$$

I find that the ratio of adjacent block lengths and distances to those blocks is a constant related to the slope of the line defining the relationship of block length to distance from the fault,

$$(4) \frac{L_{\max 2}}{L_{\max 1}} = \frac{X_2}{X_1} = \frac{1 + m}{1 - m}.$$

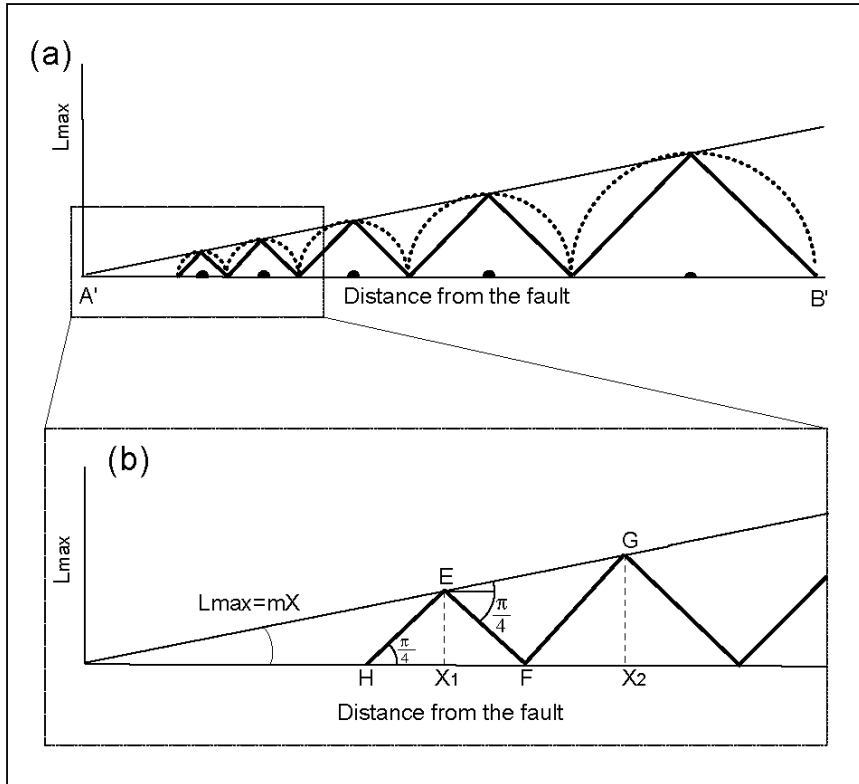


Figure 23. Geometric illustration of blocks number calculation

(a) Illustration the minimal number of blocks within OFD zone filled by circular blocks of increasing radius posted side by side. (b) Geometric relationships used for calculation of the number of large blocks in the OFD zone, n.

Multiplying the ratios for n adjacent blocks together, X_1 to X_n ,

$$(5) \frac{X_2}{X_1} \times \frac{X_3}{X_2} \times \frac{X_4}{X_3} \dots \times \frac{X_n}{X_{n-1}} = \left(\frac{1+m}{1-m} \right)^{n-1}.$$

Canceling X values that appear in both the numerator and denominator leaves

$$(6) \frac{X_n}{X_1} = \left(\frac{1+m}{1-m} \right)^{n-1},$$

And solving for n,

$$(7) n = \frac{\log(X_n / X_1)}{\log[(1+m)/(1-m)]} + 1.$$

Starting at a minimum distance, X_1 , equation 7 is used to calculate the number of blocks required out to a distance X_n . A finite minimum distance is required, otherwise an infinite number of blocks is needed. In order to get conservative estimate of n, I use a minimum distance, X_0 , of 1 m, which is the maximal width of fault gouge zone as it described by Chester et al., 2005. Thus, X_1 , the center of the closest block to the fault is

$$(8) X_1 = \frac{X_0}{1-m} = \frac{1}{1-m}.$$

Thus, n represents the number of blocks bounded between 1 m from the fault to the outer edge of the OFD zone.

For an 800 m-wide OFD zone I use a value of $m=0.71 \pm 0.05$ derived from the variance of the mylonite rotation data (Fig. 24) to find that $n=3.8 \pm 0.3$. For a 400 m-wide OFD I use $m=0.61 \pm 0.06$ to find that $n=4.2 \pm 0.3$. Essentially, I found that due to the slope difference, mylonite rotation data require the same number of blocks despite a factor of two uncertainty in the width of the OFD zone.

Having n enables estimating the ratio between the summed lengths of secondary faults within OFD zone to the length of the adjacent main fault. To do this I calculate the number of blocks of different radii, L_{\max} that can fit into a swath defined by the diameter of the largest block (Fig. 27). I set R equal to radius of largest block at the edge of the OFD zone and r represents the radius of the smaller blocks. K is the number of circles of radius r that can fit in the largest circle with radius R , and thus $R=Kr$. Because

$$(9) 2\pi R = K \times 2\pi r,$$

the cumulative circumference of circles of radius r that fit side by side into the diameter of the largest circle of radius R is simply equal to the circumference of the largest circle. Thus, within a swath defined by the diameter of the largest block (Fig. 27), the cumulative circumference of circular blocks, L_c is

$$(10) L_c = n \times 2\pi R$$

The length of the adjacent portion of the main fault is by definition $2R$ (e.g. Fig. 27). Therefore the ratio of main fault length to secondary fault length, i.e. the secondary fault density,

$$(11) \rho_f = \frac{L_c}{2R} = n\pi.$$

This relation may overestimate ρ_f because blocks could share the same bounding fault. However, smaller blocks probably fill the gaps between larger, equi-dimensional blocks and this would increase ρ_f . Hence, this is a likely a minimum estimate. Applying equation 11 for circular blocks using n and m values for 800 and 400 m wide OFD zones provides ratios of ~ 12 and ~ 15 , respectively. These estimates suggest that the cumulative length of secondary

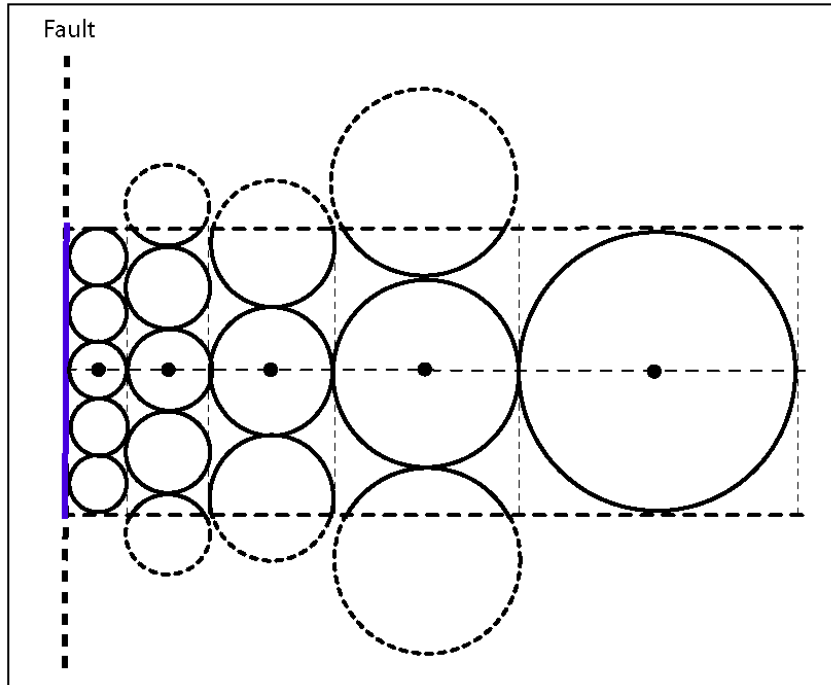


Figure 24. Geometric illustration of secondary-faults density calculation

Configuration of blocks used to calculate secondary fault density. Secondary fault length is calculated from the summed circumference of circles bounded by the swath shown with the dashed lines.

faults within the OFD zone is at least an order of magnitude greater than the length of the main fault.

4.1.4. Rotational shear displacement accommodated within the OFD zone

The magnitude of rotational displacement and its fraction of the total displacement may shed light on the uncertainty involved with slip estimates based solely on offset along faults. Distributed displacement next to the Harper Lake fault is calculated based on the azimuthal component of mylonite rotation, a component that is probably representative of vertical axis rotation. These are conservative displacement estimates based on the assumption that rotation does not exceed 90°. The minimum rotational shear displacement occurs in the southern portion of the study area where there is no significant mylonite rotation (Fig. 19) and is thus approximately zero. The maximum rotational shear displacement occurs in the northern portion of the study area where a continuous change in the azimuthal component of mylonite rotation is observed within the OFD zone (Fig. 28). In this area, systematic rotation occurs only with respect to the vertical axis (Fig. 8). Therefore, the displacement calculations based on the azimuthal component of mylonite rotation encompass the major component of rotational displacement.

I calculate rotational shear displacement by integration of the azimuthal component of rotation over the width of the OFD zone (W). W is estimated by finding the cutoff distance that divides the data set into two groups with the greatest difference of mean mylonite rotation. This is consistent with a visual inspection of the data. For the subset of data between the fault and W , I fit a linear regression to estimate the relationship between the azimuthal

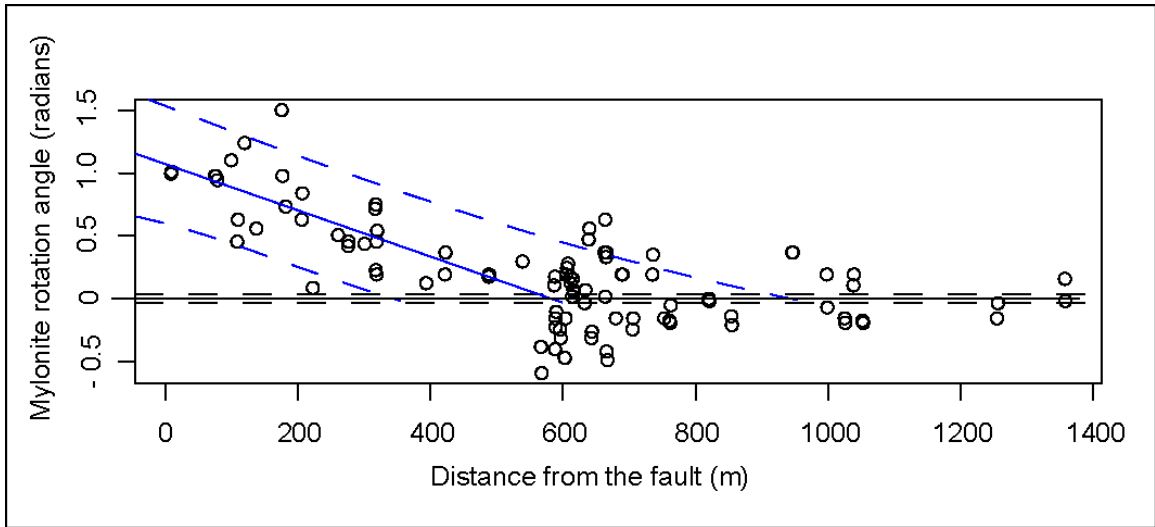


Figure 25. Mylonite rotation vs. distance from the northern section of the fault
 Azimuthal component of mylonite rotation data at the northern section of the Harper Lake fault. Negative rotation values represent either counterclockwise rotation or clockwise rotation $>90^\circ$. Blue lines show a linear regression of rotation versus distance from the fault. The dashed blue lines mark the 95% confidence belt for the regression mean. Dashed black lines mark the standard error of the mean for the rotation outside of the OFD zone. The intersection of these regression lines determines the bounds of integration of rotation to yield displacement.

component of mylonite rotation (θ) and the distance from the fault (Fig. 28). For the northern section of the data set, the regression yields $\theta = 1.05 - 0.0018x$, $R^2 = 0.52$, where θ is in radians and x is distance from the fault in meters. The significance of the slope was verified through ANOVA test for 95% confidence ($f_t = 33.21$, $f_{crit} = 4.17$). The continuous change of the azimuthal component of mylonite rotation within the OFD zone in this area suggests that rigid block dimensions are much smaller than the width deformation zone. This could justify the use of a continuum model to calculate the shear displacement (Lamb, 1987, Kimorah et al., 2004). For elongate blocks, I calculate shear displacement,

$$(12) D = \int_0^w \tan(\theta(x)) dx = \int_0^w \tan(mx) dx,$$

after Kimorah et al., (2004). This results in rotational shear displacement, D , of 400 ± 90 m. Such an elongate block configuration, however, is problematic because it creates volume problems associated with block rotation that requires internal deformation of blocks (Fig. 29). Circular blocks, on the other hand, can rotate without causing these volume and internal deformation problems, and therefore are probably a better model for areas where significant rotation is observed. For circular blocks I use;

$$(13) D = \int_0^w \frac{\theta}{2} dx = \int_0^w \frac{mx}{2} dx.$$

This results in D of only 160 ± 40 m. The factor of two difference in D calculated with these different methods is a result of the elongation of blocks that is implied by integrating over the tangent function. This results in a nonlinear increase of D with rotation angle (Fig. 29).

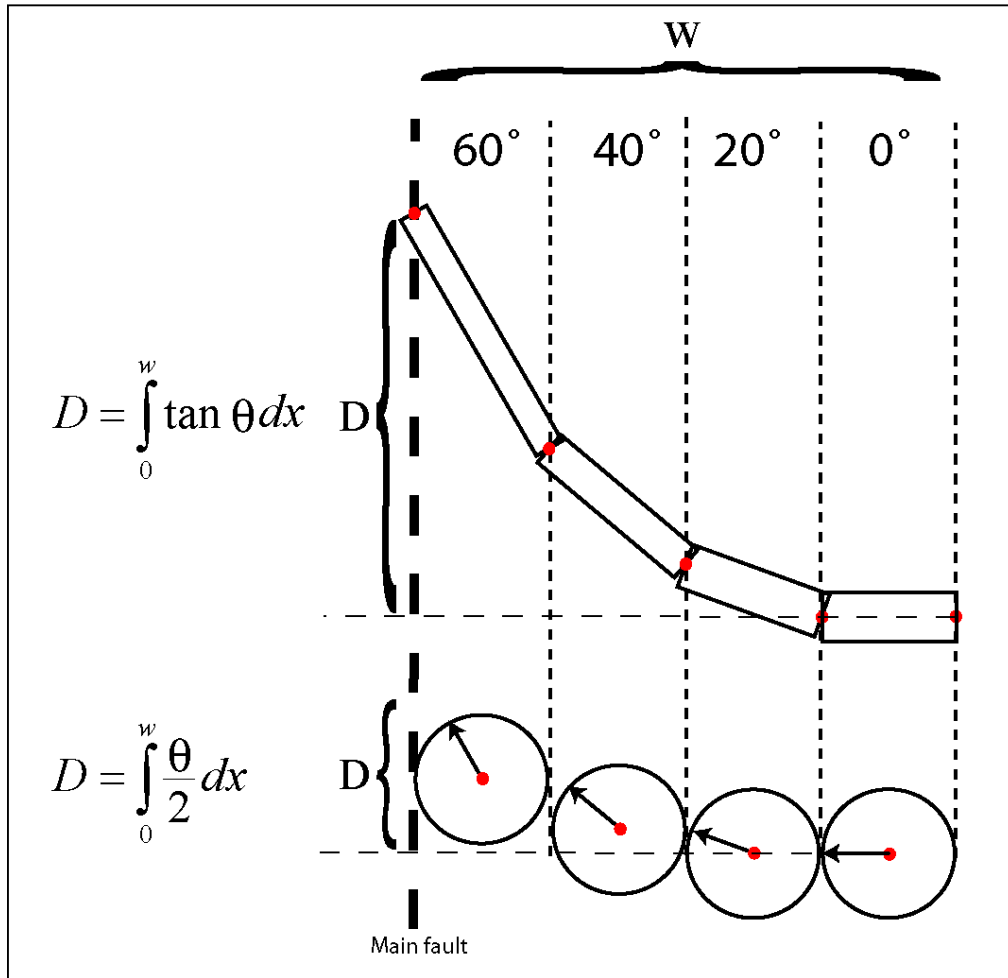


Figure 26. conceptual models for cumulative shear displacement

Conceptual illustration of two different models for calculation of shear displacement due to a linear increase in rotation angle towards a fault. The two models produce different estimates of displacement. The width of the OFD zone is a constant, W , in these models, as is the amount of rotation at a given distance from the fault. Bold black lines mark block boundaries and red circles mark rotation axes. Bold dashed lines mark major block bounding faults. Note that rectangular blocks must deform internally in order to maintain their area, thus additional internal deformation must occur. Such volume problems caused by elongate block rotation may cause strain in the third dimension, out of the figure plane. Rotation values approaching 90° yield infinite, unrealistic, displacement values for elongate blocks. Circular blocks, on the other hand, rotate without internal deformation and yield realistic displacement values for high rotation angles. Thus, the integrated displacement for circular blocks is lower than for elongate blocks. Note that the vertical distance between the centers of adjacent circular blocks equal to the arc-length defined by the block radius times the angle of rotation.

Note that the azimuthal component of mylonite rotation is calculated with respect to a far-field angle that has an error associated with it. This error is incorporated into estimates of D (Fig. 28). The combined error is estimated by Monte-Carlo simulation of 1000 repetition sampling from the distribution of far field angle (0 ± 0.03 radians) and from the distribution of regression slopes deduced from the OFD zone data-set (-0.0018 ± 0.0003).

It is important to note that the distributed deformation measured here is only on one side of the fault. If distributed displacement is symmetric across faults, then these displacement values, measured east of the fault, are only half of the total distributed displacement. A symmetric distribution of OFD is supported by the observation of a symmetric pattern of mylonite rotation surrounding secondary fault A (Fig. 9, 10) as well as the symmetric deflection of the Silver Bell fault across the Calico fault (Oskin et al., 2007; Fig. 4).

4.2. Analysis of seismic refraction data to trace changing rock properties within OFD zones

I analyzed seismic refraction data in order to quantify the change in rock properties away from the Calico fault and to compare these properties with the distribution of displacement in the OFD zone. First, I present reasoning for the assumptions that underlie the analysis. Second, I present a model to express t , the first arrival time, as a function of x , the distance between a geophone and a shot point, for a rock mass where seismic velocity varies linearly with distance and depth. Third, I apply this model to find the combination of parameters that provides the best fit to the seismic refraction data. Fourth, I compare the different refraction lines and analyze the results in terms of OFD.

Typically, the analysis of refraction lines to interpret subsurface velocity structure is based on kinks in an arrival time versus distance graph. These kinks are interpreted to indicate contacts between layers of different seismic velocities. However, the observations presented in Figure 17 display approximately smooth curvature, and thus suggest a continuous increase of seismic velocity with depth, and, possibly, with distance from the fault. Therefore, the refraction data is analyzed assuming that seismic velocities change continuously as function of distance from the fault and of depth. This assumption is supported by the lack of discrete layering in the granite exposed in the study area. Increasing seismic velocity with depth probably occurs due to overburden pressure and due to weathering near the surface. Increase of seismic velocity away from the fault may be due to a decrease in crack density - a measure of damage (Li and Vidale, 2001; Vermilye and Scholz, 1998; Faulkner et al., 2006). To simplify the calculations, I assume that velocity varies linearly. Although the seismic velocity function is certain to be nonlinear, for the scale of this study I can assume linearity for each refraction line (110-230 m long). I assess the spatial nonlinearity at a 1000 m-scale by comparing between the different refraction lines.

Each refraction line is assumed to reflect a 2-D velocity structure,

$$(14) v = f(x, z) = v_0 + az + bx,$$

where v_0 is the surface seismic velocity at the shot point, z is depth, x is horizontal distance from the shot point, and a and b are coefficients. Because the refraction lines are at high angle to the fault (fig 16), x also represents proximal horizontal distance from the fault. Thus, the ratio $b:a$ is approximately indicative of the effect of the fault on the velocity structure (Fig. 30). This can be expressed as:

$$(15) \alpha = \tan^{-1}\left(\frac{b}{a}\right),$$

Where high α value indicates significant affect of the fault on the velocity structure. α is also used to rotate the Cartesian reference frame of the velocity structure so that,

$$(16) v = f(z') = v_0 + a'z',$$

where z' is the apparent depth below a plane of constant velocity which is rotated at angle α relative to the ground surface (Fig. 30). a' is a corresponding coefficient that is geometrically related to a and b by α ,

$$(17)$$

$$a = a' \cos \alpha ,$$

$$b = a' \sin \alpha .$$

Hence, by finding v_0 , a' , and α for each refraction line, I can interpret the velocity structure and examine how it is affected by the fault. I can also compare b and v_0 values between different refraction lines to get a larger sense of the change in seismic velocity as function of distance from the fault.

Sheriff and Gerldart (1995) show that a linear increase of seismic velocity with depth of the form of eq. (16) results in a circular ray-path. They also show that the center of the circular ray-path lies above the surface at a distance h , where:

$$(18) h = \frac{v_0}{a} .$$

The time it takes for a wave front to get from depth $z=0$ to $z=z_j$ is:

$$(19) t = \frac{1}{a} \ln \left(\frac{\tan(j/2)}{\tan(i/2)} \right) ,$$

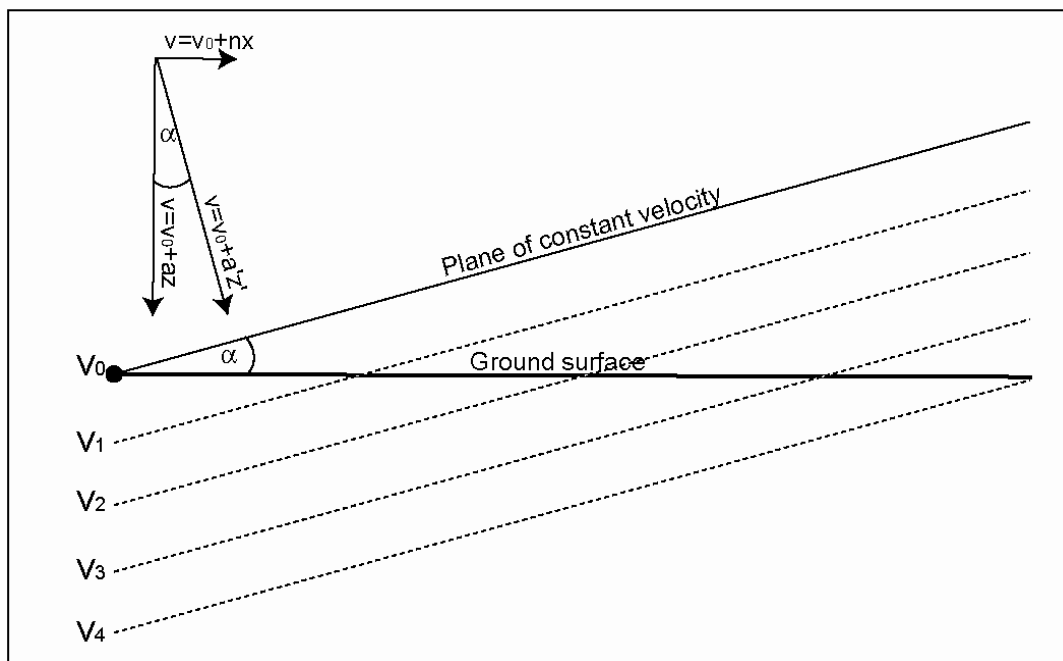


Figure 30. Illustration of tilted velocity structure

Relationship of planes of constant velocity to the ground surface for seismic velocity that varies linearly with both depth and horizontal distance.

where j is the angle between the normal to the surface and the ray-path, and i is the angle between the normal to the surface and the initial ray-path at the shot-point (Fig. 31). Figure 32 shows forward and reverse ray-paths for equidistant shot-point-geophone pairs where α is non-zero. For this general case, I must define both forward and reverse value of i and j , i_f, j_f, i_r, j_r . The travel time equation (equation 19) then becomes,

(20)

$$t_f = \frac{1}{a} \ln \left(\frac{\tan(j_f / 2)}{\tan(i_f / 2)} \right),$$

$$t_r = \frac{1}{a} \ln \left(\frac{\tan(j_r / 2)}{\tan(i_r / 2)} \right).$$

Based on the derivation presented in appendix 2,

(21)

$$i_f = \sin^{-1} \left[\frac{1}{r_f} \left(\frac{v_{x0}}{a'} - (L - x/2) \sin \alpha - x/2 \times \sin \alpha \right) \right],$$

$$j_f = \sin^{-1} \left[\frac{1}{r_f} \left(\frac{v_{x0}}{a'} - (L - x/2) \sin \alpha + x/2 \times \sin \alpha \right) \right],$$

$$i_r = \sin^{-1} \left[\frac{1}{r_r} \left(\frac{v_{x0}}{a'} + (L - x/2) \sin \alpha - x/2 \times \sin \alpha \right) \right],$$

$$j_r = \sin^{-1} \left[\frac{1}{r_r} \left(\frac{v_{x0}}{a'} + (L - x/2) \sin \alpha + x/2 \times \sin \alpha \right) \right],$$

where the coefficients r_f and r_r are the radii of the forward and reverse ray-paths,

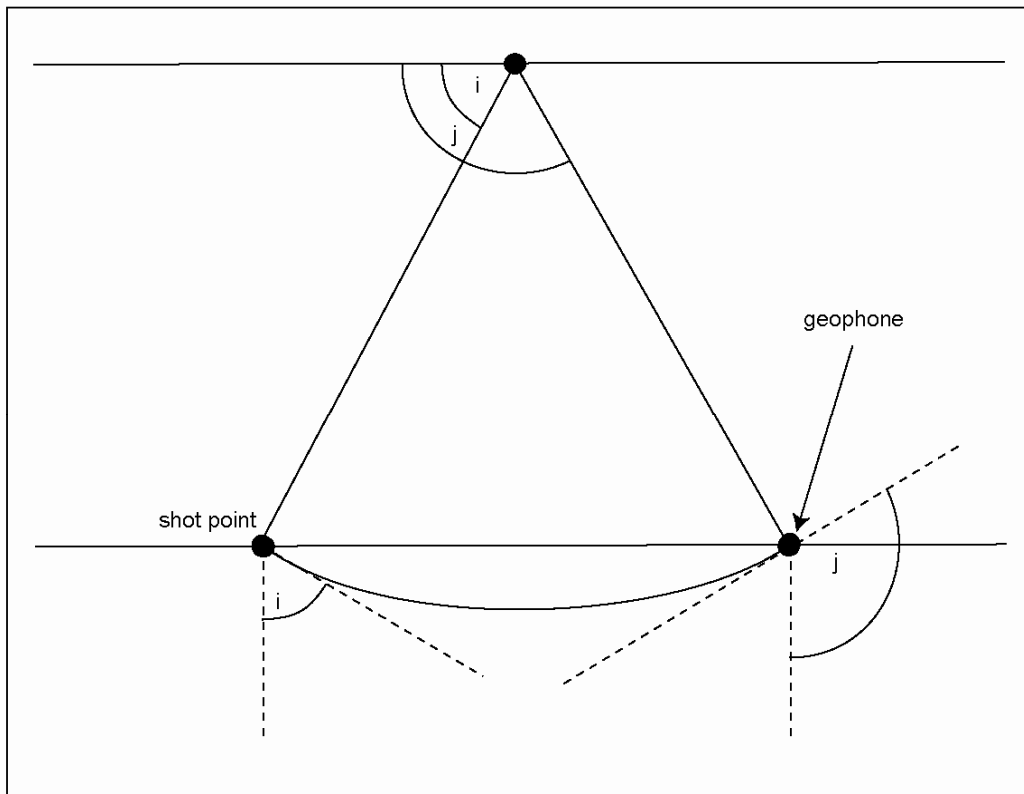


Figure 31. Illustration of circular ray-path

i and j angles for a circular refraction ray-path through a linear seismic velocity gradient. j is the angle between the normal to the surface and the ray-path. i is the angle between the normal to the surface and the initial ray-path at the shot-point.

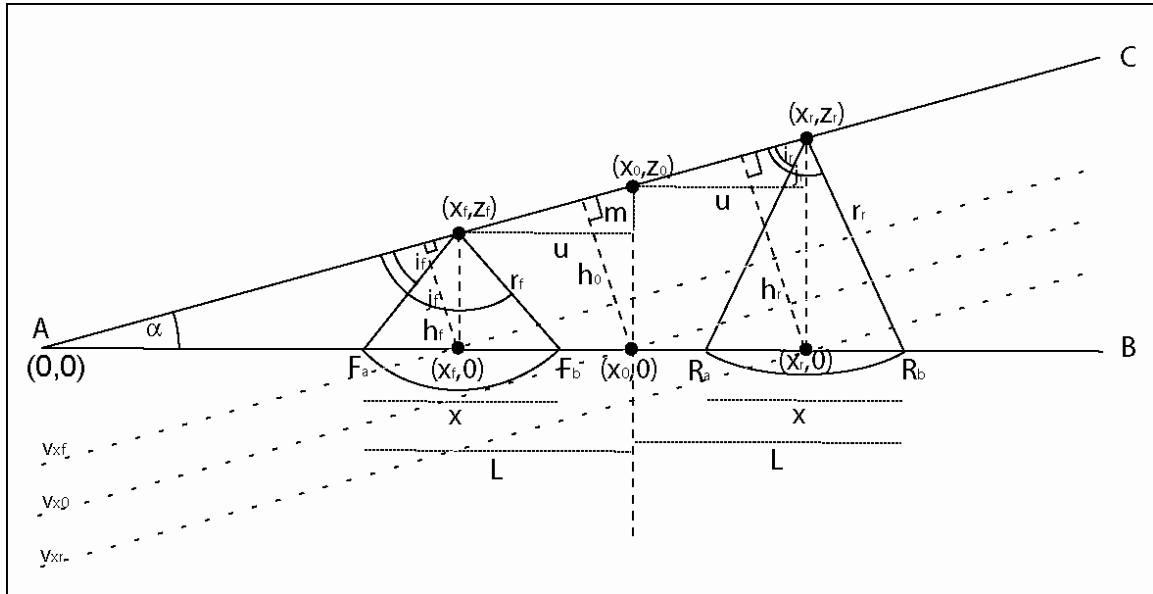


Figure 32. Geometric illustration for seismic refraction model

Geometry of a single pair of refraction line ray paths where seismic velocity varies both with horizontal distance and with depth. α is the angle of rotation, line AB is the surface and line AC is the line where $v=0$. The dotted diagonal lines crossing at $(x_f, 0)$, $(x_0, 0)$, $(x_r, 0)$ are velocity contours of v_{xf} , v_{x0} , and v_{xr} respectively. F_a and R_b are shot points located a distance of $2L$ apart. F_b and R_a are geophone locations and the arcs $F_a F_b$ and $R_a R_b$ are the ray paths between each shot-point and a geophone located at distance x from it. x_f and x_r are locations midway between the shot-point and the geophone. x_0 is located at the middle of the refraction line at distance u from x_f and x_r . h_f, h_0 and h_r are the distances from a line where velocity is equal to zero to the ground surface at points $(x_f, 0)$, $(x_0, 0)$ and $(x_r, 0)$. r_f and r_r are the radii of the corresponding ray paths. i_f, j_f and i_r, j_r are the corresponding ray path angles as presented in Figure 31.

(22)

$$r_f = \sqrt{\left(\frac{x}{2}\right)^2 + \left(\frac{v_{x0}}{a' \cos \alpha} - (L - x/2) \tan \alpha\right)^2},$$

$$r_r = \sqrt{\left(\frac{x}{2}\right)^2 + \left(\frac{v_{x0}}{a' \cos \alpha} + (L - x/2) \tan \alpha\right)^2},$$

L is the half-length of the refraction line.

Searching through possible combinations of parameters a' , α and v_{x0} , I found the combination that provides the best fit for each refraction line. I tested velocity gradient a' , between 0.002 and 0.070 s^{-1} at 0.002 s^{-1} intervals. Fifty possible v_{x0} values between 1 to 2 m/s were tested. I investigated a wide range of α values between -80° to $+80^\circ$ at 0.2° increments. Thus, in all I tested $\sim 1.4 \times 10^6$ possible combinations of parameters. I evaluate the goodness of fit from the RMS of time residuals between the model and the data. Figure 33 presents the model for each line based on its best fit parameter combination and Figure 34 shows the corresponding best fit parameter combinations. I show relative errors for each parameter a' , α and v_{x0} , where the RMS value is 1ms greater than the best-fit combination.

The best-fit parameter combinations for the different refraction lines can be projected onto a vertical plane oriented perpendicular to the fault. The projection is done assuming that the actual velocity structure is tilted about horizontal axis parallel to the fault. Comparisons, of the projected results for the different refraction lines suggest a nonlinear increase of velocity (and thus decrease of damage) away from the Calico fault (Fig. 35). The best fit parameter combinations (Fig. 34) for both far and close shot point pairs indicate that α is significantly different from zero for the first line (31.8° for close shot-points, 10.8° for far shot-points). The difference in this angle between far and close shot-point pairs probably

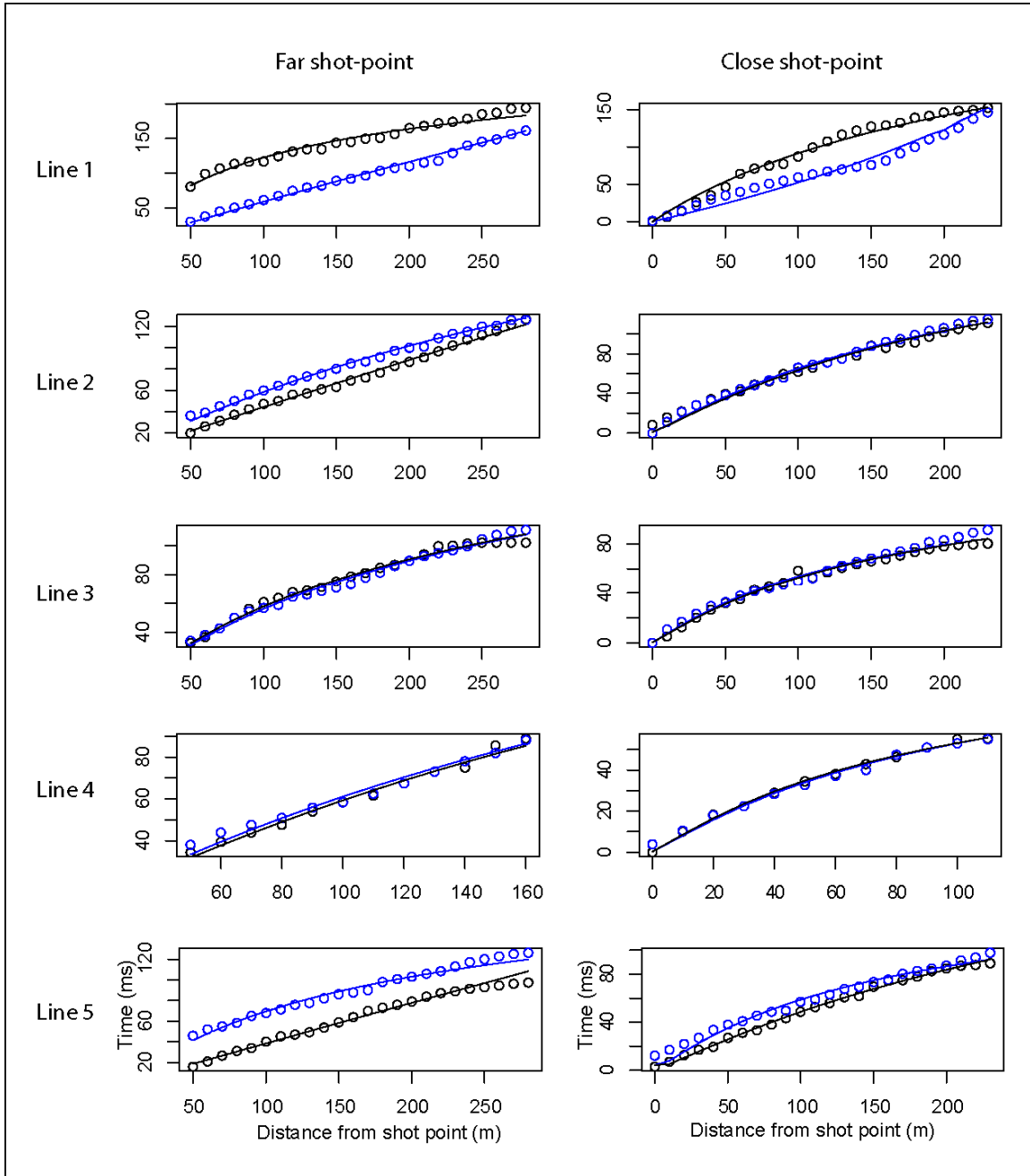


Figure 33. Model fits for all refraction lines

Model fits for all refraction lines based on the best fit parameter combinations. Blue and black circles are arrival times for the forward (shot point closer to the Calico fault) and reversed (shot point farther from the Calico fault) lines. Blue and black lines are the corresponding model fits. Note that the time axis scale varies from line to line. The significant difference of forward and reverse arrival times for the close shot-point line 1 indicates a substantial horizontal velocity gradient.

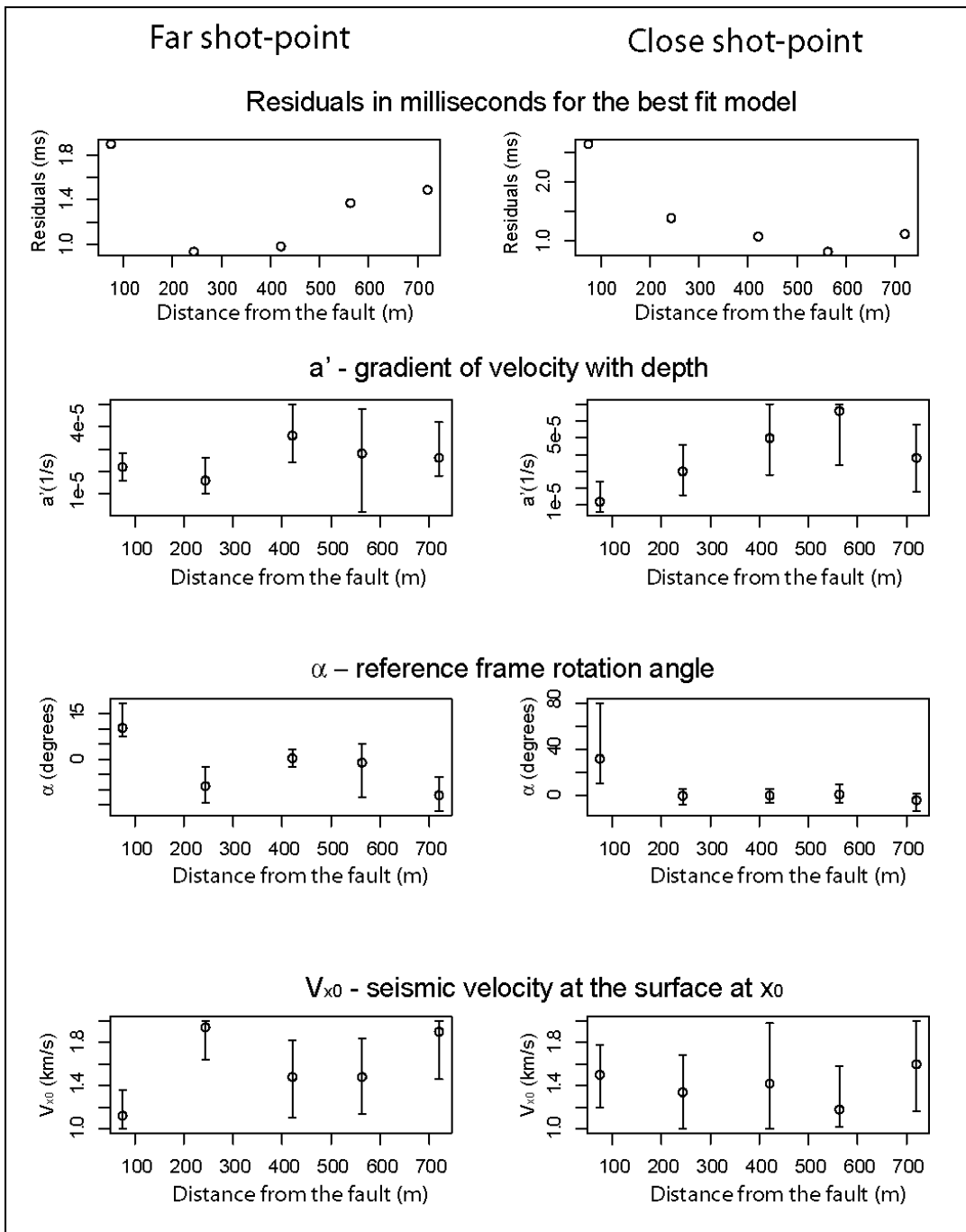


Figure 34. Best fit parameter results for all refraction lines

Best fit parameter results for all refraction lines, plotted as a function of distance from the Calico fault. Values are plotted at the center-point of each refraction line. Line 1 is the closest to the fault. Error bars represent relative errors calculated by the range of parameters that fit within 1 ms of RMS residual of the best fit.

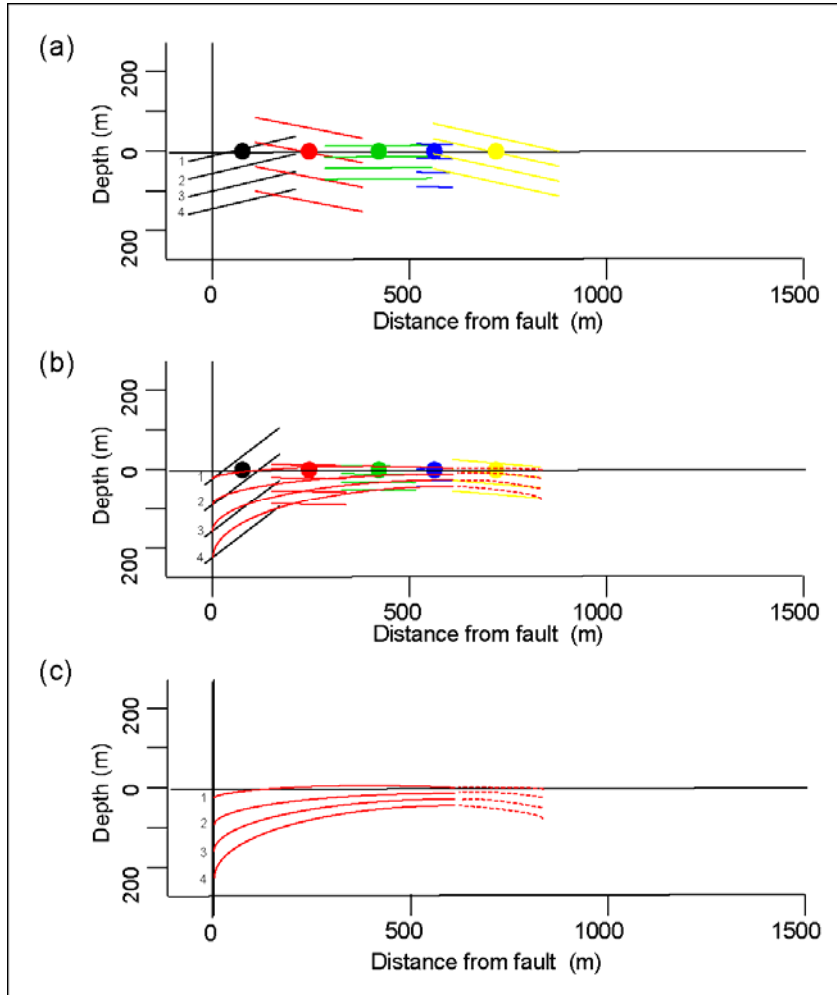


Figure 35. Modeled velocity structure

(a) Cross-section of seismic velocity contours, based on the best fit results of a continuous linear model for the far shot points. Contours are projected onto vertical plane oriented perpendicular to the fault. The projection is done assuming that the actual velocity structure is tilted about horizontal axis parallel to the fault. Different colors represent different refraction lines. Colored circles are located at the center of each line and correspond to x_0 in the velocity model (Fig. 32). Colored lines are seismic velocity contours and the associated numbers represent velocity in km/s. The velocity at the surface is defined by v_{x_0} , the angle of the velocity contours is determined by α , and the spacing between the contours is defined by a' . (b) Similar cross-section as in a, but for the close shot-points. (c) Interpretative contours of the seismic velocities presented in (b). Contours curve toward the Calico fault due to presence of a damage zone. Contours for line five (dashed), located furthest from the fault, also curve downward. This is either an artifact due to thicker alluvial cover or due to approach of the Silver Bell fault (Fig. 16). See text for discussion. Note that the uppermost contour lies mostly above the ground surface.

arises due to placement of one of the far shot-points west of the Calico fault where there is more alluvial cover. The slightly negative α values for Line 5, ~600-800 m from the fault, are probably also related to a northeastward thickening wedge of alluvial cover in Silver Canyon wash. However, in this area the seismic velocity may also decrease approaching the Silver Bell fault (Fig. 4, Fig. 16). v_{x0} values are nearly constant for all lines. This indicates that surface velocity is relatively unaffected by distance from the fault.

Velocity gradient, a' increases with distance from the fault. Far from the fault, where a' values are high and α is small, a' is probably dominated by the weathering front. This would explain why seismic velocity increases so rapidly with depth. Next to the fault, however, where α is relatively large, a' is probably also affected by the fault damage zone. This reduces the gradient of seismic velocity with depth. However, it is important to note that due to the short length of the seismic lines, the reported a' values only hold for the uppermost tens of meters. Otherwise, the reported a' values would result in extremely high seismic velocities in very shallow depths. This is further supported by the consistently lower a' values determined from far shot-point pairs that sample deeper than the close shot-point pairs (Figs. 34, 35).

4.3. InSAR data analysis to trace the effect of lithology on rigidity.

I analyzed the high-pass filtered InSAR data from 7 NW-striking faults spanning the central Mojave Desert (Fialko et al., 2002) to test for the effect of lithology on rigidity reduction. First, I divided each fault into segments. These segments are arranged symmetrically about a line striking SW from the Hector Mine epicenter, and segmented

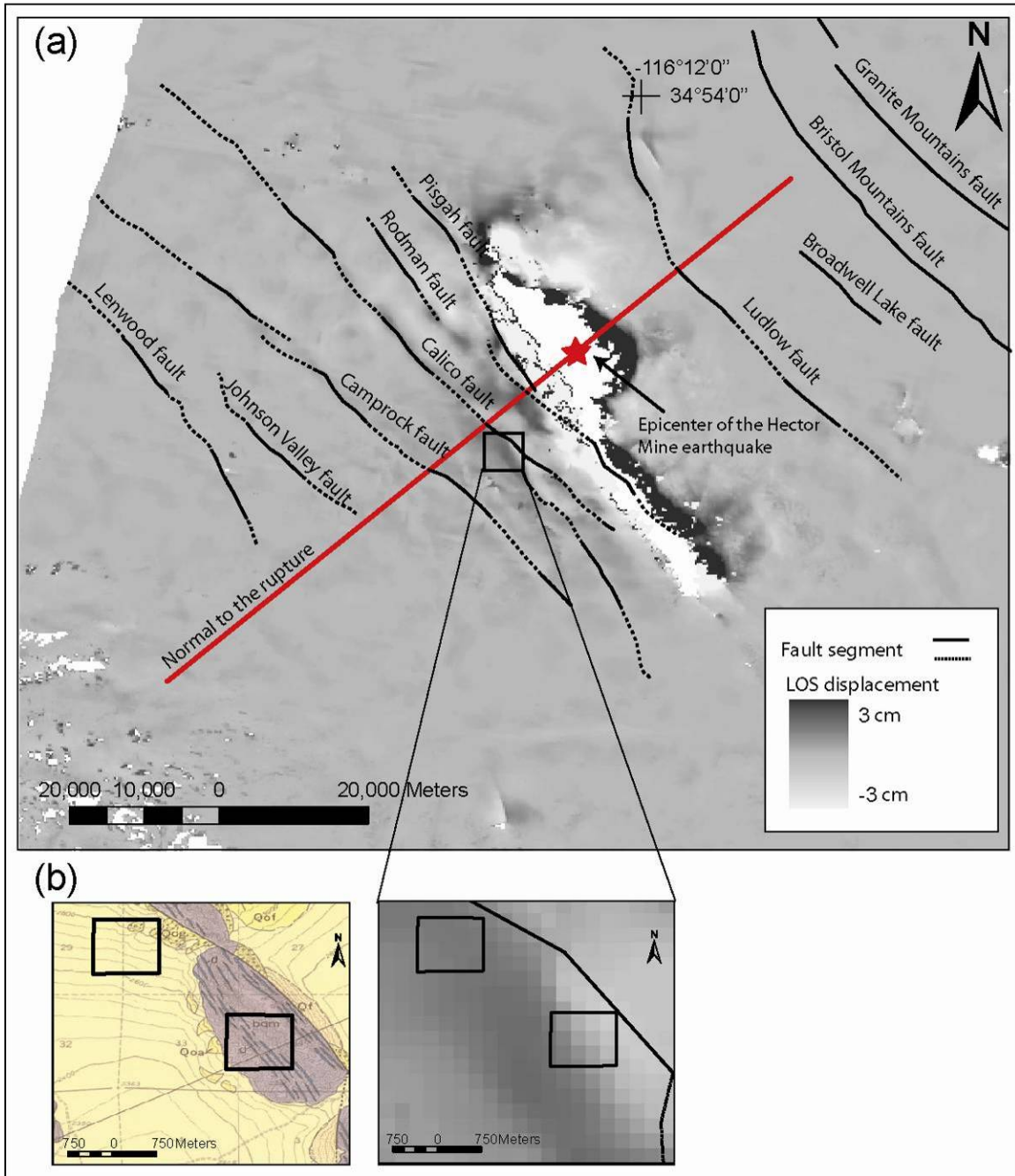


Figure 27. Illustration of InSAR data analysis

Faults are divided into segments, based on their distance from the SW striking line that bisects the epicenter normal to the fault trace. Rectangles represent the sampling window and are located within 2 km of the fault. Note the lack of displacement next to Broadwell Lake, Bristol Mountains, and Granite Mountains faults at the north east part of the map, these faults, also considered inactive geologically, were not included in the analysis.

by 10 km distance from the SW striking line (Fig. 36). Fault segments are arranged this way because coseismic stress drop decreases with distance from the epicenter (Stein and Wysession, 2003), and because the sign of this stress changes about this SW-striking line. Second, I used a 0.8 km² sampling window to calculate mean displacement and displacement gradient values for crystalline and sedimentary rocks within a 2 km wide buffer zone around each segment (Fig. 36). 2 km is approximately the width of the band of low rigidity surrounding these faults (Fialko et al 2002, 2004). The pair of means, each associated with one of the two different lithologies, are used to create a dataset composed of 20 pairs, a pair for each fault segment. The paired dataset enables comparison of lithologies only within each segment to minimize the bias caused by spatial differences in the stress drop. The consistency of the means differences is then quantified by employing Wilcoxon Signed-Ranks test ($H_0: \mu=0$). The null assumption is that the means are equal within each segment. The test results for both displacement and displacement gradient failed to reject the null assumption for 90% confidence. Thus, I conclude that within the resolution of the InSAR data (~200×200 m pixel), there is a low probability of having significantly different coseismic displacement patterns for crystalline and sedimentary rocks. This result implies that the compliant zones imaged by Fialko et al (2002) do not differ between sedimentary and crystalline rocks.

5. Discussion

In this section, I synthesize my observations to develop an understanding of OFD zones and their significance. First, I review the assumptions underlying my interpretation of distributed displacement. Then, I discuss the character of OFD zones, including the magnitude of distributed displacement, the width of OFD zones, and the distribution of displacement within these zones. Finally, I discuss structural aspects of the OFD zone – its level of activity, the structural mechanisms of strain accommodation, and the possible interactions between damage and distributed displacement.

5.1. Assumptions

The assumption of original linearity of OFD markers is fundamental to the displacement and block size calculations. This assumption is supported by the clear association of deflected mylonitic lineation directions with the Harper Lake fault (Fig. 7) and the deflection of the Silver Bell fault within 500 m from the Calico fault (Oskin et al., 2007, Fig. 4). At a smaller scale, a secondary fault next to the Harper Lake fault (fault A in Fig. 6) also shows deflected mylonitic lineation directions associated with it (Fig. 9). Though deflection could arise for features emplaced next to existing faults due to distorted stress field next to the fault (Zoback et al., 1987), this is not the case for the mylonitic lineation and the Silver Bell fault because these markers predate initiation of faulting along the Harper Lake and Calico faults (Bartley et al., 1990; Glazner et al., 2000).

To evaluate the contribution of distributed displacement to total displacement across fault zones I assume that distributed displacement is symmetric across faults. The example of the secondary fault next to the Harper Lake fault (fault A in Fig. 6, Fig. 9) as well as the symmetry of the Silver Bell fault (Oskin et al., 2007, Fig. 4) across the Calico fault also supports this assumption.

In the analysis of mylonitic lineation directions, I assumed that the rotation angle is the smallest angle between lineation directions. It is important to note that unlike paleomagnetic measurements, the measurements of mylonitic lineation provided only orientation. Rotations larger than 90° cannot be confidently resolved without measurements of mylonitic kinematic indicators.

The assumption of equi-dimensional/circular blocks is fundamental to the calculation of the ratio between the length of secondary faults and the length of the main fault. Equi-dimensional blocks minimize volume problems and internal deformation caused by rotation of elongate blocks. Thus, equi-dimensional blocks are probably common in areas of significant rotation.

5.2. Magnitude of Distributed Displacement

To generalize my observations to other faults, the relative magnitude of distributed displacement for the Harper Lake fault and Calico fault is estimated by dividing the magnitude of distributed displacement by the total displacement across the each fault. Total displacement is estimated from markers projected to each fault from outside of the OFD zone. For the Calico fault, 2.2km of distributed displacement divided by 9.8km of total displacement (Oskin et al., 2007), results in relative magnitude of 23%. For the Harper Lake

fault, distributed displacement is estimated by summing the components of vertical axis rotation and secondary fault slip in a portion of the study area. Here, 180 ± 10 m of displacement occurs across a secondary fault (fault B in Fig. 6), and 160 ± 40 m of displacement occurs via vertical axis rotation calculated through the circular block model. The elongate block model provide 400 ± 90 m of displacement. Summing the rotational and fault slip components, and multiplying it by 2 due to symmetry, results in 680 ± 100 or 1160 ± 200 m of distributed displacement, depending on the model of block rotation used. This sum is a lower bound due to possible unrecognized displacement along other secondary faults. Dividing the calculated distributed displacement values by 3500 ± 500 m of total displacement across the Harper lake fault (Bartley et al., 1992; Fletcher, personal communication with Oskin), results in relative magnitude of 19 ± 3 % and 33 ± 5 %. The relatively large values of distributed displacement next to these two faults agree with previous studies (Kimorah et al., 2004; Nelson and Jones, 1987; Miller and Yount, 2002) that show that the magnitude of distributed displacement may be up to one half of the total displacement. These results strongly suggest that displacement estimates that do not account for distributed displacement may be significantly underestimated.

The alternating pattern of mylonite rotation along the Harper Lake fault (Fig.18) suggests that the magnitude of distributed displacement changes significantly along fault strike. These variations may also be due to trade-off between different mechanisms of distributed displacement. For example, block rotation may trade off with offset along sub-parallel secondary faults. Along-strike variation in the magnitude or mechanism of distributed displacement may also explain the insignificant rotation measured paleomagnetically. The

puzzling lack of significant rotation in almost all of the paleomagnetic sites is further discussed in section 5.6.

5.3. OFD zone width

Most of my observations support the idea that distributed deformation commonly occurs within 1km from faults (Fig. 4, 7). However, this is only a general estimate. The outer boundary of the OFD zone may vary and is often not well defined because of a gradual decrease in the amount of deformation. For example, segmentation of dikes next to the Calico fault suggests that the OFD zone could extend outward for up to two kilometers (Fig. 5). The width of the OFD zone may also change along fault strike (Fig. 19). Measurements of distributed deformation next to the Calico and Harper Lake faults indicate that distributed displacement extends for up to ~800 m from the main fault trace. Secondary faults also extend up to 400 m away from the Pisgah fault. Secondary faults next to the Harper lake fault have their own OFD zones that are proportionally narrower (Fig. 9, 10).

Similar widths of the OFD zone were found in studies of surface deformation from the Landers and Hector Mine earthquakes. These studies show that inelastic deformation often occurs within 50-200 m from the main fault trace, and may extend for up to 1700 m from the main fault trace (Johnson et al., 1994; Michel and Avouac, 2006; McGill and Rubin, 1999; Trieman et al., 2002). These authors also suggest that the width of the OFD zone may depend on lithology and structural complexity of the fault trace.

5.4. Distribution of shear displacement within the OFD zone

Overall, observations from the Mojave Desert suggest that distributed displacement increases nonlinearly with distance toward the main fault (Figs. 4, 6, 7, and 10). In section

4.1.2, I fit a linear function to the azimuthal component of mylonite rotation next to the northern portion of the Harper lake study area. Integration of this yields a squared dependence of displacement on distance. An exponential function represents displacement approaching faults almost as well. The intensity of OFD, as represented by the variability of mylonite rotation, also increases nonlinearly towards faults (Fig. 17). Studies by Kimorah et al., (2004) and Katz et al., (2003), using paleomagnetic data, also report a pattern of nonlinear increase in vertical axis rotation towards strike slip faults in Japan and Israel. Taken together, these observations suggest that the nonlinear distribution of displacement within OFD zones is a general pattern that is not unique to the Mojave Desert area.

The nonlinear or exponential displacement pattern is also reflected in coseismic patterns of OFD. Studies of coseismic surface deformation, in the Mojave Desert (Michel and Avouac, 2006) and elsewhere (Lawson et al., 1908 as cited in Thatcher and Lisowski 1987), show an approximately exponential increase in faulting, fracturing, and displacement with distance toward the main fault.

5.5. Activity of OFD

A number of observations support that OFD accumulates progressively next to active faults. First, coseismic surface deformation in the Mojave Desert (Johnson et al., 1994; Michel and Avouac, 2006; McGill and Rubin, 1999; Trieman et al., 2002) and elsewhere (Lawson et al., 1908 as cited in Thatcher and Lisowski 1987; Rockwell et al., 2002; Rymer et al., 2004) shows a wide zone of inelastic deformation, including small-scale block rotation and secondary faulting. A few of these studies quantify the amount of distributed shear displacement (Lawson et al., 1908 as cited in Thatcher and Lisowski 1987; Rockwell et al.,

2002). Second, in few cases I observe distributed displacement of markers that post date fault inception (Fig. 13, 15). The Pisgah fault shows a wide zone of secondary faulting in the younger Sunshine Peak lava flow. This faulting post dates at least 600 m of displacement recorded in the older, adjacent Lavic Lake lava flow. Thus, activity on these secondary faults coexisted with slip on a well-defined, active, master fault. Next to the Harper Lake fault, a secondary fault with 179 ± 6 m of slip (fault B in Fig. 6), cuts young alluvial deposits. Strane (2007) also showed secondary faults cutting quaternary deposits up to 2 km away from the Lenwood fault.

Interestingly, the InSAR results of Fialko et al., (2002) do not show compliant zones next to major inactive faults of the Mojave Desert (Fig. 36): the Bristol and Granite Mountains, the Broadwell Lake, and the Silver Bell faults (Dokka and Travis, 1990b; Glazner et al., 2000). This may indicate that compliant zones are maintained by active faulting. Healing processes would cause compliant zones to regain rigidity once faults cease to be active.

5.6. Structural mechanism of strain accommodation within OFD zones

Figure 37 shows a conceptual model for structure of distributed displacement in OFD zones. Accommodation of distributed displacement occurs by a combination of block rotation and displacement along secondary faults sub-parallel to the main fault. The proportion between these two displacement components may vary considerably along fault strike. The density of faults, as well as the amount of rotation, increases toward the main

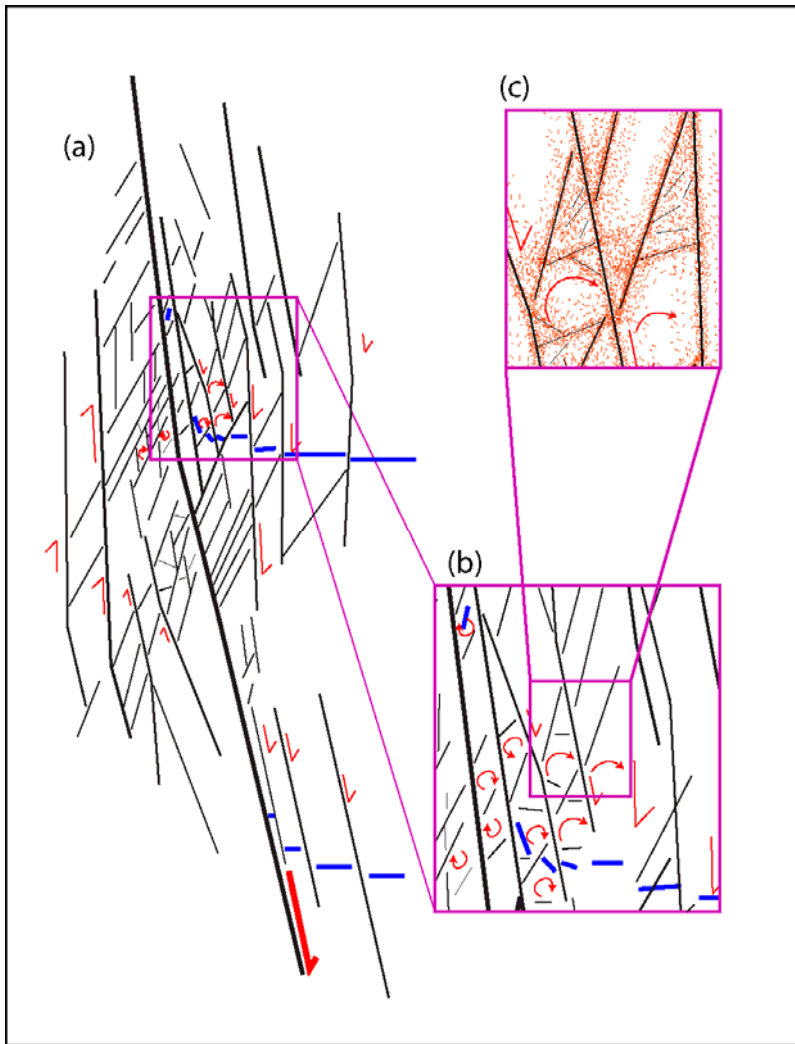


Figure 28. Conceptual model for the mechanisms of distributed displacement
 Map view of conceptual model for the mechanisms of distributed displacement in OFD zones. Black solid lines represent faults, blue lines represent planar markers, and thin orange line segments represent damage. (a) Distributed displacement is accommodated through combination of block rotation and displacement along secondary faults sub-parallel to the main fault. The proportion between these two displacement components, as well as the magnitude of displacement may vary considerably along fault strike. This variability is illustrated by the planar markers. The density of faults, as well as the amount of rotation, increases toward the main fault. (b) The dimensions of blocks decrease toward the fault and in areas of significant rotation blocks are probably equidimensional (also illustrated in c). Note that some of the blocks may rotate CCW. (c) Damage is probably distributed throughout the OFD zone via the network of secondary faults.

fault. This leads to a decrease in block dimensions, and very likely an increase in aggregate secondary fault slip, toward the main fault. In areas of significant rotation, blocks are probably equidimensional.

The lack of significant rotation from the paleomagnetic measurements is puzzling. Perhaps the sites measured just happened to randomly lie within areas where rotation did not occur. More likely, some aspect that governed site selection biased the results. One possible explanation for the lack of rotation is that rotational OFD around a vertical axis is associated with folding adjacent to faults. Except for the one potentially rotated site, bfd06, sites with folding adjacent to the main fault were avoided for paleomagnetic sampling. Conversely, the study areas along the Calico fault and Harper Lake fault, where significant rotational OFD occurs, are located within zones of modest folding. Folding and rotation may be associated due to the volume problem caused by rotation of non-circular blocks. Alternatively, higher normal stresses in areas of folding may favor rotation over simple shear.

Where measurable, integrated strain in OFD zones is dominated by normal drag. For the dextral faults studied here, normal drag is expressed as clockwise rotation of deflected markers. Though less significant, reverse drag may also be present. For example, some mylonite rotation was found to be counterclockwise (Fig. 7). This rotation may be associated with steep local slip gradient along fault strike or may occur due to local interactions between rotated blocks. Alternating modes of normal and reverse drag along fault strike are reported in studies of coseismic distributed displacement next to strike slip faults (Lawson, 1908, as cited by Thatcher and Lisowski, 1987; Rockwell et al., 2002).

5.7. Damage and displacement interactions within OFD zones

Multidisciplinary observations show correlation between the reduction of rigidity and the distribution of displacement within OFD zones. The width of distributed displacement zones (1 to 2 km half width, or 2 to 4 km total) is similar to the width of compliant fault zones imaged with InSAR (~2km, Fialko et al., 2002, 2004). These widths are also similar to the ~1km-zone of fault-parallel seismic anisotropy documented along the Hector Mine rupture by Cochran et al., (2003).

OFD zones are also characterized by a core of more intense deformation (e.g. Rockwell and Ben Zion, 2007; Faulkner et al., 2006). For example, 100-200 m wide zones of intense distributed displacement are observed next to both the Calico and Harper Lake faults. Studies of coseismic surface deformation also document a 100-400 m zone of more intense distributed deformation (Johnson et al., 1994; Michel and Avouac, 2006; McGill and Rubin, 1999; Trieman et al., 2002). The nonlinear increase in distributed displacement towards the fault is further corroborated with geophysical observations. Studies of P- and S-wave velocities show a low velocity zone of 75-250 m width along faults (Li et al., 1998, 2003; Li and Vidale, 2001). The seismic refraction study conducted next to the Calico fault shows significantly tilted velocity structure only within the first ~200 m (Fig. 35), indicating lower seismic velocity in proximity to the fault. This ~200 m wide zone is similar to the zone of intense distributed displacement indicated by the deflection of the Kane Spring fault in the same area (fig 4, 16, 35). This similarity supports the correlation in the distribution of damage and displacement within OFD zones.

The width of OFD zones may be controlled by processes of rupture propagation. Scholz et al., (1993) combined the elastic solution for fault tip stress field (Lawn and Wilshaw,

1975) with an experimental dilatancy-stress function (Scholz, 1968) to calculate crack density away from fault tip. Their model predicts an exponential decay of microfracture density away from fault tip. They also show that the width of the damage zone is 1% to 10% of overall fault length at the time of fault tip propagation past the point of observation. Yet, the spatial distribution of damage perpendicular to a point along fault strike cannot be directly predicted by this model because OFD zones are the result of multiple events of rupture tip propagation in individual earthquakes. The length of a rupture at the time of propagation beyond a specific point is unknown and likely to vary from earthquake to earthquake. However, Vermilye and Scholz (1998) show that field measurements of macro and micro structures indicate that the width of the damage zone is ~1% of the distance from furthest the fault tip, consistent with the theoretically expected damage zone width. There is similar agreement between the width of distributed displacement zones and the maximum length of faults at the points of measurement along the Harper Lake fault and the Calico fault (2-3%).

Although there is a good agreement between the width and distribution of displacement in OFD zones with the width and distribution of observed fault-compliant zones, these cannot be directly related through the model of Scholz et al., (1993). This is because their model considers dilatant cracking and not distributed shear displacement. Yet, the good empirical agreement suggests the existence of a mechanism that links the distribution of damage to distributed displacement. Such mechanism could include the formation and lengthening of secondary faults via mode two fractures within the OFD zone. Formation and growth of secondary faults, in turn, would further distribute damage through the OFD zone (Fig. 37).

Additional damage may occur by fracturing of rotated block margins due to elevated stress loads during rotation.

6. Conclusions

I show that OFD zones adjacent to 10-100 km-long, active strike slip fault in the central Mojave Desert account for a significant proportion of both active and total shear displacement. Conservative estimates show that the magnitude of distributed displacement may account for $19 \pm 3\%$ of the total displacement across fault zones. This occurs over zones that are typically 1 to 2 km across, but may in some cases be up to 4 km wide. I find that both the magnitude and the width of OFD zones can change significantly along fault strike. Within the OFD zones, displacement increases nonlinearly toward the master fault, and occurs mostly within the first 100-200 m of the fault. Because similar displacement distributions are observed in studies of coseismic surface ruptures, this suggests that distributed displacement accumulates through multiple seismic events. Fault displacements and slip rates may be significantly under-estimated if based on narrow aperture of piercing points (<100-200 m from the fault). Overall, ignoring distributed displacement will cause significant errors in geodynamic models.

Structural accommodation of distributed displacement is observed to occur through a combination of block rotation and displacement along secondary faults sub-parallel to the main fault. Rotational OFD may be associated with upright folding adjacent to faults. The intensity of OFD, as reflected in the density of faults, as well as the amount of rotation, increases toward the main fault zone. In the context of a block-model of distributed displacement, these observations imply a steady decrease of block-sizes towards the main

fault. Where measurable, integrated strain in OFD zones is dominated by normal drag, though reverse drag may also be present where blocks interact and where steep slip-gradients occur on faults. Displacement and damage in the study area are distributed in a similar pattern, and extend to similar distance away from faults. This suggests that zones of diminished rigidity near faults that is a consequence of OFD may be at least in part driven by formation and lengthening of secondary faults.

Future studies may benefit from the study of the interaction between folding and vertical axis rotation mentioned in section 5.6 (p. 84). Such studies may shed light on the volume problem associated with block rotation and its association with the internal deformation of blocks. Refinement of the analysis of block dimensions may be gained through a more homogeneous set of measurement of mylonitic lineation next to the Harper lake Fault. In addition, the use of metamorphic lineations to better understand block rotation within OFD zones seems promising and may yield interesting results if applied elsewhere. Lineation measurements should include shear sense indicators such as c-s fabric in order to measure rotations of $>90^\circ$.

Appendix 1: Table of mylonite lineation direction

Table A1. Mylonite lineation direction measurements and rotation							
Distance along fault (m)	Distance from fault (m)	Longitude (°)	Latitude (°)	Trend (°)	Plunge (°)	Rotation (°)	Flattening (°)
4737	1408	500694	3866240	212	5	0	0
4737	1407	500695	3866240	222	0	10	-5
4161	1364	500613	3866262	222	12	10	7
4161	1363	500614	3866262	220	12	8	7
4745	1362	500795	3866113	32	12	0	-17
4745	1361	500796	3866113	36	5	4	-10
2272	1358	499100	3867878	223	7	11	2
2272	1357	499102	3867878	53	14	21	-19
4050	1285	500484	3866300	222	3	10	-2
4050	1284	500485	3866300	220	5	8	0
2281	1256	499085	3867760	222	4	10	-1
2281	1255	499086	3867760	215	3	3	-2
4745	1223	500671	3866033	222	28	10	23
4745	1222	500672	3866033	220	15	8	10
3820	1193	500366	3866308	40	5	8	-10
3820	1192	500367	3866308	40	5	8	-10
4938	1134	500941	3865680	51	23	19	-28
4938	1133	500942	3865680	55	15	23	-20
2381	1133	499093	3867593	224	2	12	-3
2381	1132	499094	3867593	230	12	18	7
4745	1094	500606	3865920	213	5	1	0
4745	1093	500607	3865920	208	0	-4	-5
4934	1076	500854	3865687	225	0	13	-5
4934	1075	500855	3865687	225	0	13	-5
4938	1070	500960	3865554	220	31	8	26
4938	1069	500961	3865554	230	25	18	20
1213	1053	497884	3868406	213	14	1	9
1213	1052	497885	3868406	214	21	2	16
5298	1047	501036	3865436	222	10	10	5
5298	1046	501037	3865436	230	10	18	5
2044	1039	498861	3867659	55	21	23	-26
2044	1038	498862	3867659	50	28	18	-33
3784	1028	500153	3866329	224	8	12	3
3784	1027	500154	3866329	220	8	8	3
1213	1026	497832	3868397	213	33	1	28
1213	1025	497833	3868397	215	24	3	19
3780	1013	500103	3866369	32	6	0	-11
3780	1012	500104	3866369	25	8	-7	-13
3820	1009	500179	3866258	222	4	10	-1

3820	1008	500180	3866258	225	0	13	-5
2400	1007	499028	3867483	221	2	9	-3
2400	1006	499029	3867483	40	3	8	-8
2044	999	498705	3867740	220	25	8	20
2043	998	498707	3867741	235	21	23	16
2437	994	499048	3867449	65	12	33	-17
2437	993	499049	3867449	63	1	31	-6
3780	964	500059	3866346	40	3	8	-8
3780	963	500060	3866346	213	10	1	5
2438	962	499110	3867349	63	4	31	-9
2438	961	499111	3867349	51	5	19	-10
1213	947	497782	3868331	245	18	33	13
1213	946	497784	3868331	245	20	33	15
3780	937	500006	3866364	215	5	3	0
3780	936	500007	3866364	215	10	3	5
989	908	497725	3868312	219	2	7	-3
989	907	497726	3868312	217	9	5	4
999	902	497734	3868303	221	11	9	6
2463	895	499109	3867251	226	7	14	2
2463	894	499111	3867251	234	2	22	-3
3780	863	499967	3866297	225	5	13	0
3780	862	499968	3866297	215	8	3	3
1267	855	497913	3868170	212	22	0	17
1267	854	497915	3868170	216	26	4	21
2463	850	499070	3867228	224	5	12	0
2463	849	499071	3867228	225	6	13	1
2415	838	498932	3867343	235	5	23	0
2415	837	498933	3867343	231	8	19	3
4154	826	500187	3865933	222	5	10	0
4154	825	500188	3865933	220	2	8	-3
1297	821	497924	3868126	223	25	11	20
1297	820	497925	3868126	224	24	12	19
971	807	497658	3868234	215	2	3	-3
971	806	497659	3868234	216	6	4	1
3780	805	499896	3866288	210	0	-2	-5
3780	804	499897	3866288	205	5	-7	0
2463	804	499021	3867213	56	8	24	-13
2463	803	499022	3867213	230	2	18	-3
5298	799	500871	3865250	208	0	-4	-5
2438	799	498963	3867267	220	5	8	0
5298	798	500872	3865250	200	5	-12	0
2438	778	498993	3867205	235	10	23	5
2438	777	498995	3867205	237	3	25	-2
3100	768	499386	3866811	217	3	5	-2
3100	767	499387	3866811	42	2	10	-7
4193	767	500165	3865866	215	2	3	-3
4193	766	500166	3865866	225	10	13	5

1344	763	497938	3868052	221	33	9	28
1344	762	497939	3868052	213	21	1	16
1344	761	497940	3868052	214	21	2	16
1213	753	497737	3868143	215	22	3	17
3743	742	499826	3866269	208	2	-4	-3
3743	741	499827	3866269	210	1	-2	-4
1865	736	498453	3867599	244	18	32	13
1865	735	498454	3867599	235	38	23	33
5298	733	500832	3865192	205	19	-7	14
4160	732	500117	3865870	220	7	8	2
5298	732	500833	3865192	210	18	-2	13
4160	731	500118	3865870	226	8	14	3
882	731	497542	3868213	218	34	6	29
882	730	497543	3868213	224	31	12	26
882	729	497544	3868213	212	35	0	30
2438	720	498886	3867229	230	20	18	15
3100	710	499356	3866760	40	8	8	-13
3100	709	499358	3866760	43	2	11	-7
2301	708	498760	3867315	236	6	24	1
2301	707	498761	3867315	235	9	23	4
1317	706	497888	3868015	215	26	3	21
1317	705	497889	3868015	210	42	-2	37
2516	703	498997	3867088	33	2	1	-7
2463	702	498946	3867145	219	11	7	6
2516	702	498998	3867088	45	4	13	-9
2463	701	498947	3867145	217	16	5	11
959	700	497594	3868148	229	38	17	33
959	699	497596	3868148	230	31	18	26
5628	694	501166	3864750	220	0	8	-5
5628	693	501167	3864750	223	8	11	3
4142	691	500073	3865859	222	14	10	9
4142	690	500074	3865859	225	12	13	7
2281	690	498738	3867313	235	7	23	2
2281	689	498739	3867313	235	5	23	0
2463	687	498949	3867119	228	10	16	5
2463	686	498950	3867119	237	11	25	6
1356	680	497935	3867960	215	21	3	16
921	679	497550	3868149	238	24	26	19
2822	678	499179	3866840	215	8	3	3
921	678	497551	3868149	230	22	18	17
2822	677	499181	3866840	220	10	8	5
840	676	497479	3868188	199	44	-13	39
840	675	497480	3868188	202	43	-10	38
2438	673	498900	3867151	223	5	11	0
3743	672	499772	3866224	30	5	-2	-10
2438	672	498901	3867151	220	2	8	-3
3743	671	499773	3866224	30	8	-2	-13

2438	670	498847	3867197	230	12	18	7
3100	668	499358	3866701	227	0	15	-5
2438	668	498851	3867185	222	1	10	-4
3100	667	499359	3866701	226	5	14	0
1299	667	497853	3867986	196	33	-16	28
2438	667	498852	3867185	229	6	17	1
1182	666	497652	3868078	245	2	33	-3
1299	666	497854	3867986	200	91	-12	86
1005	665	497615	3868094	243	28	31	23
1182	665	497653	3868078	245	1	33	-4
1005	664	497616	3868094	225	23	13	18
1182	664	497654	3868078	80	4	48	-9
5388	663	500835	3865100	222	13	10	8
1005	663	497617	3868094	245	21	33	16
5388	662	500836	3865100	220	15	8	10
3743	661	499764	3866216	200	25	-12	20
3743	660	499766	3866216	210	10	-2	5
2379	655	498787	3867225	220	0	8	-5
2378	654	498788	3867224	245	13	33	8
2377	653	498789	3867224	245	9	33	4
3127	649	499386	3866645	218	3	6	-2
3127	648	499386	3866646	222	5	10	0
932	647	497544	3868116	235	27	23	22
932	646	497545	3868116	238	37	26	32
1283	644	497830	3867976	209	19	-3	14
2323	643	498746	3867246	220	12	8	7
1283	643	497831	3867976	206	19	-6	14
2323	642	498747	3867246	220	5	8	0
1213	640	497678	3868043	256	24	44	19
1213	639	497679	3868043	251	21	39	16
919	636	497527	3868113	221	29	9	24
919	635	497528	3868113	230	21	18	16
2281	634	498690	3867280	48	6	16	-11
2281	633	498691	3867280	222	2	10	-3
928	628	497532	3868103	228	29	16	24
927	628	497530	3868102	232	26	20	21
927	627	497531	3868102	206	34	-6	29
4161	620	500027	3865798	213	5	1	0
2430	620	498806	3867165	232	12	20	7
4161	619	500028	3865798	210	15	-2	10
2323	619	498748	3867209	220	15	8	10
2323	618	498749	3867209	225	4	13	-1
1213	617	497746	3867989	227	36	15	31
1213	616	497747	3867989	228	36	16	31
1213	615	497682	3868015	233	20	21	15
1213	614	497683	3868015	225	36	13	31
978	613	497566	3868063	230	39	18	34

978	612	497567	3868063	223	37	11	32
1213	612	497701	3868004	231	30	19	25
1213	611	497702	3868004	234	35	22	30
1213	608	497733	3867987	240	3	28	-2
1213	606	497731	3867984	238	8	26	3
1213	605	497732	3867984	235	1	23	-4
1215	604	497751	3867972	215	31	3	26
3697	603	499699	3866197	207	15	-5	10
1215	603	497752	3867972	197	35	-15	30
3697	602	499701	3866197	30	5	-2	-10
982	601	497564	3868051	229	42	17	37
982	600	497565	3868051	234	41	22	36
5535	599	500975	3864861	220	27	8	22
5535	598	500976	3864861	223	30	11	25
1288	597	497812	3867932	206	33	-6	28
1288	596	497813	3867932	210	35	-2	30
5628	592	501082	3864689	223	11	11	6
2756	591	499072	3866832	50	12	18	-17
5628	591	501083	3864689	220	10	8	5
2756	590	499073	3866832	220	12	8	7
1291	590	497814	3867924	218	30	6	25
1213	589	497660	3867996	211	36	-1	31
1291	589	497815	3867924	215	26	3	21
1213	588	497661	3867996	201	32	-11	27
1026	588	497595	3868017	234	38	22	33
1026	587	497596	3868017	230	31	18	26
3182	584	499366	3866570	205	13	-7	8
3182	583	499367	3866570	200	10	-12	5
837	581	497428	3868107	211	41	-1	36
837	580	497429	3868107	190	44	-22	39
2436	577	498782	3867129	60	14	28	-19
2435	576	498784	3867129	54	9	22	-14
967	575	497537	3868036	240	32	28	27
967	574	497538	3868036	240	38	28	33
1301	568	497810	3867900	190	15	-22	10
1301	567	497811	3867900	202	12	-10	7
4143	561	499972	3865778	210	13	-2	8
4143	560	499973	3865778	205	10	-7	5
996	557	497554	3868006	234	35	22	30
996	556	497555	3868006	235	39	23	34
5388	552	500745	3865033	225	10	13	5
5388	551	500746	3865033	230	15	18	10
2438	546	498779	3867090	230	9	18	4
2438	545	498780	3867090	234	6	22	1
2438	544	498783	3867086	230	8	18	3
5791	541	501085	3864600	218	15	6	10
5791	540	501086	3864600	219	10	7	5

1010	539	497557	3867984	241	29	29	24
3192	533	499335	3866527	210	15	-2	10
3697	533	499641	3866159	203	12	-9	7
3192	532	499336	3866527	212	40	0	35
3697	532	499642	3866159	205	18	-7	13
3192	531	499337	3866527	212	36	0	31
5971	518	501131	3864508	222	15	10	10
5971	517	501132	3864508	220	20	8	15
3697	508	499629	3866135	40	2	8	-7
3697	507	499630	3866135	222	5	10	0
4164	506	499942	3865727	208	15	-4	10
2738	505	498994	3866790	230	5	18	0
4164	505	499943	3865727	209	10	-3	5
2738	504	498996	3866790	222	2	10	-3
2738	503	498997	3866790	220	2	8	-3
2438	496	498750	3867051	230	8	18	3
1007	489	497529	3867942	235	43	23	38
1007	488	497531	3867942	234	42	22	37
5533	486	500862	3864824	220	28	8	23
5533	485	500863	3864824	220	24	8	19
3194	478	499297	3866489	200	35	-12	30
3194	477	499298	3866489	200	35	-12	30
947	473	497469	3867958	230	43	18	38
947	472	497470	3867958	242	46	30	41
3697	463	499579	3866121	218	21	6	16
3697	462	499580	3866121	220	13	8	8
2438	459	498723	3867024	227	11	15	6
2438	458	498724	3867024	230	9	18	4
5120	454	500578	3865051	222	4	10	-1
5120	453	500579	3865051	220	5	8	0
5373	448	500668	3864959	228	4	16	-1
923	448	497436	3867949	241	40	29	35
5373	447	500669	3864959	224	12	12	7
923	447	497437	3867949	234	46	22	41
3589	446	499558	3866119	220	18	8	13
3589	445	499559	3866119	225	25	13	20
4160	437	499885	3865687	219	18	7	13
4160	436	499886	3865687	220	10	8	5
5533	432	500828	3864781	225	22	13	17
5533	431	500829	3864781	230	20	18	15
2739	429	498939	3866739	220	15	8	10
2739	428	498940	3866739	225	10	13	5
2438	427	498707	3866994	230	20	18	15
2438	426	498709	3866994	240	22	28	17
5550	425	500845	3864744	233	12	21	7
2438	425	498710	3866994	220	23	8	18
5550	424	500846	3864744	235	10	23	5

2034	423	498345	3867288	245	38	33	33
2034	422	498346	3867288	235	35	23	30
895	422	497398	3867940	219	39	7	34
895	421	497399	3867940	214	45	2	40
922	421	497421	3867926	225	25	13	20
922	420	497422	3867926	228	24	16	19
2696	414	498899	3866762	233	10	21	5
2696	413	498901	3866762	50	2	18	-7
6154	406	501114	3864369	218	18	6	13
6154	405	501115	3864369	215	21	3	16
6026	404	501077	3864401	223	30	11	25
6026	403	501078	3864401	220	28	8	23
3185	402	499236	3866443	215	20	3	15
3185	401	499237	3866443	205	14	-7	9
6308	398	501232	3864268	218	10	6	5
5120	397	500515	3865037	20	4	-12	-9
6308	397	501233	3864268	218	10	6	5
3589	396	499505	3866105	222	25	10	20
5120	396	500516	3865037	25	5	-7	-10
3589	395	499507	3866105	220	20	8	15
1213	394	497632	3867798	231	34	19	29
3589	386	499494	3866106	220	40	8	35
5298	375	500561	3864958	225	18	13	13
2438	375	498672	3866958	224	15	12	10
5298	374	500562	3864958	230	10	18	5
5100	368	500485	3865034	218	5	6	0
4147	360	499817	3865650	215	20	3	15
4147	359	499818	3865650	215	14	3	9
3201	357	499214	3866400	210	18	-2	13
3201	356	499215	3866400	212	20	0	15
917	350	497381	3867868	227	44	15	39
2438	342	498639	3866943	210	20	-2	15
2803	341	498915	3866633	220	22	8	17
2803	340	498916	3866633	215	20	3	15
2877	335	498960	3866574	222	0	10	-5
2877	334	498961	3866574	220	10	8	5
2705	331	498843	3866700	208	9	-4	4
2705	330	498844	3866700	215	10	3	5
6342	321	501241	3864166	215	20	3	15
6342	320	501242	3864166	220	16	8	11
1869	320	498187	3867277	255	32	43	27
1874	319	498190	3867274	250	41	38	36
1869	319	498188	3867277	235	65	23	60
1874	318	498191	3867274	267	35	55	30
1869	318	498189	3867277	237	40	25	35
1874	317	498192	3867274	265	49	53	44
4123	313	499765	3865639	220	12	8	7

4123	312	499766	3865639	214	18	2	13
5120	311	500451	3864980	220	23	8	18
5120	310	500452	3864980	220	20	8	15
3493	304	499383	3866104	225	10	13	5
2768	303	498863	3866634	50	3	18	-8
3493	303	499385	3866104	225	15	13	10
2768	302	498864	3866634	46	18	14	-23
915	302	497355	3867828	225	28	13	23
1592	301	497974	3867431	249	33	37	28
2690	298	498809	3866690	215	12	3	7
3100	295	499090	3866440	203	15	-9	10
3100	294	499091	3866440	200	10	-12	5
3743	288	499499	3865953	210	35	-2	30
3743	287	499500	3865953	225	15	13	10
3743	286	499501	3865953	205	20	-7	15
4117	286	499740	3865627	210	20	-2	15
4117	285	499741	3865627	212	23	0	18
3230	283	499180	3866329	60	12	28	-17
3230	282	499181	3866329	45	2	13	-7
6308	282	501169	3864171	41	20	9	-25
6308	281	501170	3864171	40	22	8	-27
1803	277	498110	3867288	250	15	38	10
2428	277	498587	3866902	235	5	23	0
3153	276	499122	3866380	220	15	8	10
1803	276	498111	3867288	248	5	36	0
3153	275	499123	3866380	213	5	1	0
5605	273	500768	3864590	222	35	10	30
2429	273	498585	3866897	220	1	8	-4
5605	272	500769	3864590	225	30	13	25
2429	272	498586	3866897	215	22	3	17
5120	271	500428	3864946	216	10	4	5
5120	270	500429	3864946	215	13	3	8
2631	265	498745	3866712	220	10	8	5
1527	261	497900	3867446	253	23	41	18
3282	254	499194	3866270	225	18	13	13
3282	253	499195	3866270	225	15	13	10
2392	253	498544	3866906	223	15	11	10
2402	252	498551	3866899	245	5	33	0
3310	243	499206	3866243	235	12	23	7
3310	242	499207	3866243	240	12	28	7
3469	240	499314	3866092	232	23	20	18
3469	239	499315	3866092	230	20	18	15
2623	235	498716	3866698	220	20	8	15
5120	234	500399	3864921	220	18	8	13
2623	234	498717	3866698	215	15	3	10
5120	233	500400	3864921	220	11	8	6
2411	233	498545	3866878	242	5	30	0

5583	232	500717	3864593	222	5	10	0
2411	232	498546	3866878	248	19	36	14
5583	231	500718	3864593	220	8	8	3
2626	230	498715	3866693	245	15	33	10
2626	229	498717	3866693	240	12	28	7
6304	228	501135	3864127	220	0	8	-5
2722	227	498776	3866619	230	25	18	20
6304	227	501136	3864127	28	0	-4	-5
2722	226	498777	3866619	250	41	38	36
3407	226	499279	3866117	210	20	-2	15
3407	225	499280	3866117	215	18	3	13
1042	223	497425	3867695	229	36	17	31
2631	218	498710	3866681	240	18	28	13
3073	218	498945	3866439	65	26	33	-31
2386	217	498516	3866882	235	15	23	10
4051	215	499644	3865635	210	40	-2	35
4051	214	499645	3865635	210	25	-2	20
3740	213	499439	3865907	250	25	38	20
3740	212	499440	3865907	245	22	33	17
2627	211	498701	3866679	240	13	28	8
2628	211	498703	3866679	225	16	13	11
947	210	497336	3867732	255	34	43	29
4151	208	499700	3865552	208	28	-4	23
3060	208	498919	3866439	51	36	19	-41
4151	207	499701	3865552	208	30	-4	25
1799	207	498061	3867237	272	25	60	20
1799	206	498062	3867237	260	53	48	48
3056	198	498911	3866432	44	32	12	-37
3124	197	499036	3866358	218	40	6	35
5533	190	500642	3864626	240	11	28	6
2562	190	498643	3866715	205	19	-7	14
5533	189	500643	3864626	230	10	18	5
5581	189	500678	3864577	223	10	11	5
5581	188	500679	3864577	230	10	18	5
1496	182	497823	3867409	266	36	54	31
5127	181	500365	3864873	225	21	13	16
2385	181	498493	3866855	238	25	26	20
5127	180	500367	3864873	230	25	18	20
3697	179	499405	3865894	235	44	23	39
4198	179	499704	3865495	217	22	5	17
3697	178	499406	3865894	233	44	21	39
4198	178	499705	3865495	210	26	-2	21
4150	177	499674	3865533	210	20	-2	15
1746	177	497995	3867251	280	35	68	30
4150	176	499675	3865533	220	5	8	0
1746	176	497996	3867251	310	50	-82	-55
3126	175	499023	3866340	245	18	33	13

3056	172	498904	3866407	232	28	20	23
3315	169	499161	3866183	265	10	53	5
3315	168	499162	3866183	245	0	33	-5
2686	168	498708	3866607	227	34	15	29
2686	167	498709	3866607	225	28	13	23
2574	165	498632	3866689	235	21	23	16
3697	164	499385	3865892	250	33	38	28
3697	163	499386	3865892	235	38	23	33
3060	163	498913	3866393	272	43	60	38
3124	162	499012	3866332	224	23	12	18
2563	160	498621	3866694	235	32	23	27
4040	157	499591	3865608	200	38	-12	33
4040	156	499592	3865608	205	28	-7	23
3060	156	498912	3866385	301	26	89	21
2378	155	498470	3866838	250	35	38	30
3124	155	499006	3866328	223	19	11	14
2378	154	498471	3866838	255	15	43	10
3073	153	498918	3866379	178	54	-34	49
3878	153	499506	3865712	217	39	5	34
978	152	497334	3867666	214	56	2	51
3124	148	498999	3866325	220	42	8	37
3878	147	499502	3865705	183	46	-29	41
3878	146	499504	3865705	180	48	-32	43
4068	142	499596	3865576	225	18	13	13
3913	142	499503	3865696	204	32	-8	27
4068	141	499597	3865576	232	20	20	15
2385	141	498468	3866824	240	30	28	25
3100	140	498990	3866323	235	72	23	67
3310	138	499129	3866171	235	49	23	44
1217	138	497539	3867559	256	24	44	19
3310	137	499130	3866171	222	40	10	35
5127	137	500336	3864839	232	27	20	22
4195	136	499669	3865472	215	42	3	37
5127	136	500337	3864839	225	28	13	23
4034	135	499569	3865598	202	45	-10	40
4034	134	499570	3865598	191	55	-21	50
4034	133	499571	3865598	210	52	-2	47
5562	133	500621	3864558	230	22	18	17
6062	133	500914	3864181	210	12	-2	7
4022	132	499560	3865606	210	45	-2	40
5562	132	500622	3864558	220	25	8	20
6062	132	500915	3864181	215	10	3	5
4022	131	499561	3865606	210	50	-2	45
3913	131	499490	3865691	193	58	-19	53
3060	131	498891	3866368	243	44	31	39
3913	130	499491	3865691	180	45	-32	40
3126	130	498996	3866304	200	79	-12	74

2693	129	498683	3866575	228	42	16	37
2693	128	498684	3866575	235	50	23	45
2693	127	498685	3866575	220	39	8	34
3913	127	499489	3865689	187	50	-25	45
3035	126	498881	3866365	282	49	70	44
3127	126	498995	3866298	274	26	62	21
2561	125	498594	3866672	210	23	-2	18
3780	125	499406	3865815	204	39	-8	34
3664	124	499321	3865896	250	57	38	52
2394	124	498463	3866805	240	28	28	23
3664	123	499322	3865896	259	50	47	45
3268	122	499089	3866190	30	27	-2	-32
2569	122	498597	3866665	210	17	-2	12
3268	121	499091	3866190	28	21	-4	-26
5478	121	500546	3864622	232	18	20	13
1425	120	497729	3867413	295	14	83	9
5478	120	500547	3864622	238	8	26	3
3188	119	499031	3866246	235	18	23	13
3188	118	499032	3866246	230	35	18	30
3109	117	498976	3866304	268	21	56	16
3196	115	499035	3866239	80	10	48	-15
5208	115	500341	3864805	225	12	13	7
3126	115	498984	3866293	245	21	33	16
970	114	497308	3867638	220	37	8	32
5208	114	500342	3864805	228	12	16	7
3766	113	499389	3865811	210	35	-2	30
3109	113	498973	3866301	277	24	65	19
3766	112	499391	3865811	212	40	0	35
3759	111	499384	3865816	210	38	-2	33
3766	111	499392	3865812	208	35	-4	30
1742	110	497950	3867201	260	30	48	25
1742	109	497951	3867201	250	18	38	13
3913	108	499472	3865679	200	48	-12	43
3100	107	498966	3866298	256	29	44	24
3029	106	498860	3866353	275	41	63	36
2564	104	498580	3866656	218	35	6	30
2702	103	498668	3866550	229	50	17	45
3613	103	499293	3865897	222	50	10	45
2702	102	498669	3866550	208	52	-4	47
3613	102	499294	3865897	232	60	20	55
3628	101	499295	3865887	70	10	38	-15
2395	101	498449	3866786	258	38	46	33
3628	100	499296	3865887	83	11	51	-16
1275	100	497571	3867498	287	2	75	-3
3952	100	499492	3865641	220	49	8	44
3952	99	499493	3865641	235	55	23	50
2392	99	498445	3866786	250	39	38	34

2392	98	498446	3866786	253	45	41	40
3912	96	499463	3865673	217	47	5	42
3743	96	499368	3865814	212	41	0	36
3100	95	498954	3866295	235	34	23	29
2555	93	498565	3866655	205	30	-7	25
944	92	497274	3867632	350	15	-42	-20
5203	90	500314	3864796	233	20	21	15
3932	89	499470	3865650	210	49	-2	44
5203	89	500315	3864796	235	12	23	7
3215	88	499030	3866206	230	35	18	30
5550	88	500576	3864539	227	22	15	17
3215	87	499031	3866206	230	30	18	25
5550	87	500577	3864539	225	20	13	15
6158	87	500945	3864100	245	35	33	30
3911	87	499453	3865670	228	46	16	41
854	86	497193	3867672	316	33	-76	-38
6158	86	500946	3864100	245	42	33	37
3743	86	499357	3865809	216	46	4	41
6158	85	500947	3864100	252	40	40	35
2539	85	498549	3866662	227	23	15	18
2539	84	498550	3866662	225	15	13	10
5498	82	500533	3864582	228	15	16	10
3911	82	499450	3865667	222	54	10	49
5498	81	500534	3864582	230	18	18	13
808	80	497151	3867690	330	16	-62	-21
1356	79	497648	3867432	278	19	66	14
3197	78	499008	3866212	215	22	3	17
3197	77	499009	3866212	220	30	8	25
3890	77	499443	3865665	272	25	60	20
3743	77	499353	3865801	225	56	13	51
1722	76	497914	3867186	280	20	68	15
3100	76	498941	3866281	237	34	25	29
3741	75	499347	3865805	285	29	73	24
1722	75	497915	3867186	280	33	68	28
3433	74	499165	3866008	225	42	13	37
2998	74	498837	3866329	250	13	38	8
3433	73	499166	3866008	200	45	-12	40
3433	72	499167	3866008	235	50	23	45
3029	71	498850	3866317	270	18	58	13
5533	71	500553	3864547	232	8	20	3
3741	71	499346	3865802	287	30	75	25
3029	70	498852	3866317	260	42	48	37
5533	70	500554	3864547	222	5	10	0
3029	69	498853	3866317	270	28	58	23
3878	68	499433	3865669	301	39	89	34
3029	67	498849	3866315	265	35	53	30
3878	67	499431	3865670	302	25	90	20

3029	66	498851	3866315	260	25	48	20
3743	65	499342	3865796	30	58	-2	-63
3073	64	498889	3866296	261	24	49	19
3923	63	499445	3865641	192	28	-20	23
3878	63	499428	3865669	312	42	-80	-47
3923	62	499446	3865641	171	50	-41	45
3163	58	498969	3866222	222	25	10	20
3100	58	498930	3866267	239	11	27	6
3163	57	498970	3866222	222	21	10	16
3740	57	499333	3865794	150	4	-62	-1
2447	56	498465	3866712	241	50	29	45
3878	56	499421	3865666	338	44	-54	-49
2447	55	498466	3866712	254	55	42	50
3468	53	499155	3865986	240	40	28	35
2932	52	498784	3866345	278	20	66	15
3468	52	499156	3865986	245	25	33	20
3927	52	499439	3865630	170	26	-42	21
3878	52	499418	3865664	350	39	-42	-44
3073	51	498884	3866283	250	25	38	20
2932	51	498785	3866345	282	35	70	30
3927	51	499440	3865630	171	30	-41	25
5522	51	500526	3864542	230	18	18	13
3100	50	498923	3866258	255	32	43	27
3073	50	498885	3866283	247	18	35	13
2725	50	498645	3866499	255	62	43	57
5522	50	500527	3864542	225	40	13	35
3100	49	498924	3866258	250	27	38	22
2725	49	498646	3866499	250	55	38	50
3100	48	498925	3866258	235	22	23	17
799	47	497126	3867666	351	16	-41	-21
3877	46	499411	3865664	354	26	-38	-31
3381	45	499101	3866050	312	71	-80	-76
3937	45	499437	3865617	215	12	3	7
3740	45	499325	3865785	144	8	-68	3
2893	44	498752	3866369	290	15	78	10
3937	44	499438	3865617	218	25	6	20
2893	43	498753	3866369	292	27	80	22
835	43	497154	3867643	35	5	3	-10
809	42	497132	3867656	360	16	-32	-21
809	41	497133	3867656	358	19	-34	-24
5406	41	500436	3864620	215	10	3	5
5406	40	500437	3864620	210	15	-2	10
3734	40	499318	3865785	168	29	-44	24
5219	39	500296	3864743	230	32	18	27
3877	39	499404	3865661	340	43	-52	-48
5219	38	500297	3864743	225	31	13	26
3733	37	499313	3865785	178	36	-34	31

3870	36	499400	3865663	335	49	-57	-54
3870	35	499399	3865662	335	43	-57	-48
5235	35	500303	3864729	235	30	23	25
5235	34	500304	3864729	225	25	13	20
2530	34	498504	3866634	260	30	48	25
2878	33	498733	3866372	318	40	-74	-45
2418	33	498424	3866719	68	12	36	-17
3719	33	499302	3865788	340	1	-52	-6
2878	32	498734	3866372	298	43	86	38
2418	32	498425	3866719	255	9	43	4
2878	31	498735	3866372	325	38	-67	-43
2720	31	498628	3866490	232	40	20	35
5262	31	500324	3864706	230	20	18	15
2720	30	498629	3866490	230	50	18	45
5262	30	500325	3864706	220	11	8	6
2841	29	498706	3866398	295	15	83	10
2841	28	498708	3866398	312	6	-80	-11
5486	22	500482	3864550	240	10	28	5
5495	21	500487	3864542	235	2	23	-3
5486	21	500483	3864550	242	8	30	3
5495	20	500488	3864542	225	15	13	10
3860	19	499381	3865665	358	14	-34	-19
3703	18	499285	3865784	358	33	-34	-38
4628	16	499871	3865086	334	56	-58	-61
3701	13	499278	3865786	355	34	-37	-39
1706	10	497861	3867144	282	41	70	36
1706	9	497862	3867144	281	30	69	25
2588	9	498524	3866575	260	52	48	47
2588	8	498525	3866575	250	48	38	43
4429	5	499709	3865209	300	14	88	9
5362	4	500379	3864621	320	32	-72	-37
5362	3	500380	3864621	320	32	-72	-37
5424	3	500426	3864582	256	2	44	-3
5424	2	500427	3864582	260	0	48	-5
2452	2	498429	3866672	248	32	36	27
2452	1	498430	3866672	248	32	36	27
5128	-2	500215	3864779	42	51	10	-56
3860	-28	499390	3865665	338	42	-54	-47
1657	-91	497760	3867094	325	62	-67	-67
1657	-92	497761	3867094	300	65	88	60
1706	-118	497783	3867043	328	41	-64	-46
1659	-129	497738	3867063	340	59	-52	-64
1659	-130	497739	3867063	333	50	-59	-55
1658	-133	497735	3867061	130	25	-82	20
1658	-134	497736	3867061	120	40	88	-45

Note: Rotation and flattening values are calculated relative to the farthest-most point from the fault (the first point in the table).

Appendix 2: Calculation of parameters for seismic refraction model

Here I derive the refraction angles i and j as a function of a' , α , and v_{x0} . (Figs. 31, 32,). Refer to Figures 31 and 32 for the geometric configuration of these angles. Contours of seismic velocity, v , lie at an angle, α , from the ground surface line, AB. v_{xf} , v_{xr} and v_{x0} , are the seismic velocities at ground positions x_f , x_r and x_0 , respectively. Here, I use trigonometry to reduce variables and show v_{xr} and v_{xf} as function of v_{x0} , a' , and α . From eq. (18),

(A1)

$$h_f = \frac{v_{xf}}{a'}$$

$$h_r = \frac{v_{xr}}{a'}$$

$$h_0 = \frac{v_{x0}}{a'}$$

where a' is constant. Trigonometric relations show that

$$(A2) \frac{x_f}{z_f} = \frac{h_r}{z_r} = \frac{h_0}{z_0} = \cos \alpha,$$

$$(A3) \frac{h_f}{\cos \alpha} = \frac{v_{xf}}{a' \cos \alpha},$$

(A4)

$$z_f = \frac{v_{xf}}{a \times \cos \alpha},$$

$$z_0 = \frac{v_{x0}}{a \times \cos \alpha},$$

$$z_r = \frac{v_{xr}}{a \times \cos \alpha} .$$

From these I solve for the velocities,

(A5)

$$v_{xf} = z_f a' \cos \alpha ,$$

$$v_{x0} = z_0 a' \cos \alpha ,$$

$$v_{xr} = z_r a' \cos \alpha .$$

Figure 32 shows that $u=L-x/2$, and that $m=u \times \tan \alpha$. Therefore,

(A6)

$$\frac{z_f}{x_f} = \left(\frac{z_0 - (L - x/2) \tan \alpha}{x_0 - (L - x/2)} \right) ,$$

$$\frac{z_r}{x_r} = \left(\frac{z_0 + (L - x/2) \tan \alpha}{x_0 + (L - x/2)} \right) .$$

Combining with eq. (A5) and (A6),

(A7)

$$(A7a) \ v_{xf} = [z_0 + (L - x/2) \tan \alpha] a' \cos \alpha ,$$

$$(A7b) \ v_{xf} = z_0 a' \cos \alpha - (L - x/2) a' \sin \alpha ,$$

$$(A7c) \ v_{xf} = v_{x0} - (L - x/2) a' \sin \alpha$$

$$(A7d) \ v_{xr} = v_{x0} + (L - x/2) a' \sin \alpha$$

With v_{xr} and v_{xf} in terms of v_{x0} , a' , and α , I derive i and j as functions of these parameters. r_f , r_r , are the radius of the ray-paths, and are equal to,

(A8)

$$r_f = \sqrt{\left(\frac{x}{2}\right)^2 + z_f^2},$$

$$r_r = \sqrt{\left(\frac{x}{2}\right)^2 + z_r^2}.$$

Combining (A8) with eq. (A4) and (A7),

(A9)

$$r_f = \sqrt{\left(\frac{x}{2}\right)^2 + \left(\frac{v_{x0}}{a' \cos \alpha} - (L - x/2) \tan \alpha\right)^2},$$

$$r_r = \sqrt{\left(\frac{x}{2}\right)^2 + \left(\frac{v_{x0}}{a' \cos \alpha} + (L - x/2) \tan \alpha\right)^2}.$$

To define i and j , I apply the law of sine's on triangles A, F_a, (x_f, z_f) and A, R_a, (x_r, z_r),

$$(A10) r_f / \sin \alpha = \frac{x_f - x/2}{\sin i_f}.$$

This results in

$$(A11) \sin i_f = \left(\frac{x_f}{r_f} - \frac{x}{2 \times r_f}\right) \sin \alpha.$$

Because $v_{xf}/a' = x_f \sin \alpha$, (eq. A7c), eq. (A11) becomes

$$(A12) \sin i_f = \frac{v_{xf}}{a' r_f} - x \frac{\sin \alpha}{2 r_f}.$$

Similar relations for triangle A, F_b, (x_f, z_f), A, R_a, (x_r, z_r), and A, R_b, (x_r, z_r) give

(A13)

$$\sin j_f = \frac{v_{xf}}{a' r_f} + x \frac{\sin \alpha}{2 r_f},$$

$$\sin i_r = \frac{v_{xr}}{a' r_r} - x \frac{\sin \alpha}{2 r_r},$$

$$\sin j_r = \frac{v_{xr}}{a' r_r} + x \frac{\sin \alpha}{2 r_r}.$$

From $z_f/x_f = \tan \alpha$

$$(A14) x_f = z_f \cot \alpha ,$$

$$(A15) x_f = \left[z_0 - \left(L - \frac{x}{2} \right) \tan \alpha \right] \cot \alpha ,$$

$$(A16) x_f = \frac{v_{x0}}{a' \cos \alpha} \times \frac{\cos \alpha}{\sin \alpha} - \left(L - \frac{x}{2} \right),$$

$$(A17) x_f = \frac{v_{x0}}{a' \sin \alpha} - \left(L - \frac{x}{2} \right).$$

Similarly,

$$(A18) x_r = \frac{v_{x0}}{a' \sin \alpha} + \left(L - \frac{x}{2} \right).$$

Based on the law of sine's, triangles $A,F_a,(x_f, z_f)$ and $A,R_a,(x_r, z_r)$,

(A19)

$$r_f \sin i_f = (x_f - x/2) \sin \alpha = \left[\frac{v_{x0}}{a' \sin \alpha} - \left(L - \frac{x}{2} \right) - \frac{x}{2} \right] \sin \alpha ,$$

$$r_f \sin i_f = \frac{v_{x0}}{a'} - \left(L - \frac{x}{2} \right) \sin \alpha - \frac{x}{2} \sin \alpha ,$$

$$r_f \sin j_f = \frac{v_{x0}}{a'} - \left(L - \frac{x}{2} \right) \sin \alpha + \frac{x}{2} \sin \alpha .$$

Similarly, for r_r I get ;

(A20)

$$r_r \sin i_r = \frac{v_{x0}}{a'} + \left(L - \frac{x}{2} \right) \sin \alpha - \frac{x}{2} \sin \alpha ,$$

$$r_r \sin j_r = \frac{v_{x0}}{a'} + \left(L - \frac{x}{2} \right) \sin \alpha + \frac{x}{2} \sin \alpha .$$

Thus, using eq. (A19), (A20) I can express i , for both forward and reverse ray-paths in terms of the parameters a' , v_{x0} , α , and the variables x , and L . Recall that r is also a function of these parameters (eq. A19). Finally, I use eq. A12 to get:

(A21)

$$i_f = \sin^{-1} \left[\frac{1}{r_f} \left(\frac{v_{x0}}{a'} - \left(L - \frac{x}{2} \right) \sin \alpha - \frac{x}{2} \sin \alpha \right) \right],$$

$$j_f = \sin^{-1} \left[\frac{1}{r_f} \left(\frac{v_{x0}}{a'} - \left(L - \frac{x}{2} \right) \sin \alpha + \frac{x}{2} \sin \alpha \right) \right]$$

$$i_r = \sin^{-1} \left[\frac{1}{r_r} \left(\frac{v_{x0}}{a'} + \left(L - \frac{x}{2} \right) \sin \alpha - \frac{x}{2} \sin \alpha \right) \right]$$

$$j_r = \sin^{-1} \left[\frac{1}{r_r} \left(\frac{v_{x0}}{a'} + \left(L - \frac{x}{2} \right) \sin \alpha + \frac{x}{2} \sin \alpha \right) \right].$$

Appendix 3: $^{40}\text{Ar}/^{39}\text{Ar}$ dating of the Sunshine and Lavic basalts

A3.1 . $^{40}\text{Ar}/^{39}\text{Ar}$ samples, methods, and results

Groundmass separated from phenocrysts in samples PG-05-02 and -03 of the Sunshine and Lavic basalts was analyzed by the furnace incremental heating method following procedures in Singer et al. (2004). Briefly, ≈ 100 mg packets of 180-250 micron-sized groundmass grains were irradiated along with crystals of 1.194 Ma sandine from the Alder Creek rhyolite (Renne et al., 1998) which were used to monitor the neutron fluence, J . Mass discrimination was 1.0069 ± 0.0005 based on measurements from an automated air pipette during the analytical period. Procedural blanks were measured over a range of temperature before and after each incremental heating experiment and for the critical ^{36}Ar signals were typically 10 to 50 times smaller than the samples, hence their impact on overall uncertainty has been minimized. J values, reactor constants, and complete analytical results are in Tables A3, A4. Ages are reported with 2 sigma analytical uncertainties. Results from replicate incremental heating experiments comprising between 11 and 16 steps each are summarized in Table A2.

A3.2. Interpretation of $^{40}\text{Ar}/^{39}\text{Ar}$ results

The age spectra from both samples are discordant such that increments which define a continuous age plateau at the 95% confidence level give apparent ages significantly younger than adjacent increments. These results therefore strongly suggest that extraneous argon is present, either due to older material incorporated into the magma *en*

route to the surface, or the presence of excess argon in the magma at the time of eruption. The spectra from sample PG-05-03 step down from apparent ages of nearly 4 Ma at low temperature to plateau ages of about 1100 ka that comprise 80-95% of the gas released (Fig. 14). The MSWD values for these age plateaus are slightly larger than expected due to inclusion of steps near 60% of the ^{39}Ar released that have relatively low K/Ca ratios and slightly higher ages (Fig. 14; Table A2). Notwithstanding, combining the regressions of these 22 plateau steps yields an isochron age of 752 ± 110 ka and indicates that the lava contains argon with an initial $^{40}\text{Ar}/^{36}\text{Ar}$ ratio of 303.4 ± 2.5 which is significantly higher than the value of 295.5 for the atmosphere. Thus, this lava contains excess argon which has affected domains having slightly lower K/Ca ratios to a greater degree than those with higher K/Ca (Fig. 14). The isochron age, which makes no assumption about the initial composition of argon in the system, gives the best estimate of time since this lava was erupted.

The age spectra for sample PG-05-02 are also discordant, both are weakly saddle-shaped, and several of the high temperature gas-release steps that have lower than average K/Ca ratios yield apparent ages older than the mean plateau age of 182 ± 10 ka (Fig. 14). This lava may therefore also contain a small quantity of extraneous argon. The combined isochron age calculated from the 14 plateau steps is 163 ± 29 ka, which is indistinguishable from the plateau age, and indicates an initial $^{40}\text{Ar}/^{36}\text{Ar}$ ratio of 297.5 ± 2.9 that overlaps the atmospheric value. Despite the fact that excess argon is not present in a quantity such that it biases the age, we cannot rule out the possibility that a small amount of older inherited material is present in this lava. We suggest that the isochron age gives the most conservative estimate of time elapsed since this lava erupted.

Table A2: Summary of $^{40}\text{Ar}/^{39}\text{Ar}$ furnace incremental heating results on groundmass from Mojave Desert lava flows											
Sample	wt. (mg)	K/Ca total	Total fusion Age (Ma) $\pm 2 \sigma$	Increments used $^{\circ}\text{C}$	Age Spectrum			Isochron Analysis			
					^{39}Ar %	MSWD	Age (ka) $\pm 2 \sigma$	N	$^{40}\text{Ar}/^{36}\text{Ar} \pm 2 \sigma$	MSWD	Age (ka) $\pm 2 \sigma$
PG-05-02 (Sunshine basalt)											
UW57B6	96	0.361	231.6 \pm 13.0	630 - 1000	61.7	0.99	181.6 \pm 15.4	8 of 11	297.7 \pm 4.5	1.00	160.8 \pm 42.3
UW57C1	101	0.351	236.6 \pm 12.0	770 - 1120	55.2	0.61	183.1 \pm 14.3	6 of 12	297.3 \pm 3.7	0.52	164.4 \pm 40.5
				weighted mean plateau age	0.02		182.0 \pm 10.0	weighted mean isochron age	0.02		163.0 \pm 29.0
PG-05-03 (Lavic basalt)											
UW57C2	101	0.188	1274.2 \pm 79.8	720 - 1280	95.3	2.47	1126.2 \pm 68.2	11 of 13	302.1 \pm 3.3	0.90	820.5 \pm 152.2
UW57C3	115	0.276	1490.7 \pm 74.8	770 - 1220	79.8	3.14	1109.2 \pm 81.5	11 of 16	305.1 \pm 3.7	0.39	665.0 \pm 171.9
				weighted mean plateau age	0.75		1119.0 \pm 52.0	weighted mean isochron age	1.80		752.0 \pm 110.0

Ages calculated relative to 1.194 Ma Alder Creek rhyolite sanidine (Renne et al., 1998) using decay constants of Steiger and Jäger (1977).

Table A3: Complete $^{40}\text{Ar}/^{39}\text{Ar}$ incremental heating results for the Sunshine basalt										
ID #	Temp (°C)	$^{40}\text{Ar}/^{39}\text{Ar} \pm 1\sigma$	$^{38}\text{Ar}/^{39}\text{Ar} \pm 1\sigma$	$^{37}\text{Ar}/^{39}\text{Ar} \pm 1\sigma$	$^{36}\text{Ar}/^{39}\text{Ar} \pm 1\sigma$	F $\pm 1\sigma$	$^{39}\text{Ar}_k$ (%)	$^{40}\text{Ar}^*$ (%)	K/Ca	Apparent Age ± 2 ka
PG-05-02										
		Groundmass								
$J = 0.000262 \pm 0.49\% (1)$										
BD1707	# 630 °C	16.5299±0.1619	0.0251±0.0008	1.2570±0.0170	0.0543±0.0008	0.5915±0.2451	1.66	3.58	0.342	279.5±231.6
BD1708	# 680 °C	7.4446±0.0251	0.0191±0.0001	1.1259±0.0113	0.0244±0.0002	0.3243±0.0591	6.19	4.35	0.382	153.3±55.9
BD1709	# 730 °C	4.3378±0.0137	0.0160±0.0001	0.9738±0.0096	0.0137±0.0001	0.3598±0.0305	11.44	8.29	0.441	170.0±28.9
BD1710	# 780 °C	4.3721±0.0200	0.0155±0.0001	1.0772±0.0105	0.0139±0.0001	0.3626±0.0387	14.11	8.29	0.399	171.4±36.6
BD1711	# 830 °C	6.3771±0.0236	0.0170±0.0002	1.4465±0.0151	0.0205±0.0001	0.4445±0.0372	11.32	6.96	0.297	210.1±35.2
BD1712	# 880 °C	7.6267±0.0200	0.0178±0.0002	1.1879±0.0115	0.0249±0.0002	0.3755±0.0430	7.36	4.92	0.362	177.5±40.6
BD1713	# 940 °C	9.0957±0.0532	0.0189±0.0002	1.1257±0.0125	0.0295±0.0002	0.4752±0.0720	5.17	5.22	0.382	224.6±68.1
BD1714	# 1000 °C	10.7851±0.0496	0.0200±0.0004	1.2635±0.0132	0.0355±0.0002	0.3796±0.0547	4.43	3.52	0.340	179.4±51.7
BD1715	# 1070 °C	10.6067±0.0267	0.0195±0.0001	1.3266±0.0129	0.0338±0.0002	0.7142±0.0546	6.35	6.73	0.324	337.5±51.6
BD1716	# 1140 °C	10.5392±0.0124	0.0191±0.0002	1.2558±0.0119	0.0339±0.0001	0.6290±0.0381	11.00	5.96	0.342	297.3±36.1
BD1717	# 1220 °C	9.7947±0.0141	0.0187±0.0001	1.9737±0.0186	0.0315±0.0001	0.6382±0.0281	20.97	6.51	0.218	301.7±26.5
Total Fusion Age:		231.6±13.0	39 Ar % in Plateau		61.7					
Weighted Plateau from 8 of 11 Analyses:		MSWD	0.99		Plateau Temp Range	e 630 °C - 1000 °C				
Inverse Isochron from 8 of 11 Analyses:		MSWD	1.00		$^{40}\text{Ar}/^{39}\text{Ar} \pm 2\sigma$	297.7 ± 4.5				
$J = 0.000260 \pm 0.46\% (1)$										
101 mg aliquot										
Groundmass										
BD2043	# 670 °C	13.6940±0.0561	0.0225±0.0002	1.2976±0.0192	0.0449±0.0004	0.5289±0.1009	3.13	3.86	0.331	248.1±94.7
BD2044	# 720 °C	5.8074±0.0127	0.0172±0.0002	1.0536±0.0148	0.0182±0.0001	0.5250±0.0244	9.03	9.03	0.408	246.2±22.9
BD2045	# 770 °C	4.1369±0.0085	0.0158±0.0001	1.0093±0.0141	0.0130±0.0001	0.3758±0.0315	13.72	9.08	0.426	176.3±29.6
BD2046	# 820 °C	5.8554±0.0211	0.0159±0.0002	1.2907±0.0182	0.0180±0.0001	0.3805±0.0262	12.45	6.81	0.333	178.5±24.5
BD2047	# 880 °C	7.1908±0.0193	0.0171±0.0001	1.2122±0.0173	0.0235±0.0002	0.3276±0.0691	8.51	4.55	0.354	153.7±64.8
BD2048	# 980 °C	8.9037±0.0267	0.0190±0.0002	1.1351±0.0162	0.0289±0.0001	0.4456±0.0432	7.01	5.00	0.379	209.0±40.6
BD2049	# 1070 °C	10.3802±0.0284	0.0196±0.0001	1.3155±0.0184	0.0342±0.0002	0.3913±0.0452	6.75	3.77	0.327	183.5±42.4
BD2050	# 1120 °C	10.3614±0.0186	0.0192±0.0002	1.3132±0.0187	0.0340±0.0001	0.4083±0.0381	6.74	3.94	0.327	191.5±35.7
BD2051	# 1170 °C	10.3115±0.0266	0.0189±0.0002	1.2245±0.0175	0.0327±0.0002	0.7455±0.0488	8.19	7.22	0.351	349.6±45.8
BD2052	# 1200 °C	9.4270±0.0193	0.0188±0.0001	1.5733±0.0217	0.0304±0.0001	0.5687±0.0376	9.14	6.03	0.273	266.2±35.2
BD2053	# 1230 °C	9.6263±0.0160	0.0193±0.0002	2.8657±0.0398	0.0308±0.0001	0.7440±0.0388	8.32	7.71	0.150	349.0±36.4
BD2054	# 1260 °C	13.6925±0.0299	0.0217±0.0002	8.3396±0.1145	0.0460±0.0002	0.7650±0.0590	6.99	5.55	0.051	358.8±55.4
Total Fusion Age:		238.6±12.0	39 Ar % in Plateau		55.2					
Weighted Plateau from 6 of 12 Analyses:		MSWD	0.61		Plateau Temp Range	770 °C - 1120 °C				
Inverse Isochron from 6 of 12 Analyses:		MSWD	0.52		$^{40}\text{Ar}/^{39}\text{Ar} \pm 2\sigma$	297.3 ± 3.7				
183.1±14.3										
164.4±40.5										

All ages calculated relative to 1.194 Ma for the Alder Creek rhyolite sanidine (Renne et al., 1998) using the decay constants of Steiger and Jäger. Reactor constants are as follows: $[^{40}\text{Ar}/^{39}\text{Ar}]_K = 0.00086$; $[^{36}\text{Ar}/^{39}\text{Ar}]_Ca = 0.000264$; $[^{39}\text{Ar}/^{37}\text{Ar}]_Ca = 0.000673$. ^{37}Ar and ^{39}Ar corrected for post-irradiation decay, half lives of 35.2 days and 269 years, respectively. # indicates increments that have been included in weighted plateau and isochron calculations. $^{38}\text{Ar}/^{39}\text{Ar}$ ratio is not corrected for background signal.

Table A4: Complete $^{40}\text{Ar}/^{39}\text{Ar}$ incremental heating results for the Lavic basalt										
ID #	Temp (°C)	$^{40}\text{Ar}/^{39}\text{Ar} \pm 1\sigma$	$^{37}\text{Ar}/^{39}\text{Ar} \pm 1\sigma$	$^{36}\text{Ar}/^{39}\text{Ar} \pm 1\sigma$	F $\pm 1\sigma$	$^{39}\text{Ar}_k$ (%)	$^{40}\text{Ar}^*$ (%)	K/Ca	Apparent Age ± 2 ka	
PG-05-03										
101 mg aliquot		Groundmass			$\bar{J} = 0.000260 \pm 0.46\%$ (1)				$= 1.0069 \pm 0.05\%$ (1)	
BD1724	620 °C	1467.8679 ± 17.8925	1.9025 ± 0.0353	4.9103 ± 0.0594	17.0609 ± 0.0060	0.14	1.16	0.226	7984.9 ± 7477.4	
BD1725	670 °C	211.4845 ± 0.8960	1.6710 ± 0.0178	0.6970 ± 0.0043	5.6452 ± 1.0737	4.59	2.67	0.257	2646.0 ± 1005.8	
BD1726	720 °C	81.7689 ± 0.2317	1.4236 ± 0.0150	0.2669 ± 0.0020	3.0288 ± 0.5726	7.92	3.70	0.302	1420.1 ± 536.7	
BD1727	770 °C	41.9945 ± 0.1420	1.2163 ± 0.0131	0.1336 ± 0.0006	2.6076 ± 0.1809	11.66	6.20	0.353	1222.7 ± 169.6	
BD1728	820 °C	30.2445 ± 0.1373	1.2935 ± 0.0138	0.0934 ± 0.0007	2.7437 ± 0.2023	14.22	9.06	0.332	1286.5 ± 189.6	
BD1729	870 °C	38.9010 ± 0.1802	1.8604 ± 0.0205	0.1236 ± 0.0007	2.5195 ± 0.1672	12.21	6.47	0.231	1181.4 ± 156.8	
BD1730	920 °C	50.0609 ± 0.2295	1.6765 ± 0.0182	0.1606 ± 0.0008	2.7325 ± 0.2209	6.49	5.45	0.256	1281.3 ± 207.1	
BD1731	980 °C	43.7635 ± 0.1862	1.5198 ± 0.0180	0.1386 ± 0.0007	2.9290 ± 0.2464	3.54	6.69	0.283	1373.4 ± 231.0	
BD1732	1040 °C	47.4285 ± 0.4396	2.1872 ± 0.0301	0.1508 ± 0.0013	3.0381 ± 0.3719	2.56	6.40	0.196	1424.5 ± 348.7	
BD1733	1100 °C	38.0669 ± 0.1117	2.0474 ± 0.0227	0.1206 ± 0.0008	2.6090 ± 0.2323	2.28	6.84	0.210	1223.4 ± 217.8	
BD1734	1160 °C	31.5349 ± 0.1807	1.3343 ± 0.0150	0.0997 ± 0.0007	2.1784 ± 0.1850	5.25	6.90	0.322	1021.5 ± 173.4	
BD1735	1220 °C	24.5057 ± 0.0811	1.6887 ± 0.0175	0.0759 ± 0.0003	2.2021 ± 0.0771	17.99	8.98	0.254	1032.6 ± 72.3	
BD1736	1280 °C	28.2737 ± 0.0765	8.0284 ± 0.0803	0.0899 ± 0.0003	2.3647 ± 0.0895	11.15	8.32	0.053	1108.8 ± 83.9	
Total Fusion Age:		1274.2 ± 75.8	^{39}Ar % in Plateau	95.3						
Weighted Plateau from 11 of 13 Analyses:			MSWD	2.47	Plateau Temp Range 720 °C - 1280 °C				Age:	1126.2 ± 68.2
Inverse Isochron from 11 of 13 Analyses:			MSWD	0.9	$^{40}\text{Ar}/^{39}\text{Ar} \pm 2\sigma$				Age:	820.5 ± 152.2
115 mg aliquot		Groundmass			$\bar{J} = 0.000260 \pm 0.46\%$ (1)				$= 1.0069 \pm 0.05\%$ (1)	
BD2020	620 °C	2268.5253 ± 40.6423	1.4446 ± 0.0291	1.7372 ± 0.0661	75.0327 ± 20.3833	0.07	3.30	0.247	3485.5 ± 18756.0	
BD2021	650 °C	355.4137 ± 2.8699	0.2341 ± 0.0034	1.7024 ± 0.0296	11.0634 ± 1.7922	2.21	3.11	0.252	5182.0 ± 1676.5	
BD2022	680 °C	166.0960 ± 0.6642	0.1173 ± 0.0010	1.6010 ± 0.0234	8.4079 ± 0.9872	4.03	5.06	0.268	3939.5 ± 924.1	
BD2023	710 °C	91.2583 ± 0.4138	0.0695 ± 0.0007	1.4192 ± 0.0211	0.2938 ± 0.0017	4.5617 ± 0.3348	4.99	0.303	2138.5 ± 313.7	
BD2024	740 °C	55.5408 ± 0.1274	0.0453 ± 0.0008	1.2404 ± 0.0173	0.1752 ± 0.0009	3.8715 ± 0.2543	8.08	6.96	1815.1 ± 238.3	
BD2025	770 °C	38.8278 ± 0.1840	0.0345 ± 0.0002	1.1788 ± 0.0166	0.1230 ± 0.0006	2.5870 ± 0.1479	9.26	6.66	1213.0 ± 138.6	
BD2026	800 °C	31.6981 ± 0.1523	0.0311 ± 0.0002	1.2631 ± 0.0185	0.0994 ± 0.0005	2.4203 ± 0.1299	10.56	7.63	1134.9 ± 121.8	
BD2027	830 °C	30.2428 ± 0.1017	0.0301 ± 0.0003	1.4792 ± 0.0206	0.0948 ± 0.0005	2.3622 ± 0.1269	10.69	7.80	1107.7 ± 119.0	
BD2028	860 °C	40.7248 ± 0.1675	0.0370 ± 0.0003	1.9967 ± 0.0278	0.1298 ± 0.0008	2.5287 ± 0.2268	9.05	6.20	1185.7 ± 212.7	
BD2029	900 °C	55.2280 ± 0.2348	0.0464 ± 0.0003	1.9146 ± 0.0266	0.1770 ± 0.0008	3.0913 ± 0.2094	7.14	5.59	1449.4 ± 196.3	
BD2030	950 °C	33.3422 ± 0.2969	0.0316 ± 0.0004	1.2067 ± 0.0190	0.1046 ± 0.0008	2.5170 ± 0.2586	4.28	7.54	1180.3 ± 242.5	
BD2031	1000 °C	45.2205 ± 0.4692	0.0403 ± 0.0005	1.8653 ± 0.0313	0.1454 ± 0.0013	2.3944 ± 0.3889	2.73	5.29	1122.8 ± 364.6	
BD2032	1060 °C	40.2596 ± 0.3818	0.0374 ± 0.0005	2.3444 ± 0.3388	0.1274 ± 0.0010	2.8084 ± 0.3085	2.60	6.96	1316.8 ± 289.2	
BD2033	1120 °C	35.9747 ± 0.3323	0.0357 ± 0.0005	1.9051 ± 0.3038	0.1177 ± 0.0011	2.8198 ± 0.3117	2.73	7.83	1322.2 ± 292.2	
BD2034	1170 °C	30.2476 ± 0.2040	0.0313 ± 0.0003	1.3934 ± 0.0214	0.0952 ± 0.0010	2.2350 ± 0.2858	5.53	7.38	1048.0 ± 267.9	
BD2035	1220 °C	23.9814 ± 0.0726	0.0271 ± 0.0002	1.6942 ± 0.0235	0.0745 ± 0.0003	2.0939 ± 0.0794	15.23	8.72	981.9 ± 74.4	
Total Fusion Age:		1490.7 ± 74.8	^{39}Ar % in Plateau	79.8						
Weighted Plateau from 11 of 16 Analyses:			MSWD	3.14	Plateau Temp Range 770 °C - 1220 °C				Age:	1109.2 ± 81.5
Inverse Isochron from 11 of 16 Analyses:			MSWD	0.39	$^{40}\text{Ar}/^{39}\text{Ar} \pm 2\sigma$				Age:	665.0 ± 171.9

All ages calculated relative to 1.194 Ma for the Alder Creek rhyolite sanidine (Renne et al., 1998) using the decay constants of Steiger and Jäger. Reactor constants are as follows: $[^{40}\text{Ar}/^{39}\text{Ar}]K = 0.00086$; $[^{36}\text{Ar}/^{37}\text{Ar}]Ca = 0.000264$; $[^{39}\text{Ar}/^{37}\text{Ar}]Ca = 0.000673$. ^{37}Ar and ^{39}Ar corrected for post-irradiation decay; half-lives of 35.2 days and 269 years, respectively. # indicates increments that have been included in weighted plateau and isochron calculations. $^{38}\text{Ar}/^{39}\text{Ar}$ ratio is not corrected for background signal.

Appendix 4: Cenozoic evolution of the Ludlow fault, Cady Mountains and Blacktop Hills, California

Table of contents

Table of contents.....	117
List of Figures.....	118
A4.1. Background.....	119
A4.2. Quaternary Deformation.....	122
A4.2.1. Cady Mountains section.....	122
A4.2.2. Blacktop Hill section.....	127
A4.3. Discussion.....	128
A4.3.1. Uncertainty of the Cady Mountains offset.....	128
A4.3.2. Blacktop hills deflections.....	128
A4.3.3. Best estimate of Q2a age.....	129
A4.4. Conclusions.....	130

List of Figures

Figure A4.1. Location map	120
Figure A4.2. Map of the southern study area.....	123
Figure A4.3. Main faults in the Cady Mountains study area	124
Figure A4.4. Main folds in the Cady Mountains study area.....	125
Figure A4.5. Offset markers in the Cady mountain study area	126

A4.1. Background

The Mojave Desert section of Eastern California shear zone (ECSZ), is sliced by northwest striking, active dextral faults (Howard and Miller, 1992; Dokka and Travis 1990a, 1990b; Glazner et al., 2002; Fig. A4.1). To the east, the adjacent Sonoran block, is seismically quiet and contains few faults with evidence of Quaternary activity (Howard and Miller, 1992). The Ludlow fault is the eastern-most of the active northwest striking faults that transect the central Mojave Desert (Howard and Miller, 1992; Dokka, 1983; Dokka and Travis 1990a, 1990b; Fig. A4.1). As such, it may shed light on the characteristics of faulting at the margins of actively deforming regions. The fault, extending 60 kilometers northwest of the Lead Mountains, is among the least studied faults of the Mojave Desert. Understanding of its structure, displacement, timing of activity and slip-rate will contribute to the understanding of how strain is accommodated along the margins of the active ECSZ.

Estimates of the total dextral displacement across the Ludlow fault are mostly based on kinematics considerations and not on direct field observations. Dokka (1983) defines "small" amount of offset on the Ludlow fault, similar to the zero offset estimate provided by Garfunkel (1974) based on his block model. However, Dokka (1983) does not clarify the observational base for this estimate. Dokka and Travis (1990b) estimate two kilometers of displacement based on kinematic constraints imposed by adjacent blocks in their block model. The model defines the Ludlow fault as the boundary between an active, counter-clockwise rotated domain to the west, and an inactive, non-rotated domain to the east. Dokka and Travis (1990b) also suggest that the Mesquite Valley disrupted zone, a sinuous belt

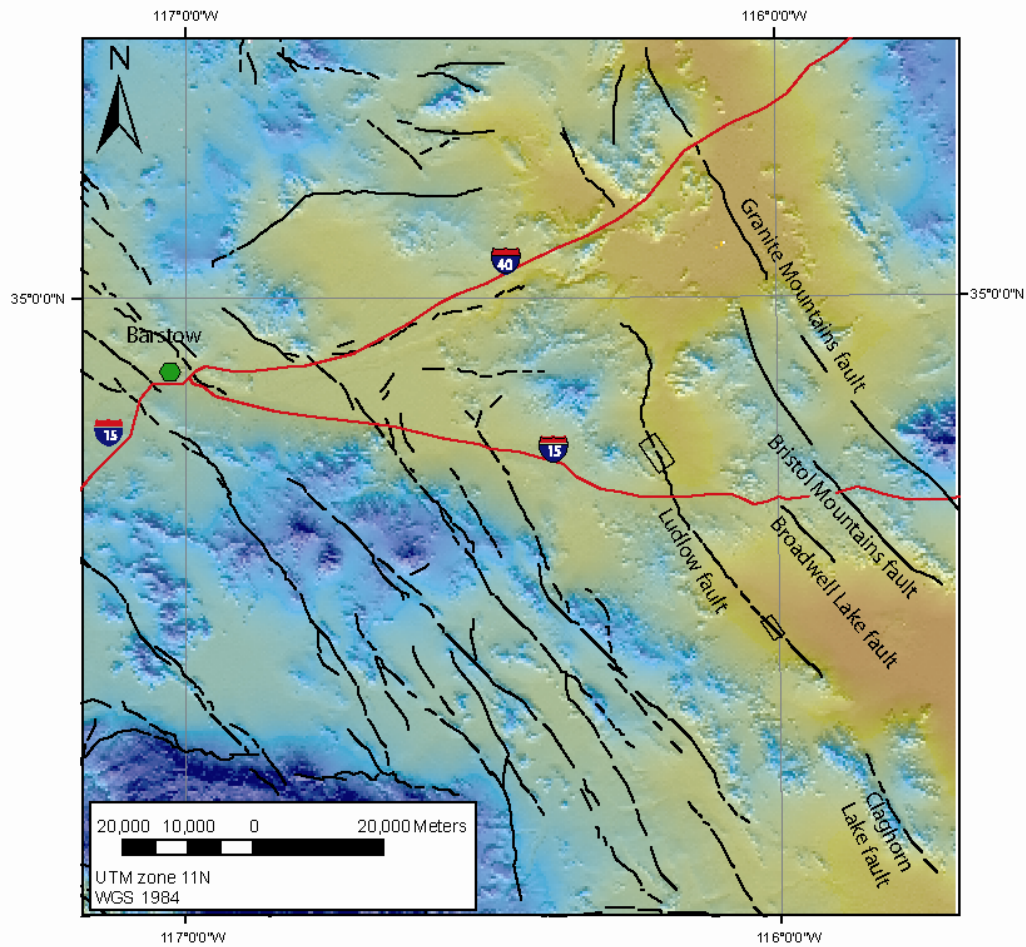


Figure A4.1. Index map of the central Mojave Desert. Black lines are faults. Black boxes show the Cady Mountains (north) and the Blacktop Hills (south) study areas. The Ludlow fault is the easternmost fault with evidence of Late Quaternary activity in this portion of the ECSZ.

of topographic depressions in continuum with the northern portion of the Ludlow fault, correlates with zone of thinned crust beneath this area of the Mojave Desert. They suggest an extensional or transtensional origin for this disrupted zone. Glazner et al. (2002) divide the Mojave Desert into domains of strike slip faulting and vertical axis rotation to interpret development of dextral shear across the region. Based on the work of Davis (1977), Davis and Burchfiel (1993), and Brady (1984) in the southern Death Valley fault zone, Glazner et al. (2002) estimate an offset of approximately four kilometers on the Ludlow fault. This estimate is based on averaging the displacement imposed by adjacent blocks (8-20 km) between the Ludlow, Broadwell Lake, Bristol Mountains, and Granite Mountains fault zones (Fig. A4.1).

The only direct observation of displacement on the Ludlow fault is provided by Howard and Miller (1992), who studied Late Cenozoic faulting along the southern portion of the Ludlow fault next to the Lead mountains. They suggest a minimum displacement of six kilometers across the Ludlow fault. Their estimate is based on correlation between the lithology of clasts in a tilted Neogene conglomerate and its possible source in the Bristol Mountains. Howard and Miller (1992) also suggest that the Cleghorn Lake fault is a southern extension of the Ludlow fault (Fig. A4.1), and estimate 2-3 kilometers of offset along the fault based on offset bedrock markers. The width of the Cleghorn Lake fault zone, as it is exposed in bedrock, is about 0.5 km. Although Howard and Miller (1992) report indicators of Quaternary faulting, they do not provide an estimate of Quaternary displacement and slip rate across the Ludlow fault.

This study aims to define Quaternary slip rates along the Ludlow fault based on field mapping (plate 1) and comparative dating. The Cady Mountains section of the Ludlow fault is located along the northern part of the fault, just west of the Broadwell Lake. Here, the fault

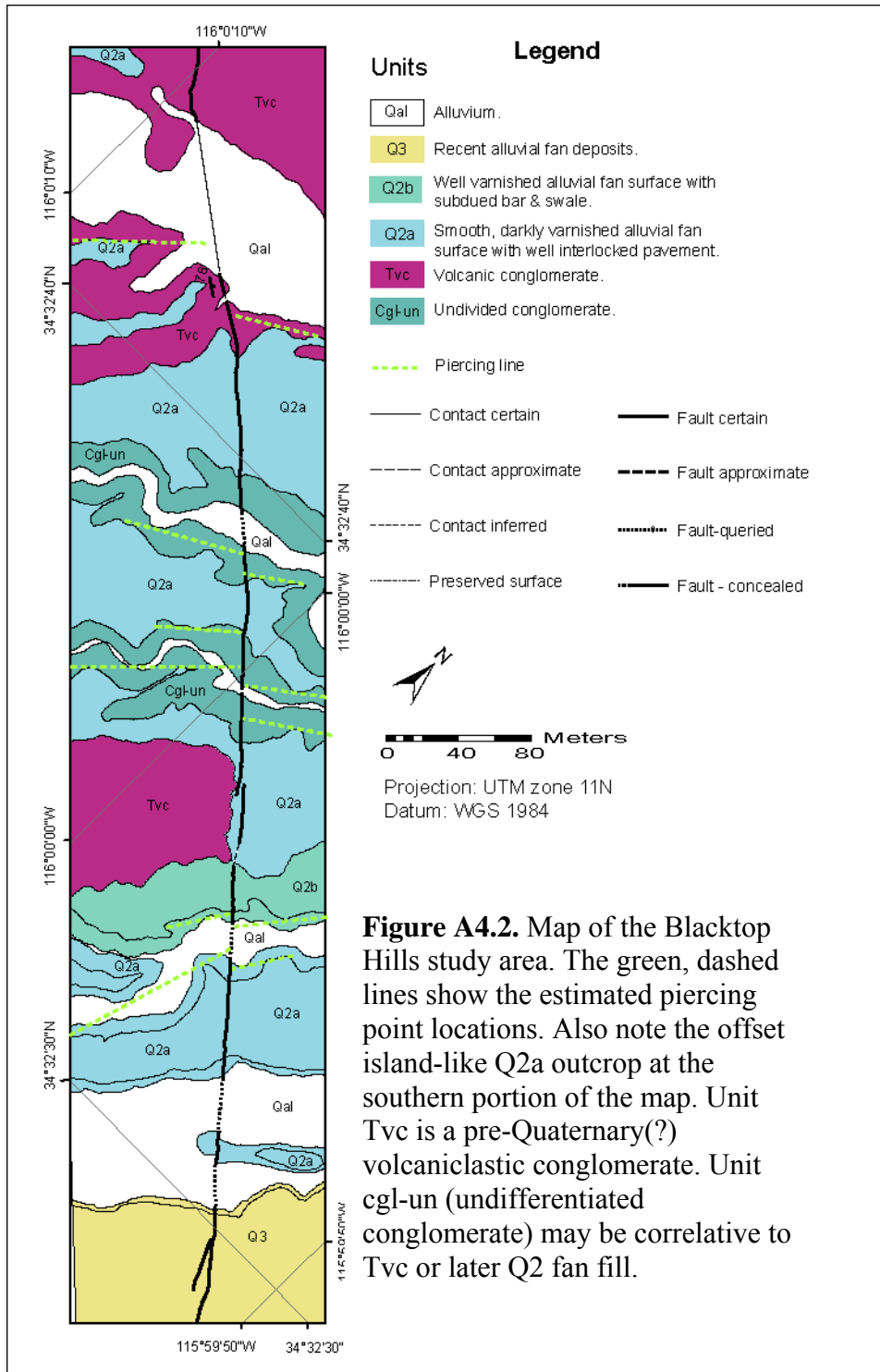
is adjacent to a line of low hills about one kilometer east of the slopes of the Cady mountains. The isolated valley, located between the Cady mountains and the hills, drains toward the Broadwell Lake through a set of channels, creating small canyons as they cross the line of low hills associated with the Ludlow fault. The Blacktop Hills section of the Ludlow fault is located nine kilometers north of the Lead mountains, within the Twentynine Palms Marine Base. Here, a segment of the fault with moderate topographic expression is exposed just east of the Blacktop Hills (Fig A4.2).

A4.2. Quaternary Deformation

A4.2.1. Cady Mountains section

The Cady Mountains section of the Ludlow fault zone trends 320°-340° and is composed of few, discontinuous, and often parallel fault strands, creating a fault zone of up to 250 m wide. The southwest side of the fault is continuously uplifted in the study area (Fig. A4.3) and the fault rarely disrupts Quaternary fan surfaces. The fault is accompanied by continuous folding and the major fold axis approximately follows the fault (Fig. A4.4). Quaternary alluvial fans and terrace surfaces are folded in two places - next to the fold hinge and in the area of a local tight fold one km east of the fault.

A few indications of Quaternary dextral offset are exposed in a small valley centered at 547086/3860180 (Fig. A4.5). Here, the fault offsets a small channel incised into Q2a and Q2b by 19 ± 4 m (574146/3850072). About 120 m to the north (574053/3850237) the riser of the southwestern terrace bounding a channel incised in Q2a surface is offset by at least 13 ± 3 m. At the same area (574065/3850230), preserved Q2a and Q2b surfaces, just across the fault



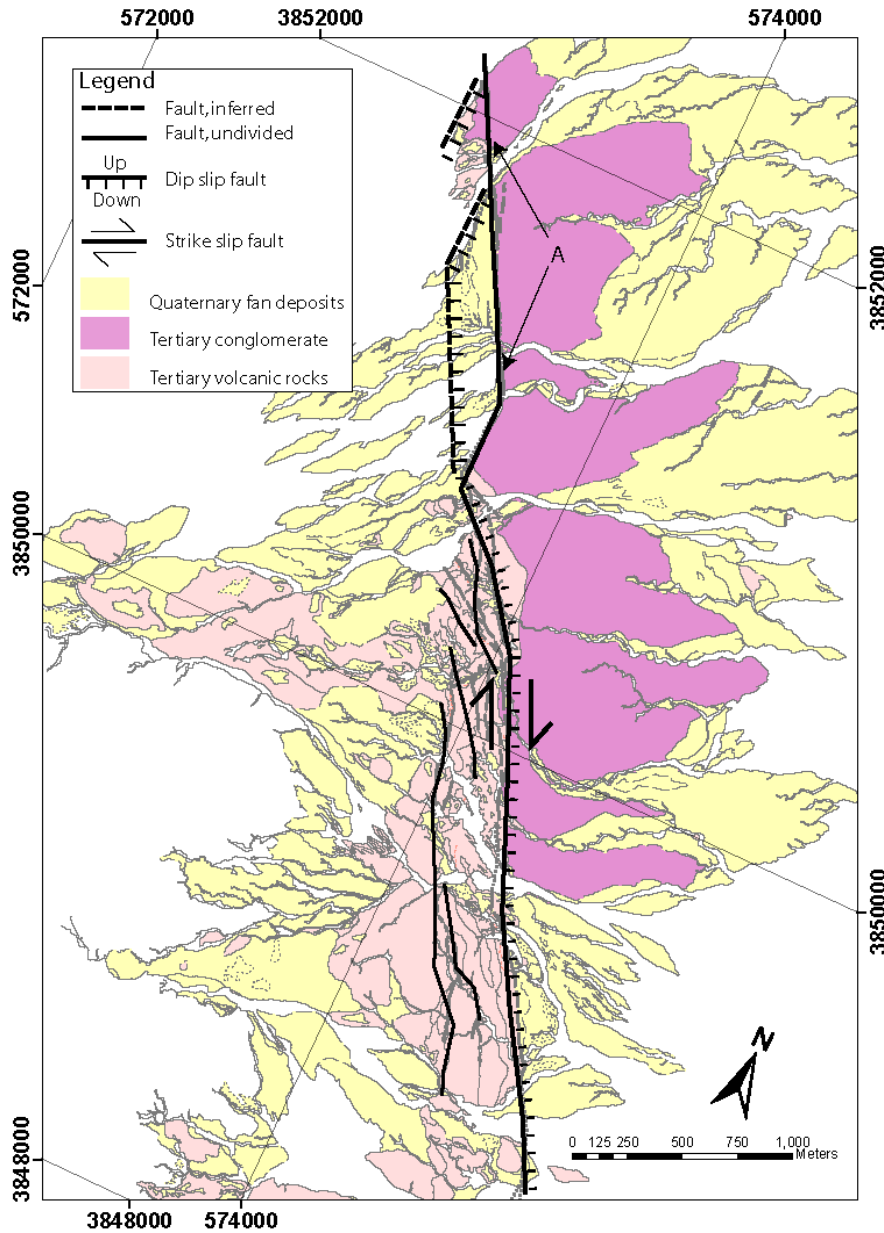


Figure A4.3. Illustration of the main faults in the Cady Mountains study area. Note the pull-apart basin at the northern section of the fault. The section labeled as ‘A’ at the northern portion of the fault marks the area where the southwest, downthrown side may have been initially uplifted and eroded before subsiding into the pull-apart basin.

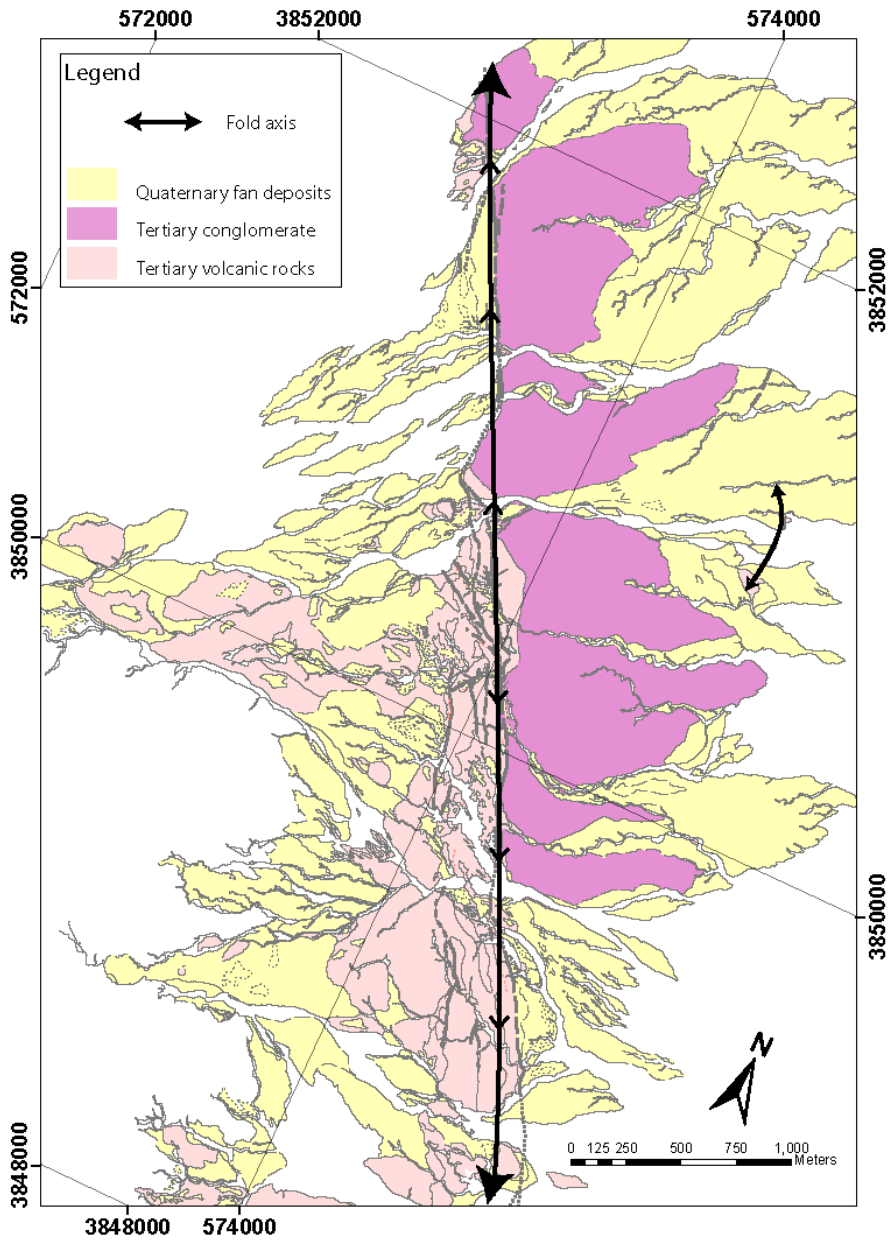


Figure A4.4. Main folds in the Cady Mountains study area. Note the northwest trending fold axis follows the Ludlow fault trace.

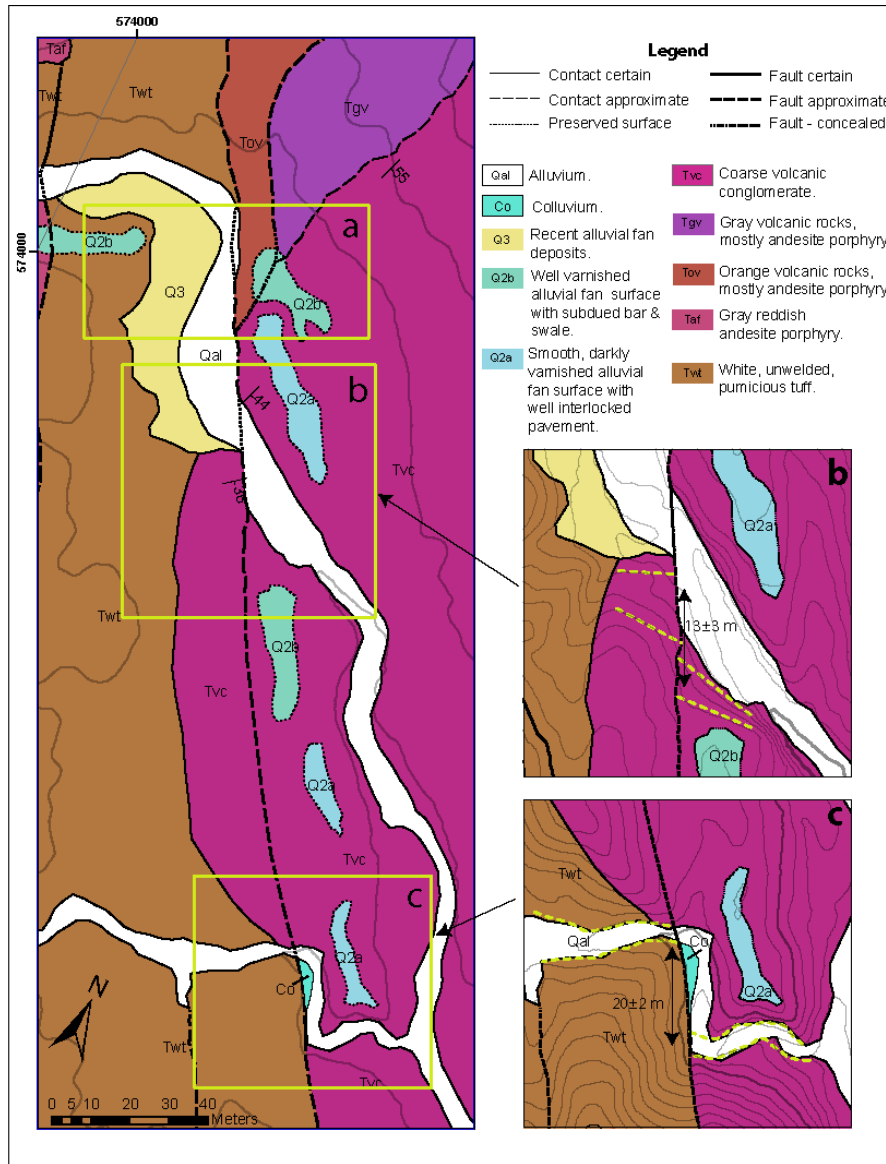


Figure A4.5. Offset stream channels and alluvial terraces in the Cady mountains study area. Contour interval is 10 m. Arrows in upper part of map shows Q2b strath terraces aligned across the fault. This supports an undetermined, but low amount of post-Q2b displacement. Inset map b shows terrace riser is offset by at least 13 ± 3 m. This offset is based on the projected contours shown as dashed yellow lines. This is a minimum offset because the terrace edge may have been eroded on the southwest side of the fault. Inset map c shows a channel that is dextrally offset by 19 ± 4 m, based on restoration of its channel margins shown as dashed yellow lines. Contour interval is 1m on inset maps, with 10m index contours shown in bold.

from an opening of small canyon with Q2a and Q2b straths, indicate a similarly low, but difficult to quantify amount of offset.

Vertical Quaternary displacement (southwest side down) occurs in several places at the northern section of the map (573220/3851880, 573550/3851270) within a pull apart basin bounded by right step in the trace of the main fault. A steep scarp in Tvc at the northernmost exposure of the fault (573160/3852000) probably also indicates Quaternary displacement. Interestingly, the southwest side down sense of Quaternary displacement has opposite sense of vertical displacement compared to the underlying Tertiary units ('A' on Fig. A4.3). This suggests that the southwest side of the fault was uplifted and eroded prior to subsiding into the pull-apart basin.

A4.2.2. Blacktop Hill section

A continuous fault segment with moderate topographic expression, trending 330°- 340°, is exposed at the Blacktop Hills area in the Twentynine Palms marine base. The southwest side of the fault is often uplifted and the fault disrupts quaternary deposits in multiple places. Tilted conglomerate and basalts are exposed in several places within up to 100 m from the fault. Beds strike subparallel to the fault and maximum dips are 80°. Quaternary units are possibly folded northeast of the fault at 591960/3823021.

Multiple indicators suggest small Quaternary dextral offsets along the fault (Fig. A4.2). Offset markers include a set of four channels incised in Q2a and offset by 20 ± 5 m. Another indicator is a local, isolated outcrop of Q2a within the active alluvium in the southern part of the map area that is offset by 2.4 ± 1.4 m. At the southern section of the map, where the fault is branched, it also offset channel bars on the Q3 fan by one to two meters (591984/3822647).

A4.3. Discussion

A4.3.1. Uncertainty of the Cady Mountains offset

Markers of dextral offsets in the Cady Mountains study area are few and thus provide sparse constraints for estimation of slip rate (Fig A4.5). The best-preserved marker is a channel offset by 19 ± 4 m. The channel is incised in both Q2a and Q2b and thus, assuming constant slip rate through time, the slip rate is calculated from the time of emplacement of the older Q2a strath terrace. The second marker, a terrace riser offset by 13 ± 3 m, is a minimum offset due to erosion of the original slope of the riser southwest of the fault. Here, the channel is diagonal to the fault and the offset riser at the southwest side of the fault is located in a favorable position for bank erosion. Therefore, this offset may preserve less than the actual offset since channel incision into Q2a. The third marker, an alignment of Q2a and Q2b straths across the fault, indicates that < 20 m of offset occurred since Q2a time. Although the Cady Mountains section of the Ludlow fault has only few markers for quaternary dextral offset, the similarity in the dextral displacement between these markers and the ones at the Blacktop hills section of the Ludlow fault support the reliability of these offsets and suggest no cumulative slip gradient along the fault.

A4.3.2. Blacktop hills deflections

The multiple offset markers in the Blacktop Hill section of the Ludlow fault range from 42 to 10 m. The estimated offset is calculated based on the minimal displacement (considering error) associated with the largest offset (22 m), and the maximal displacement associated with the smallest offset (19 m). The estimated offset, based on these two displacements, is 20.5 ± 1.5 m. A more conservative bootstrap technique, where I randomly

eliminate one offset to calculate a suite of slip estimates yields a best-estimate slip of 20 ± 5 m. These values agree well with the best-constrained offset value of 19 ± 4 measured in the Cady Mountains study area. The 2.4 ± 1.4 m deflection of Q2a outcrop does not contradict this value since the outcrop is an island-like exposure in the middle of an active channel. Continuous erosion through time probably aligned the margins of the outcrop after incision of Q2a and thus the 2.4 m offset represents the displacement that occurred since the last alignment of the outcrop margins and not since the initial incision of Q2a.

A4.3.3. Best estimate of Q2a age.

I estimate an age of Q2a surface based on correlation to dated surfaces of similar characteristics elsewhere in the Mojave Desert. The smooth, darkly varnished surface with well-interlocked desert pavement and a moderately developed argilic soil is similar to the 'F' fan surface described elsewhere in the Mojave Desert by Oskin et al., (2008), and Strane, (2007). Gurney (2007) estimated an age of 100 ± 30 ka for this alluvial generation based on limited cosmogenic dating of fan-surface clasts and comparison to dated fans in the Death Valley region. Oskin et al. (2008) used a conservative minimum age of 50 ± 20 ka for Q2a. This age was based on the age of the younger Q2b surface determined from sites along the Calico, Lenwood, and Helendale faults. Correlation of Q2a from the Ludlow fault to the F/Q2a alluvial fans of the central Mojave Desert may be inappropriate due to climatic differences between the arid eastern Mojave Desert and slightly more humid central Mojave Desert. The climatic difference, also reflected in the vegetation cover at these areas, may affect surface evolution and cause surfaces of similar appearance to have different ages.

A4.4. Conclusions

Late Quaternary dextral displacement of approximately 20 m occurs in two study areas along the Ludlow fault. Slip rate estimates, based on a minimum age of 50 ± 20 ka for the Q2a surface into which the channels are incised, are $< 0.4\pm 0.2$ mm/yr. This slip rate is relatively slow compared to other northwest striking faults that cross the Mojave Desert, and imply that Quaternary fault slip rates decrease at the transition to the Sonora block.

References

- Albers, J. P., 1967, Belt of sigmoidal bending and right-lateral faulting in the western Great Basin: Geological Society of America Bulletin, v. 78, p. 143-156.
- Baer, G. and Reches, Z., 1991, Mechanics of emplacement and tectonic implications of the Ramon dike system, Israel: Journal of Geophysical Research, v. 96, p. 11895–11910.
- Bartley, J.M., Glazner, A.F., and Fletcher, J.M., Martin, M.E., and Walker, J.D., 1992, Amount and nature of dextral off-set on neogene faults near Barstow, California: EOS (Transaction, American Geophysical Union), v. 73, p. 363.
- Bartley, J.M., Glazner, A.F., and Schermer, E.R., 1990, North-south contraction of the Mojave block and strike-slip tectonics in southern California: Science, v. 248, p. 1398-1401.
- Beck, M.E., 1980, Paleomagnetic record of plate-margin tectonic processes along the western edge of North America: Journal of Geophysical Research, v. 85, p. 7115-7131.
- Brady, R.H., 1984, Neogene stratigraphy of the Avawatz mountains between the Garlock and the Death Valley fault zones, southern Death Valley, California: implication as to late Cenozoic tectonism: Sedimentary geology, v. 38, p.127-157.
- Chester, J.S., Chester, F., M, and Kronenberg, A., K, 2005, Fracture surface energy of the Punchbowl Fault, San Andreas system, Nature, v. 437, p. 33-136.
- Davis, G., H, 1984, Structural Geology of rocks and Regions, John Willey and Sons, New York, 592 p.
- Davis, G.A., 1977, Limitations on displacement and southeastward extent of Death Valley fault zone, California: California division of Mines and Geology special report 129, p. 27-33.
- Davis, G.A., and Burchfiel, B.C., 1993, Tectonic problems revisited: the eastern terminus of the Miocene Garlock fault and the amount of slip on the Death Valley fault zone: Geological Society of America abstracts with programs, v. 9, p. 409.
- Demarest, H.H., 1983, Error analysis for the determination of tectonic rotation from paleomagnetic data: Journal of Geophysical Research, v. 88, p. 4321-4328.
- Dennis, J., 1972, Structural Geology, John Willey, New York, 532 p.
- Dibblee, T.W., 1964a, Geological Map of the Ord Mountains Quadrangle, San Bernardino County, California, Miscellaneous Geologic Investigations Map I-427: Washington D.C., U.S. Geological Survey.

- Dibblee, T.W., 1964b, Geological Map of the Rodman Mountains Quadrangle, San Bernardino County, California, Miscellaneous Geologic Investigations Map I-430: Washington D.C., U.S. Geological Survey.
- Dibblee, T.W., 1966, Geological Map of the Lavic Quadrangle, San Bernardino County, California, Miscellaneous Geologic Investigations Map I-472: Washington D.C., U.S. Geological Survey.
- Dibblee, T.W., 1967a, Geological Map of the Broadwell Lake Quadrangle, San Bernardino County, California, Miscellaneous Geologic Investigations Map I-478: Washington D.C., U.S. Geological Survey.
- Dibblee, T.W., 1967b, Geological Map of the Deadman Lake Quadrangle, San Bernardino County, California, Miscellaneous Geologic Investigations Map I-488: Washington D.C., U.S. Geological Survey.
- Dibblee, T.W., 1967c, Geological Map of the Emerson Lake Quadrangle, San Bernardino County, California, Miscellaneous Geologic Investigations Map I-490: Washington D.C., U.S. Geological Survey.
- Dibblee, T.W., 1967d, Geological Map of the Ludlow Quadrangle, San Bernardino County, California, Miscellaneous Geologic Investigations Map I-477: Washington D.C., U.S. Geological Survey.
- Dibblee, T.W., 1967e, Geological Map of the Old Woman Springs Quadrangle, San Bernardino County, California, Miscellaneous Geologic Investigations Map I-518: Washington D.C., U.S. Geological Survey.
- Dibblee, T.W., 1970, Geological Map of the Daggett Quadrangle, San Bernardino County, California, Miscellaneous Geologic Investigations Map I-592: Washington D.C., U.S. Geological Survey.
- Dibblee, T.W., and Bassett, A.M., 1966a, Geological Map of the Cady Mountains Quadrangle, San Bernardino County, California, Miscellaneous Geologic Investigations Map I-467: Washington D.C., U.S. Geological Survey.
- Dibblee, T.W., and Bassett, A.M., 1966b, Geological Map of the Newberry Quadrangle, San Bernardino County, California, Miscellaneous Geologic Investigations Map I-461: Washington D.C., U.S. Geological Survey.
- Dixon, T.H., Robaudo, S., Lee, J., and Reheis, M.C., 1995, Constraints on present-day Basin and Range deformation from space geodesy: *Tectonics*, v. 14, p. 755-772.
- Dokka, R.K., 1983, Displacement on late Cenozoic strike slip faults of the western Mojave Desert, California: *Geology*, v. 11, p. 305-308.

- Dokka, R.K., and Travis, C.J., 1990a, Late Cenozoic strike-slip faulting in the Mojave Desert, California: *Tectonics*, v. 9, p. 311-340.
- Dokka, R.K., and Travis, C.J., 1990a, Late Cenozoic strike-slip faulting in the Mojave Desert, California: *Tectonics*, v. 9, p. 311-340.
- Dokka, R.K., and Travis, C.J., 1990b, Role of the Eastern California Shear Zone in accommodating Pacific-North American plate motion: *Geophysical Research Letters*, v. 17, p. 1323-1326.
- Dokka, R.K., and Travis, C.J., 1990b, Role of the Eastern California Shear Zone in accommodating Pacific-North American plate motion: *Geophysical Research Letters*, v. 17, p. 1323-1326.
- Faulkner, D., R, Mitchell, T., M, Healy, D., and Heap, M., J, 2006, Slip on 'weak' faults by the rotation of regional stress in the fracture damage zone: *Nature*, v. 444, p. 922-925.
- Fialko, Y., 2004, Probing the mechanical properties of seismically active crust with space geodesy: Study of the coseismic deformation due to the 1992 Mw 7.3 Landers (southern California) earthquake: *Journal of Geophysical Research*, v. 109, p. doi: 10.1029/2003JB002756.
- Fialko, Y., Sandwell, D., Agnew, D., Simons, M., Shearer, P., and Minster, B., 2002, Deformation on nearby faults induced by the 1999 Hector Mine earthquake: *Science*, v. 297, p. 1858 - 1862.
- Fisher, R., A, 1953, Dispersion on a sphere: *Proceedings of the Royal Society of London, Series A*, v. 217, p. 295-305.
- Fletcher, J.M., Bartley, J.M., Martin, M.W., Glazner, A.F., and Walker, D.J., 1995, Large-magnitude continental extension: An example from the central Mojave metamorphic core complex: *Geological Society of America Bulletin*, v. 107, p. 1468-1483.
- Gan, W., Svarc, J.L., Savage, J.C., and Prescott, W.H., 2000, Strain accumulation across the Eastern California Shear Zone at latitude 36°30'N: *Journal of Geophysical Research*, v. 105, p. 16229-16236.
- Garfunkel, Z., 1974, Model for the late Cenozoic tectonic history of the Mojave Desert, California, and its relations to adjacent regions: *Geological Society of America Bulletin*, v. 5, p.141-188.
- Glazner, A.F., Bartley, J.M., and Sanner, W.K., 2000, Nature of the southwestern boundary of the central Mojave Tertiary province, Rodman Mountains, California: *Geological Society of America Bulletin*, v. 112, p. 34-44.
- Glazner, A.F., Walker, D.J., Bartley, J.M., and Fletcher, J.M., 2002, Cenozoic evolution of the Mojave block of southern California: in Glazner, A.F., Walker, D.J., and Bartley,

- J.M., eds., Geologic evolution of the Mojave desert and Southwestern Basin and Range: Boulder, Colorado, Geological Society of America Memoir, v. 195, p. 19-41.
- Glazner, A.F., Walker, D.J., Bartley, J.M., and Fletcher, J.M., 2002, Cenozoic evolution of the Mojave block of southern California: in Glazner, A.F., Walker, D.J., and Bartley, J.M., eds., Geologic evolution of the Mojave desert and Southwestern Basin and Range: Boulder, Colorado, Geological Society of America Memoir, v. 195, p. 19-41.
- Gurney, E., 2007, Slip Rate of the Camp Rock Fault and Folding of the Lenwood Anticline, Eastern California [M.S. thesis]: Chapel Hill, University of North Carolina.
- Hart, E. W., 1988, Fault-rupture Hazard Zones in California, Department of Conservation, California Division of Mines and Geology Special Publication 42.
- Hilley, G.E., Burgmann, R., -Z., Z.P., and Molnar, P., 2005, Bayesian inference of plastosphere viscosities near the Kunlun Fault, northern Tibet: Geophysical Research, v. 32, p. 1-4.
- Howard, K.A, and Miller, D.M., 1992, Late Cenozoic faulting at the boundary between the Mojave and Sonoran blocks: Bristol Lake area, California, In Richard, S.M., ed., Deformation associated with the Neogene eastern California shear zone, southeast California and southwest Arizona, Redlands, California, San Bernardino County Museum Association special publication 92-1, p. 37-47.
- Johnson A, M., Robert W, F., and Kenneth M, C., 1994, Shear zones formed along long, straight traces of fault zones during the 28 June 1992 Landers, California, earthquake: Bulletin of the Seismological Society of America, v. 84, p. 499-510.
- Jones, C. H., 2002, User-driven integrated software lives: "PaleoMag" paleomagnetism analysis on the macintosh: Computers and Geosciences, v. 28 (10), p. 1145-1151.
- Katz O., Reches Z. and Baer G., 2003, Faults and their associated host rock deformation: Structure of small faults in a quartz-syenite body, southern Israel: Journal of Structural Geology, v. 25, p.1675-1689.
- Kimorah, H., Itoh, Y., and Tsutsumi, H., 2004, Quaternary strike-slip crustal deformation around an active fault based on paleomagnetic analysis: a case study of the Enako fault in central Japan: Earth and Planetary Letters, v. 226, p. 321-334.
- Kirschvink, J.L., 1980, The least-squares line and plane and the analysis of paleomagnetic data: Geophysical Journal of the Royal Astronomical Society., v. 62, p. 699-718.
- Lamb, S., H, 1987, A model for tectonic rotations about a vertical axis: Earth Planetary Science letters, v. 84, p. 75-86.
- Lawn, B. R. and Wilshaw, T. R., 1975: Fracture of Brittle Soils, Cambridge University Press, Cambridge, UK, 204 p.

- Lawson, A.C., chairman, 1908, The California Earthquake of April 18, 1906: Report of the State Earthquake Investigation Commission: Carnegie Institution of Washington Publication, 87 p., 2 vols.
- Lemaitre, J., and Desmorat, R., 2005, Engineering Damage Mechanics: Ductile, Creep, Fatigue and Brittle Failures, 400 p.
- Li, Y., -G, Vidale, J., E, S, M., Day, and D, D., Oglesby, 2002, Study of the 1999 M7.1 Hector Mine, California, earthquake fault plane by trapped waves: Bulletin of the Seismological Society of America, v. 92(4), p. 1318-1332.
- Li, Y., Vidale, J., Aki, K., Xu, F., and Burdette, T., 1998, Evidence of Shallow Fault Zone Strengthening After the 1992 M7.5 Landers, California, Earthquake: Science, v. 279, p. 217-219.
- Li, Y.-G., and Vidale, J.E., 2001, Healing of the shallow fault zone from 1994-1998 after the 1992 M7.5 Landers, California, earthquake: Geophysical Research Letters, v. 28, p. 2999-3002.
- Li, Y.-G., Vidale, J.E., M, D., Steven, Oglesby, D., D, and Cochran, E., 2003, Postseismic Fault Healing on the Rupture Zone of the 1999 M 7.1 Hector Mine, California, Earthquake: Bulletin of the Seismological Society of America, v. 93, p. 854-869.
- Lyakhovskiy, V., Ben-Zion, Y., and Agnon, A., 2005, A viscoelastic damage rheology and rate- and state-dependent friction: Geophysical Journal International, v. 161, p. 179-190.
- Lyakhovskiy, V., Y. Ben-Zion and A. Agnon., 1997, Distributed Damage, Faulting, and Friction: Journal of Geophysical Research, v. 102, p. 27635-27649.
- McGill, S.M., and Rubin, C.M., 1999, Surficial slip distribution on the central Emerson fault during the June 28, 1992 Landers earthquake: Journal of Geophysical Research, v. 104, p. 4811-4833.
- Michel, R., and Avouac J, P., 2006, Imaging co-seismic fault zone deformation from Air Photos: The kikapoo stepover along the surface ruptures of the 1992 Landers earthquake: Journal of Geophysical Research. 111, B03408, doi:10.1029/2005JB003776.
- Miller, D.M., and Yount, J.C., 2002, Late Cenozoic tectonic evolution of the north-central Mojave Desert inferred from fault history and physiographic evolution of the Fort Irwin area, California, in Glazner, A.F., Walker, J.D., and Bartley, J.M., eds., Geologic Evolution of the Mojave Desert and Southwestern Basin and Range: Geological Society of America Memoir 195: Geological Society of America Memoir: Boulder, CO, Geological Society of America, p. 173-197.
- Nelson, M.R., and Jones, C.H., 1987, Paleomagnetism and crustal rotations along a shear zone, Las Vegas Range, southern Nevada: Tectonics, v. 6, p. 13-33.

- Oskin, M., and Iriondo, A., 2004, Large-magnitude transient strain accumulation on the Blackwater fault, Eastern California shear zone: *Geology*, v. 32, p. 313-316.
- Oskin, M., Perg, L., Shelef, E., Strane, M., Gurney, E., Singer, B., and Zhang, X., 2008, Elevated shear-zone loading rate during an earthquake cluster in eastern California: *Geology*, in press.
- Oskin, M., Perg, L., Shelef, E., Strane, M., Gurney, E., Singer, B., and Zhang, X., in review: Elevated shear-zone loading rate during an earthquake cluster in eastern California, *Geology*.
- Oskin, M.E., Perg, L.A., Blumentritt, D., Mukhopadhyay, S., and Iriondo, A., 2007, Slip rate of the Calico fault: Implications for geologic versus geodetic discrepancy in the Eastern California shear zone: *Journal of Geophysical Research*, v. 112, p. doi:10.1029/2006JB004451.
- Passchier, C.W., 2001, Flanking structures: *Journal of Structural Geology*, v. 23, p. 951-962.
- Rabotnov, Y., N, 1988, *Mechanics of deformable solids*: Science, Moscow, p. 712.
- Reches, Z., and Eidelman, A., 1995, Drag along faults: *Tectonophysics*, v. 247, p. 145-156.
- Renne, P.R., Swisher, C.C., Deino, A.L., Karner, D.B., Owens, T.L., and DePaolo, D.J., 1998, Intercalibration of standards, absolute ages and uncertainties in $^{40}\text{Ar}/^{39}\text{Ar}$ dating: *Chemical Geology*, v. 145, p. 117-152.
- Richard, P., Mocquet, B., and Cobbold, P., R, 1991, Experiments on simultaneous faulting and folding above a basement wrench fault. *Tectonophysics*, v. 188, p. 133-141.
- Rockwell, T. K., and Y. Ben-Zion., 2007, High localization of primary slip zones in large earthquakes from paleoseismic trenches: Observations and implications for earthquake physics: *Journal of Geophysical Research*, v. 112, B10304, doi:10.1029/2006JB004764
- Rockwell, T.K., Lindvall, S., Dawson, T., Langridge, R., Lettis, W.R., and Klinger, Y., 2002, Lateral offsets on surveyed cultural features resulting from the 1999 Izmit and Düzce Earthquakes, Turkey: *Bulletin of the Seismological Society of America*, v. 92, p. 79-94.
- Rockwell, T.K., Lindvall, S., Herzberg, M., Murbach, D., Dawson, T., and Berger, G., 2000, Paleoseismology of the Johnson Valley, Kickapoo, and Homestead Valley faults: Clustering of earthquakes in the Eastern California Shear Zone: *Bulletin of the Seismological Society of America*, v. 90, p. 1200-1236.
- Rymer, M.J., Seitz, G.G., Weaver, K.D., Orgil, A., Faneros, G., Hamilton, J.C., and Goetz, C., 2002, Geologic and Paleoseismic Study of the Lavic Lake Fault at Lavic Lake Playa, Mojave Desert, Southern California: *Bulletin of the Seismological Society of America*, v. 92, p. 1577-1591.

- Salyards, S.L., Sieh, K.E., and Kirschvink, J.L., 1992, Paleomagnetic measurement of nonbrittle coseismic deformation across the San Andreas fault at Pallett Creek: *Journal of Geophysical Research*, v. 97, p. 12457-12470.
- Scholz, C., H, 1968, Microfracturing and inelastic deformation of rock in compression: *Journal of Geophysical Research*, v. 73, p. 1417-1432.
- Scholz, C., H, 1990, *The Mechanics of Earthquakes and Faulting*, Cambridge University Press, Cambridge, UK, 439 p.
- Scholz, C., H., Dawers, N., H, Yu, J., -Z, Anders, M., H, and Cowie, P., A, 1993, Fault growth and fault scaling laws: Preliminary results: *Journal of Geophysical Research*, v. 98 (B12), p. 21-951.
- Sheriff, R., E, and Geldart, L., P, 1995, *Exploration Seismology*, Cambridge University Press, Cambridge, UK, 592 p.
- Shipton Z. K., Evans J. P., Abercrombie R. E., Brodsky E.E. 2006. The missing sinks: Slip localization in faults, damage zones, and the seismic energy budget, In: *American Geophysical Union Geophysical Monograph Series, Volume 170, Earthquakes: Radiated Energy and the Physics of Faulting*. Editors: R. Abercrombie, A. McGarr, G. Di Toro and H. Kanamori. p 217-222.
- Singer, B.S., Ackert, R.P. Jr., and Guillou, H., 2004, $^{40}\text{Ar}/^{39}\text{Ar}$ and K-Ar chronology of Pleistocene glaciations in Patagonia: *Geological Society of America Bulletin*, v. 116, p. 434-450.
- Sonder, L.J., Jones, C.H., Salyards, S.L., and Murphy, K.M., 1994, Vertical axis rotations in the Las Vegas Valley Shear Zone, southern Nevada: Paleomagnetic constraints on kinematics and dynamics of block rotations: *Tectonics*, v. 13, p. 769-788.
- Stein, R. and M. Wysession, *An Introduction to Seismology, Earthquakes and Earth Structure*, 2003, Blackwell Publishing, Oxford, 498 p.
- Strane, M., 2007, Masters thesis, 55 p.
- Strane, M., 2007, Slip rate and structure of the nascent Lenwood fault zone, eastern California [M.S. thesis]: Chapel Hill, Universit
- Thatcher, W., and Lisowski, M., 1987, Long-term seismic potential of the San Andreas fault southeast of San Francisco, California: *Journal of Geophysical Research*, v. 92, p. 4771-4784.
- Treiman, J.A., Kendrick, K.J., Bryant, W.A., Rockwell, T.K., and McGill, S.F., 2002, Primary surface rupture associated with the Mw 7.1 16 October 1999 Hector Mine earthquake, San Bernardino County, California: *Bulletin of the Seismological Society of America*, v. 92, p. 1171-1191.

- Valentine, M.J., Vbrow, L.L., and Golombek, M.P., 1993, Cenozoic crustal rotations in the Mojave Desert from paleomagnetic studies around Barstow, California: *Tectonics*, v. 22, p. 666-677.
- Vermilye, J., M, and Scholz, C., H, 1998, The process zone; a microstructural view of fault growth: *Journal of Geophysical Research*, v. 103, p. 12,223-12,237.
- Wells, R., E, and Hillhouse, J., W, 1989, Paleomagnetism and tectonic rotation of the lower Miocene Peach Springs Tuff: Colorado Plateau, Arizona, to Barstow California: *Geological Society of America Bulletin*, v. 101, p. 846-863.
- Wilbur, 1980, The nature and origin of Quaternary basaltic volcanism in the central Mojave desert area, California: Unpublished Ms thesis, San Jose State University, 134 p., 3 pl. (1:24,000 scale).
- Wilson, B., Dewers, T., and Reches, Z.B., J, 2005, Particle size and energetics of gouge from earthquake rupture zones: *Nature*, v. 434, p. 749-752.
- Yamashita, T., 2000, Generation of microcracks by dynamic shear rupture and its effects on rupture growth and elastic wave radiation: *Geophysics Journal International.*, v. 143, p. 395-406.
- Zoback, M., D, Zoback, M., L, Mount, V., S, Suppe, J., Eaton, J., P, Healy, J., H, Oppenheimer, D., Reasenberg, P., Jones, L., Raleigh, C., B, Wong, I., G, Scotti, O., and Wentworth, C., 1987, New evidence on the state of stress of the San Andreas fault system: *Science*, v. 238, p. 1105-1111.